Dynamic Modeling and Passivity-Based Control of a 2 DOF Tower Crane with a Flexible Hoist Cable

A THESIS
SUBMITTED TO THE FACULTY OF THE GRADUATE SCHOOL
OF THE UNIVERSITY OF MINNESOTA
BY

Ping-Yen Shen

IN PARTIAL FULFILLMENT OF THE REQUIREMENTS
FOR THE DEGREE OF
MASTER OF SCIENCE

Advisor: Ryan James Caverly

August, 2020

Acknowledgements

Great thanks to my family and my advisor Prof. Ryan James Caverly who always led me, guided me, and helped me throughout my time in graduate school. My full-time graduate studying is supported by Chung-Cheng Institute of Technology, National Defense University, Taiwan (R.O.C.).

Dedication

To my grandfather.

Abstract

Tower cranes are ubiquitous with the construction of modern infrastructure owing to high payload capacity, operational flexibility, and efficiency. This thesis aims to find a solution to achieving quick payload maneuver trajectory with reduced oscillations, and ensuring applicability to autonomous tower cranes that feature noncolocation, underactuation, and uncertain dynamics. A dynamic model of a 2 DOF tower crane is presented accounting for the winch inertia and the axial cable stiffness that varies with the length of the cable using a Rayleigh-Ritz discretization approach. The two proposed control methods, μ-tip control and adaptive sliding-mode control, employ passivity-based control to provide rigorous robust guarantees of closed-loop input-output stability when performing trajectory tracking of a tower crane's payload. The use of the μ-tip rate for trajectory tracking of the crane's payload greatly simplifies the task of designing a stabilizing feedback controller. The proposed μ-tip control uses a μ-tip modification to establish a passive input-output mapping of a 2 DOF tower crane with a flexible hoist cable from a modified force input to the payload's μ-tip rate by considering the sway angle as a flexible coordinate. However, the μ-tip control method relies on the assumptions that the sway angle and its angular rate remain small. A robust sliding-mode-inspired passivity-based control with an adaptive update law that does not rely on a specific structure of the dynamic equations or exact knowledge of the crane's mass properties is presented including experimental validations. A formulation of the adaptive sliding-mode control in the payload coordinates, which facilitates the generation of desired trajectories and the choice of control

gains, is presented. The control theory developed in this thesis is not limited to only tower cranes, and can be extended to cable-driven robots and flexible robotic manipulators.

Table of Contents

List of Tables

List of Figures

Chapter 1

Introduction

1.1 Motivation

Tower cranes, such as the one shown in Figure 1.1, are ubiquitous with the construction of modern infrastructure owing to high payload capacity, operational flexibility, and energy efficiency. Accurately controlling the motion of a tower crane's payload when performing quick trajectories is a challenging task [3, 4]. This is predominantly due to the fact that tower cranes are underactuated, meaning that they have less inputs than generalized coordinates (parameters in configuration space), and they are noncolocated, given that the system's control inputs are located at the opposite end of a hoist cable that may have its own dynamics. Traditionally, manipulation of a tower crane relies heavily on the experience and skill-level of a human operator. The repeating trajectory manipulation and the manual operation accounting for payload swaying have increased operational time and reduced efficiency. Autonomous systems can potentially give a solution with faster manipulation and lower humanity cost/risk but not loosing the trajectory accuracy. To assist the design of autonomous crane control methods, dynamic models have been derived that include the vibrations of the tower frame [5] and the hoist cable [5, 6]. Partial differential equations (PDE) and boundary conditions can be used to model a flexible hoist cable [7, 8].

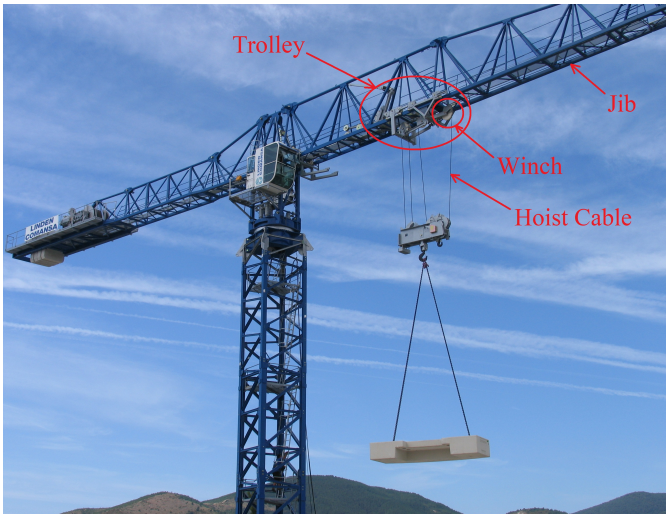

Figure 1.1: Tower crane and its main components [1].

A number of control strategies are found in the literature that can be used to augment the performance of a human operator or an autonomously operated crane [9, 10]. Open-loop feedforward control methods that rely on input-shaping of the reference commands sent to the crane are well-studied [11–16], and are particularly useful in preventing sway of the crane's hoist cable caused by human operator. A comparison of different input-shaping methods can be found in [17]. Off-line motion planning methods that involve preliminary trolley/payload trajectory design smoothing out the motion of the payload swaying [18–22] are particularly useful in autonomous and periodic crane operation.

Advanced closed-loop control methods including gain scheduling [23], sliding-mode control [24, 25], and integral-sliding-mode control [26] have been proposed for the trajectory tracking control of tower crane payloads over a range of operating conditions, including variations in hoist cable length and payload mass. Although these control techniques are effective in certain situations, they do not necessarily provide a guarantee of robust closed-loop stability [23] or the ability to track payload velocity trajectories [6]. A number of tower crane control methods have been proposed to explicitly account for model uncertainty or unknown external

disturbances. In particular, disturbance rejection solutions include implementing a disturbance observer [27], adding a damping anti-swing signal [28], and combining open-loop input-shaping technique and closed-loop feedback disturbance rejection control [29]. Unmodeled crane dynamics and unknown payload mass can be addressed by adaptive output feedback control [30] and adaptive sliding-mode control [31, 32] methods. The practical issues of discrete-time tower crane control has also been investigated in [26, 33].

1.2 Thesis Objectives, Outline, and Contributions

Although the existing control techniques are effective in certain situations, they do not cover all the problems for an autonomous tower crane. The off-line motion planning methods usually do not consider flexibility of cable, then the noncolocation problem are omitted [18–22]. The adaptive sliding-mode control methods require precise knowledge of the system's mass properties [31, 32]. This thesis aims to find a solution to achieving quick payload maneuver trajectory with reduced oscillations, and ensuring applicability to autonomous tower cranes that feature noncolocation, underactuation, and uncertain dynamics.

A dynamic model of a two-dimensional tower crane with a flexible hoist cable and two degrees-of-freedom (2 DOF) is derived in Chapter 2, accounting for the winch inertia and the axial cable stiffness that varies with the length of the cable using a Rayleigh-Ritz discretization approach inspired by [34–36]. The proposed model more accurately represents the axial stiffness of a hoist cable compared to the linear spring used in [6], and allows for varying degrees of fidelity by adjusting the number of Ritz basis functions used. The state-dependent basis functions used in the discretization based on the work of [36] gives a computationally-efficient model to the length varying flexible cable. Passivity-based control approaches are employed to perform trajectory tracking of a tower crane's payload in Chapters 3

and 4. In contrast to Lyapunov-based control methods that focus on asymptotic stability of system states, passivity-based control is centered around the notion of input-output stability. In simple terms, a system is considered input-output stable if well-behaved inputs result in well-behaved outputs. Specifically, this thesis is concerned with a particular type of input-output stability known as input-output $\mathcal{L}_2$ stability, where input in the inner-product space $\mathcal{L}_2$ guarantee outputs in the same inner product space $\mathcal{L}_2$. A connection between passivity-based input-output stability and Lyapunov stability analysis is found using a storage function [37]. The Passivity Theorem [37], which is given in Section 1.3, guarantees closed-loop input-output stability of a negative feedback involving a passive system and an input strictly passive (ISP) controller.

Passivity-based methods are widely used for the motion control of robotic manipulators, where the control inputs are colocated with the measurement outputs (e.g., the input-output mapping from joint torques to joint rates is passive). Dynamic systems with noncolocated actuators and sensors typically do not feature a passive input-output mapping. The μ-tip rate was defined in [38] to modify the noncolocated actuator/sensor pair of a flexible robotic manipulator with a heavy payload, resulting in a passive input-output mapping. The μ-tip rate has been implemented in a variety of flexible robotic systems, including a flexible gantry robot [39] and cable driven parallel robots [36, 40, 41]. Within these applications, passivity-based control provides a rigorous robust guarantee of closed-loop input-output stability, which is not always possible with other nonlinear control techniques, such as gain scheduling [23]. This motivates the use of the μ-tip rate and passivity-based control for the control of tower cranes, in an effort to overcome robustness and performance limitations of closed-loop control techniques for cranes in the literature. Chapter 3 uses the μ-tip approach to address the noncolocated actuation issue. The μ-tip rate used in [36, 40, 41] for cable-driven parallel robots and [39] for a gantry robot is leveraged to establish a passive input-output mapping from modified force and torque inputs of the crane to an output that is formed from the position and velocity tracking error of the crane's payload.

A significant novel contribution of the work in Chapter 3 compared to previous implementations of the μ-tip rate [36, 38–42] is that the rigid-body sway angle of the crane's hoist cable is considered as a flexible coordinate. In this work it is assumed that the sway angle and sway angle rate are small, which is justified by the fact that gravity will act as a nonlinear spring and cause the hoist cable to vibrate about its equilibrium position. The use of the μ-tip rate for trajectory tracking of the crane's payload greatly simplifies the task of designing a stabilizing feedback controller. In Chapter 3, the sway angle θ is considered as a flexible coordinate, and using a μ-tip approach to maintain passivity mapping from the input force and torque to the output μ-tip rate of payload behavior.

The μ-tip control method proposed in Chapter 3 relies on assumptions that the sway angle and its angular rate remain small, which is very restrictive in practice. In order to solve this issue, passivity-base adaptive sliding-mode-inspired approach is presented in Chapter 4. The adaptive sliding-mode control method in [31, 32] is used as inspiration, where the underactuated system is separated into actuated and unactuated parts, and sliding-mode control is used to account for the unactuated sway of the crane's payload. The proposed approach does not require assumptions on the size of the sway angle or sway angular rate, and provides a practical control alternative to the μ-tip approach in Chapter 3. Compared to the method in [31, 32], the proposed approach uses passivity theory uses Passivity Theorem to prove closed-loop input-output stability rather than a Lyapunov approach, and makes use of a more general adaptation law [42, 43] that does not rely on a model-specific adaptation law or precise knowledge of the payload mass, as in [32].

Additionally, the novel passivity-based adaptive sliding-mode control method is implemented in the payload trajectory aspect that allows the controller to be more intuitively designed in the task space. Experiments are presented in Chapter 5 based on the passivity-based adaptive sliding-mode-inspired control method in Chapter 4 implemented on the Quanser 3 DOF crane [2]. The control theory developed in this thesis is not limited to only tower cranes, and can be extended

to cable-driven robots and flexible robotic manipulators.

1.3 Preliminaries

1.3.1 Vectrix Notation

Vectrix notation defined in [44, 45] is used throughout this thesis. For example, the position vector $\underrightarrow{r}^{ij}$ describing the position of point j relative to point i is denoted by

$$\begin{aligned}\underrightarrow{r}^{ij} &= r_{a1}^{ij}\underrightarrow{a}^{1} + r_{a2}^{ij}\underrightarrow{a}^{2} + r_{a3}^{ij}\underrightarrow{a}^{3} \\ &= \begin{bmatrix}\underrightarrow{a}^{1} & \underrightarrow{a}^{2} & \underrightarrow{a}^{3}\end{bmatrix}\begin{bmatrix} r_{a1}^{ij} \\ r_{a2}^{ij} \\ r_{a3}^{ij}\end{bmatrix} \\ &= \underrightarrow{\boldsymbol{\mathcal{F}}}_a{}^{\mathsf{T}}\mathbf{r}_a^{ij}\end{aligned}$$

where $\underrightarrow{\boldsymbol{\mathcal{F}}}_a = \begin{bmatrix}\underrightarrow{a}^{1} & \underrightarrow{a}^{2} & \underrightarrow{a}^{3}\end{bmatrix}^{\mathsf{T}}$ is a column matrix of three orthonormal basis vectors $\underrightarrow{a}^{1}$, $\underrightarrow{a}^{2}$, $\underrightarrow{a}^{3}$ that define reference frame $\mathcal{F}_a$, and $\mathbf{r}_a^{ij} = \begin{bmatrix} r_{a1}^{ij} & r_{a2}^{ij} & r_{a3}^{ij}\end{bmatrix}^{\mathsf{T}}$ is a column matrix of scalars containing the components of $\underrightarrow{r}^{ij}$ resolved in $\mathcal{F}_a$. The time derivative of $\underrightarrow{r}^{ij}$ is denoted by $\underrightarrow{r}^{ij\,\bullet a} = \underrightarrow{\boldsymbol{\mathcal{F}}}_a{}^{\mathsf{T}}\dot{\mathbf{r}}_a^{ij}$, or it can be written as $\underrightarrow{v}^{ij/a} = \underrightarrow{r}^{ij\,\bullet a} = \underrightarrow{\boldsymbol{\mathcal{F}}}_a{}^{\mathsf{T}}\mathbf{v}_a^{ij/a}$ if it represents a velocity. The dot product of two vectors $\underrightarrow{u}$ and $\underrightarrow{v}$ is

$$\begin{aligned}\underrightarrow{u}\cdot\underrightarrow{v} &= \left(\underrightarrow{\boldsymbol{\mathcal{F}}}_a{}^{\mathsf{T}}\mathbf{u}_a\right)\cdot\left(\underrightarrow{\boldsymbol{\mathcal{F}}}_a{}^{\mathsf{T}}\mathbf{v}_a\right) \\ &= \mathbf{u}_a^{\mathsf{T}}\left(\underrightarrow{\boldsymbol{\mathcal{F}}}_a\cdot\underrightarrow{\boldsymbol{\mathcal{F}}}_a{}^{\mathsf{T}}\right)\mathbf{v}_a \\ &= \mathbf{u}_a^{\mathsf{T}}\,\mathbf{1}\,\mathbf{v}_a \\ &= \mathbf{u}_a^{\mathsf{T}}\mathbf{v}_a = \mathbf{v}_a^{\mathsf{T}}\mathbf{u}_a,\end{aligned}$$

and is a frame-invariant computation, as the same result is obtained using the components of $\underrightarrow{u}$ and $\underrightarrow{v}$ resolved in $\underrightarrow{\boldsymbol{\mathcal{F}}}_b$, i.e. $\underrightarrow{u} \cdot \underrightarrow{v} = \mathbf{u}_b^{\mathsf{T}} \mathbf{v}_b = \mathbf{v}_b^{\mathsf{T}} \mathbf{u}_b$. The cross product of two vectors $\underrightarrow{u}$ and $\underrightarrow{v}$ resolved in $\underrightarrow{\boldsymbol{\mathcal{F}}}_a$ is

$$\begin{aligned} \underrightarrow{u} \times \underrightarrow{v} &= \left(\underrightarrow{\boldsymbol{\mathcal{F}}}_a{}^{\mathsf{T}} \mathbf{u}_a \right) \times \left(\underrightarrow{\boldsymbol{\mathcal{F}}}_a{}^{\mathsf{T}} \mathbf{v}_a \right) \\ &= \underrightarrow{\boldsymbol{\mathcal{F}}}_a{}^{\mathsf{T}} \mathbf{u}_a^{\times} \mathbf{v}_a, \end{aligned}$$

where $\mathbf{u}_a^{\times} = \begin{bmatrix} u_{a,1} \\ u_{a,2} \\ u_{a,3} \end{bmatrix}^{\times} = \begin{bmatrix} 0 & -u_{a,3} & u_{a,2} \\ u_{a,3} & 0 & -u_{a,1} \\ -u_{a,2} & u_{a,1} & 0 \end{bmatrix}$ is the cross-product operator matrix corresponding to vector $\underrightarrow{u}$ resolved in $\underrightarrow{\boldsymbol{\mathcal{F}}}_a$. Also, $\underrightarrow{u} \times \underrightarrow{v} = \underrightarrow{\boldsymbol{\mathcal{F}}}_b{}^{\mathsf{T}} \mathbf{u}_b^{\times} \mathbf{v}_b$ denotes the cross product of $\underrightarrow{u}$ and $\underrightarrow{v}$ resolved in $\underrightarrow{\boldsymbol{\mathcal{F}}}_b$.

The direction cosine matrix (DCM), also called the orientation matrix, is used to operate the change of reference frame (change of coordinates). For example,

$$\mathbf{v}_b = \mathbf{C}_{ba} \mathbf{v}_a,$$

where

$$\mathbf{C}_{ba} = \underrightarrow{\boldsymbol{\mathcal{F}}}_b \cdot \underrightarrow{\boldsymbol{\mathcal{F}}}_a{}^{\mathsf{T}} = \begin{bmatrix} \underrightarrow{b}^1 \cdot \underrightarrow{a}^1 & \underrightarrow{b}^1 \cdot \underrightarrow{a}^2 & \underrightarrow{b}^1 \cdot \underrightarrow{a}^3 \\ \underrightarrow{b}^2 \cdot \underrightarrow{a}^1 & \underrightarrow{b}^2 \cdot \underrightarrow{a}^2 & \underrightarrow{b}^2 \cdot \underrightarrow{a}^3 \\ \underrightarrow{b}^3 \cdot \underrightarrow{a}^1 & \underrightarrow{b}^3 \cdot \underrightarrow{a}^2 & \underrightarrow{b}^3 \cdot \underrightarrow{a}^3 \end{bmatrix}$$

is the DCM that describes the orientation of $\mathcal{F}_b$ relative to $\mathcal{F}_a$, and can be used to relate the components of $\underrightarrow{v}$ resolved in $\mathcal{F}_a$ to the components of $\underrightarrow{v}$ resolved in $\mathcal{F}_b$.

1.3.2 Passivity Theory

The input-output stability analysis in Chapters 3 and 4 rely heavily on the passivity theorem. The required preliminary knowledge is provided in this section.

Definition 1 (Lebesgue Space [46])**.** *The Lebesgue space, $\mathcal{L}_2$, is an inner product*

space, and is given by all square integral functions defined by

$$\mathcal{L}_2 = \left\{ \mathbf{u} : \mathbb{R}_{\geq 0} \to \mathbb{R}^n \;\middle|\; \|\mathbf{u}\|_2^2 = \int_0^\infty \mathbf{u}^\mathsf{T}(t)\mathbf{u}(t)\mathrm{d}t < \infty \right\}.$$

The extended Lebesgue space, $\mathcal{L}_{2e}$, also known as the extended $\mathcal{L}_2$ inner product space, is a space of square integral functions defined by

$$\mathcal{L}_{2e} = \left\{ \mathbf{u} : \mathbb{R}_{\geq 0} \to \mathbb{R}^n \;\middle|\; \|\mathbf{u}\|_{2T}^2 = \int_0^T \mathbf{u}^\mathsf{T}(t)\mathbf{u}(t)\mathrm{d}t < \infty,\ \forall T \in \mathbb{R}_{\geq 0} \right\}.$$

Definition 2 ($\mathcal{L}_\infty$ Space [46])**.** *The $\mathcal{L}_\infty$ space is a space of functions that have a finite $\mathcal{L}_\infty$ norm defined by function $\mathbf{u} \in \mathcal{L}_\infty$ if*

$$\|\mathbf{u}\|_\infty = \sup_{t \in \mathbb{R}_{\geq 0}} \left[\max_{i=1,\ldots,n} |u_i(t)| \right] < \infty,$$

where $\mathbf{u}^\mathsf{T}(t) = \begin{bmatrix} u_1(t) & \cdots & u_n(t) \end{bmatrix}$.

Definition 3 (Truncated Signals)**.** *A truncated signal $\mathbf{x}_T(t)$ is defined for any $T \in [0, \infty)$ as*

$$\mathbf{x}_T(t) = \begin{cases} \mathbf{x}(t), & \text{if } 0 \leq t \leq T, \\ 0, & \text{if } t > T. \end{cases}$$

Definition 4 (Passive System [47])**.** *The mapping $\mathbf{u} \mapsto \mathbf{y}$ associated with the operator $\mathcal{G} : \mathcal{L}_{2e} \to \mathcal{L}_{2e}$, where $\mathbf{y} = \mathcal{G}\mathbf{u}$, is passive if there exists β such that*

$$\int_0^T \mathbf{y}^\mathsf{T}(t)\mathbf{u}(t)\mathrm{d}t \geq \beta \quad \forall \mathbf{u} \in \mathcal{L}_{2e},\ T \in \mathbb{R}^+.$$

Definition 5 (Input Strictly Passive (ISP) System [47])**.** *The mapping $\mathbf{u} \mapsto \mathbf{y}$ associated with the operator $\mathcal{G} : \mathcal{L}_{2e} \to \mathcal{L}_{2e}$, where $\mathbf{y} = \mathcal{G}\mathbf{u}$, is input strictly passive*

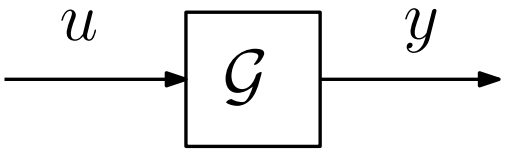

Figure 1.2: Block diagram for passive mapping.

(ISP) if there exists a β *and* $0 < \delta < 1$ *such that*

$$\int_0^T \mathbf{y}^\mathsf{T}(t)\mathbf{u}(t)\mathrm{d}t \geq \delta \int_0^T \mathbf{u}^\mathsf{T}(t)\mathbf{u}(t)\mathrm{d}t + \beta \quad \forall \mathbf{u} \in \mathcal{L}_{2e},\ T \in \mathbb{R}^+.$$

Theorem 1 (Passivity Theorem [46])**.** *Let* $\mathcal{G}_1, \mathcal{G}_2 : \mathcal{L}_{2e} \to \mathcal{L}_{2e}$*, and consider the negative feedback interconnection defined by*

$$u_1 = r_1 - \mathcal{G}_2 u_2,$$
$$y_1 = \mathcal{G}_1 u_1,$$

as shown in Figure 1.3. Under these conditions, if $\mathcal{G}_1$ *is passive and* $\mathcal{G}_2$ *is input strictly passive (ISP), then* $y_1 \in \mathcal{L}_2$ *for every* $r_1 \in \mathcal{L}_2$*.*

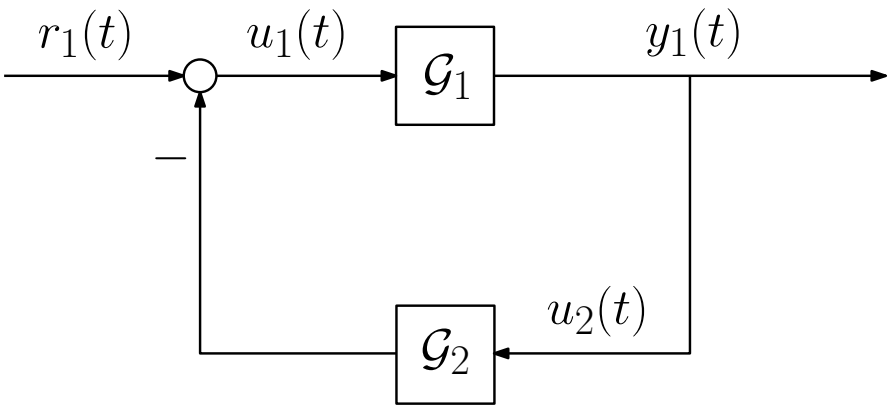

Figure 1.3: Block diagram for Passivity Theorem.

Lemma 1 (Barbalat's Lemma [37]). *If the differentiable function $f(\cdot)$ has a finite limit as $t \to \infty$, and if $\dot{f}(\cdot)$ is uniformly continuous, then $\dot{f}(\cdot) \to 0$ as $t \to \infty$.*

Lemma 2 (Lemma 4.8 in [37]). *Consider the state space representation of a linear invariant system $\dot{x}(t) = Ax(t) + Bu(t)$, with $u(t) \in \mathbb{R}^m$, $x(t) \in \mathbb{R}^n$ and A exponentially stable. If $u \in \mathcal{L}_2$ then $x \in \mathcal{L}_2 \cap \mathcal{L}_\infty$, $\dot{x} \in \mathcal{L}_2$ and $\lim_{t \to +\infty} x(t) = 0$.*

Note that the system above with $u \in \mathcal{L}_2$ does not necessarily have an equilibrium point.

Theorem 2 (Theorem 4.10 in [37], p. 59 in [47]). *Consider the exponentially stable and strictly proper system*

$$\begin{cases} \dot{x}(t) = Ax(t) + Bu(t) \\ y(t) = Cx(t), \end{cases}$$

and its transfer function $H(s) = C\left(I_n - A\right)^{-1} B$. If $u \in \mathcal{L}_p$, then $y = h * u \in \mathcal{L}_p \cap \mathcal{L}_\infty$, $\dot{y} \in \mathcal{L}_p$ for $p = 1, 2$ and ∞. The function $h(\cdot)$ is the inverse Laplace transform of $H(s)$, and the symbol $*$ is the convolution product. For $p = 1, 2$, then $\lim_{t \to +\infty} y(t) = 0$.

Chapter 2

Dynamic Modeling of a 2 DOF Crane with a Flexible Hoist Cable

2.1 Introduction

This chapter presents a finite-dimensional dynamic model of a two-dimensional tower crane with a flexible hoist cable. The remainder of this section features an introduction to the notation used in the derivation of the dynamic model. Section 2.2 includes an overview of the two-dimensional crane that is to be modeled. Section 2.3 presents details of the Rayleigh-Ritz discretization used to model the elasticity of the crane's flexible hoist cable. State-dependent basis functions are used in the discretization based on the work of [36], which result in a computationally-efficient model. The derivation of the crane's kinetic and potential energies is given in Section 2.4, and is used to derive the crane's dynamic model following a Lagrangian approach in Section 2.5.

2.2 2 DOF Crane Model

Consider the two-dimensional tower crane shown in Figure 2.1. The crane has trolley mass m_1, winch mass m_w, payload mass m_2, and a flexible hoist cable with

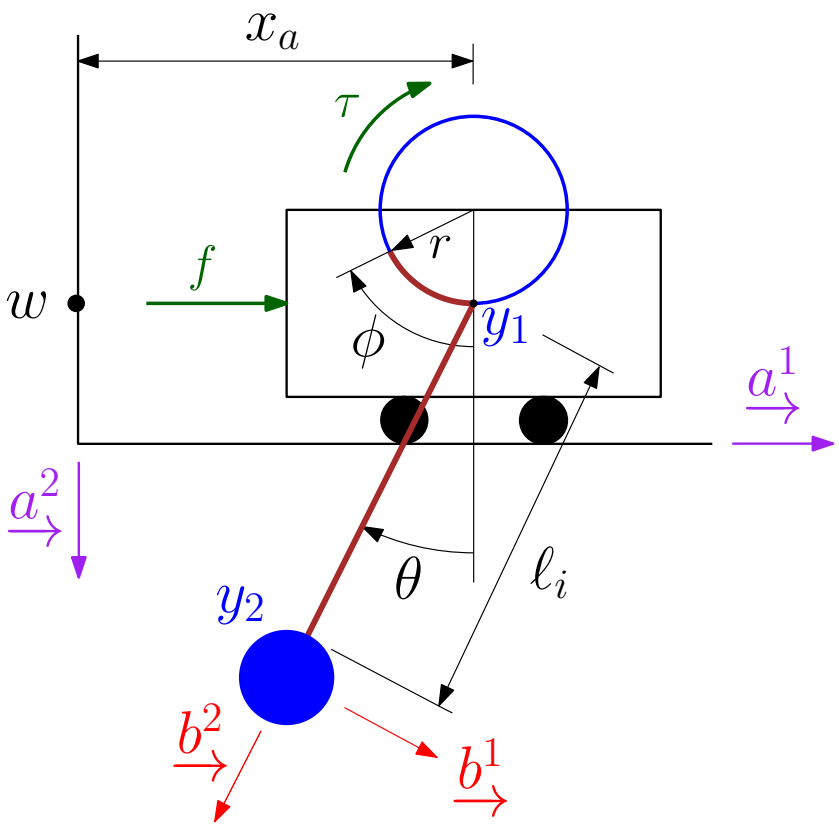

Figure 2.1: Schematic of a two-dimensional tower crane with the reference frames and generalized coordinates.

cross-sectional area A, and density ρ_c. The cable is wrapped around the winch drum and attached to the payload. An inertial reference frame $\mathcal{F}_a$ is defined by basis vectors $\underset{\rightarrow}{a}^1$, $\underset{\rightarrow}{a}^2$, $\underset{\rightarrow}{a}^3$. The winch's center of mass is colocated with the trolley's center of mass, neglecting any shift in center of mass due to the winding of the cable, and is denoted by y_1. An external horizontal force f in the $\underset{\rightarrow}{a}^1$ direction is applied to the trolley as an input. The horizontal distance between y_1 and stationary point w is x_a. The winch has radius r, and the cable attachment point is assumed to be colocated with y_1. The winch rotation is described by the angle ϕ, and is actuated by the torque τ. The payload, denoted as point y_2, is modeled as a point mass connected to the winch by the cable. The angle θ denotes the clockwise sway angle of the cable and the payload about the $\underset{\rightarrow}{a}^3$ axis.

The nominal initial length L defines the length of cable between the winch and payload when $\phi = 0$. The instantaneous length of cable between the payload and the winch, neglecting the flexibility of the cable, is given by $\ell_i = L - r\phi$. The spatial coordinate x denotes the location of an infinitesimal mass element of the continuous cable, and varies from $x = L - \ell_i$ at the point where the cable is fixed to the winch drum to $x = L$ at the end of the cable, as shown in Figure 2.2a. The modeling approach used in this thesis assumes that the cable does not go slack, and the cross-sectional shape is preserved while vibrating. Disregarding the elasticity of the cable, the rigid generalized coordinates of the tower crane are given by $\mathbf{q}^\mathsf{T} = \begin{bmatrix} x_a & \phi & \theta \end{bmatrix}$.

2.3 Rayleigh-Ritz Discretization

The hoist cable is a elastic continuum, whose vibrations can be described by partial differential equations (PDEs). PDEs are complicated to solve, and do not tend to be particularly amenable to feedback control design. For control purposes, we prefer to work with finite-dimensional ordinary differential equations (ODEs). To this end, we require a spatial discretization of the hoist cable to convert the PDEs into ODEs.

A Rayleigh-Ritz discretization is used to modeled the axial vibrations of the flexible hoist cable. Consider two infinitesimally small pulleys fixed beneath the winch such that the upper end of the flexible cable is fixed to the bottom of the winch, as shown in Figure 2.2a, and neglect any curving or bending of the cable due to the pulleys. The angle β is a spatial variable used to define the angular position of the mass element of the cable that is reeled on the winch drum, which will be used in Section 2.4.2 when deriving the kinetic energy stored in the winch drum.

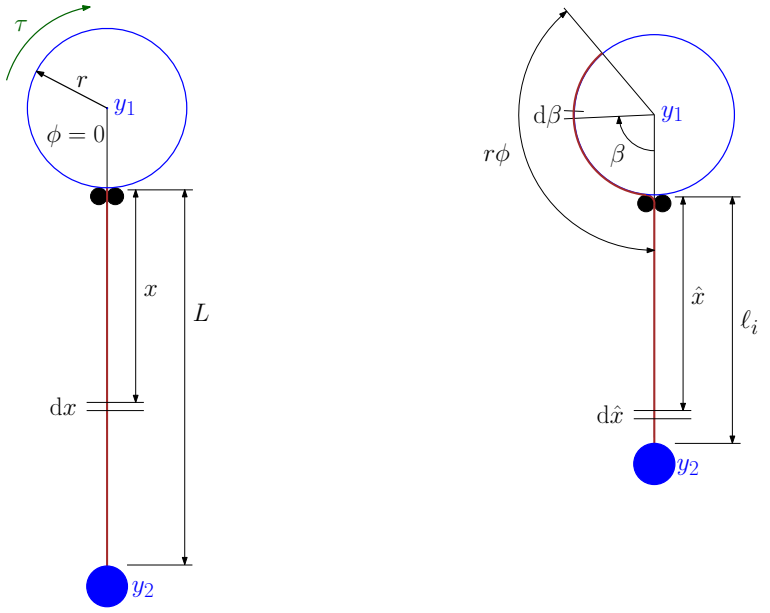

(a) unwound cable (b) length varying cable

Figure 2.2: Schematic of a two-dimensional tower crane, where (a) presents the unwound cable and (b) illustrates the variation in the length of the hoist cable based on its winding about the trolley winch.

The elastic displacement of any mass element on the flexible cable is described by

$$u(x,t) = \mathbf{\Psi}(x)\,\mathbf{q}^e(t)\,,$$

where $\mathbf{\Psi}(x)$ are the spatially-dependent Ritz basis functions and $\mathbf{q}^e(t)$ are time-dependent elastic coordinates describing the vibration modes. The Ritz basis

functions, referred to simply as basis functions, are arbitrarily chosen, provided they satisfy the boundary conditions, and are conventionally taken to be time-independent.

The varying length of the cable and the reeling motion of the winch are essential to the modeling of the tower crane system. Since the length of the flexible portion of cable ℓ_i is time-varying, it is necessary to include $\ell_i(t)$ in the state-dependent basis functions to ensure the boundary condition of $u(L-\ell_i,t)=0$, where the elastic displacement at $x=L-\ell_i$ is zero. Additionally, it has been shown that there is a computational advantage to using state-dependent basis functions when the boundary conditions depend on the state [34–36]. Using the approach described in [36], the elastic deformation of the cable at any point between the winch and the payload is given by

$$u(x,t)=\boldsymbol{\Psi}\left(x,\ell_i(t)\right)\mathbf{q}^e\left(t\right),\forall x\in[L-\ell_i,L],$$

where $\mathbf{q}^e\left(t\right)$ contains time-dependent elastic coordinates and $\boldsymbol{\Psi}\left(x,\ell_i(t)\right)$ contains state-dependent basis functions, and is shortened as $\boldsymbol{\Psi}\left(x,\ell_i\right)$ or $\boldsymbol{\Psi}$ for the remainder of this thesis. In the interest of brevity, the temporal argument t is also removed from time-dependent quantities, except when required for clarity. The chosen basis functions are [34–36]

$$\boldsymbol{\Psi}\left(x,\ell_i\right)=\begin{bmatrix}\sin\left(\frac{\pi(x-L+\ell_i)}{2\ell_i}\right) & \sin\left(2\frac{\pi(x-L+\ell_i)}{2\ell_i}\right) & \sin\left(3\frac{\pi(x-L+\ell_i)}{2\ell_i}\right) & \dots\end{bmatrix}. \tag{2.1}$$

It is worth noting that [36]

$$\dot{\boldsymbol{\Psi}}\left(x,\ell_i\right)=\frac{\partial\boldsymbol{\Psi}\left(x,\ell_i\right)}{\partial\ell_i}\frac{\partial\ell_i}{\partial t}=-r\dot{\phi}\frac{\partial\boldsymbol{\Psi}\left(x,\ell_i\right)}{\partial\ell_i}.$$

The generalized coordinates of the tower crane with a flexible hoist cable are now given by $\mathbf{q}^{\mathsf{T}}=\begin{bmatrix}x_a & \phi & \theta & \mathbf{q}^{e\mathsf{T}}\end{bmatrix}$, which includes the elastic coordinates.

2.4 Kinetic and Potential Energies

A Lagrangian approach is to be used to derive the system's equations of motion, which requires the kinetic and potential energies of the system. The full system is separated into components defined by the payload, cable, winch and trolley. Vectrix notation and the Transport Theorem are used to derive the kinetic and potential energies of the individual components, and are then added together in Section 2.4.4. Specifically, Section 2.4.1 uses a Rayleigh-Ritz discretization as mentioned in Section 2.3 and the chosen basis functions (2.1) to model the flexible hoist cable, Section 2.4.2 derives the rotational and translational energy of the winch and trolley, Section 2.4.3 uses the boundary condition $\hat{x} = \ell_i$ located at the rear end of the flexible cable to derive the kinetic and potential energies of the payload.

2.4.1 Unwound Cable

The flexible portion of the cable has an instantaneous length ℓ_i that depends on the winch angle ϕ, which results in state-dependent boundary conditions on the spatial coordinate x. It is therefore beneficial to define the state-dependent spatial coordinate $\hat{x} \in [0, \ell_i]$, where $\hat{x} = x - r\phi$ is the shifted position of x lying between y_1 and y_2, such that $\hat{x} = 0$ is located at y_1 and $\hat{x} = \ell_i$ is located at y_2, as shown in Figure 2.2b. Consider the infinitesimal mass element $\mathrm{d}m$ at position $\hat{x}$ located between y_1 and y_2, whose position and velocity relative to point w, with the velocity taken with respect to $\mathcal{F}_a$, resolved in $\mathcal{F}_a$ are

$$
\begin{aligned}
\underrightarrow{r}^{\mathrm{d}mw} &= \underrightarrow{r}^{\mathrm{d}my_1} + \underrightarrow{r}^{y_1w} \\
&= \underrightarrow{\boldsymbol{\mathcal{F}}}_a{}^{\mathsf{T}} \left(\mathbf{C}_{ab} \mathbf{r}_b^{\mathrm{d}my_1} + \mathbf{r}_a^{y_1w} \right) = \underrightarrow{\boldsymbol{\mathcal{F}}}_a{}^{\mathsf{T}} \mathbf{r}_a^{\mathrm{d}mw}, \\
\underrightarrow{v}^{\mathrm{d}mw/a} &= \underrightarrow{r}^{\mathrm{d}mw\,\bullet a} \\
&= \underrightarrow{\boldsymbol{\mathcal{F}}}_a{}^{\mathsf{T}} \dot{\mathbf{r}}_a^{\mathrm{d}mw} = \underrightarrow{\boldsymbol{\mathcal{F}}}_a{}^{\mathsf{T}} \mathbf{v}_a^{\mathrm{d}mw/a},
\end{aligned}
$$

where

$$\begin{aligned}
\mathbf{r}_a^{\mathrm{d}mw} &= \underrightarrow{\mathcal{F}}_a{}^{\mathsf{T}} \left(\mathbf{C}_{ab} \mathbf{r}_b^{\mathrm{d}my_1} + \mathbf{r}_a^{y_1 w} \right) \\
&= \begin{bmatrix} \cos\theta & -\sin\theta & 0 \\ \sin\theta & \cos\theta & 0 \\ 0 & 0 & 1 \end{bmatrix} \begin{bmatrix} 0 \\ \hat{x} + \mathbf{\Psi}\mathbf{q}^e \\ 0 \end{bmatrix} + \begin{bmatrix} x_a \\ 0 \\ 0 \end{bmatrix} \\
&= \begin{bmatrix} x_a - \sin\theta \left(\hat{x} + \mathbf{\Psi}\mathbf{q}^e \right) \\ \cos\theta \left(\hat{x} + \mathbf{\Psi}\mathbf{q}^e \right) \\ 0 \end{bmatrix}, \qquad (2.2) \\
\mathbf{v}_a^{\mathrm{d}mw/a} &= \begin{bmatrix} \dot{x}_a - \cos\theta\dot{\theta} \left(\hat{x} + \mathbf{\Psi}\mathbf{q}^e \right) + \sin\theta \dot{P}_x \\ -\sin\theta\dot{\theta} \left(\hat{x} + \mathbf{\Psi}\mathbf{q}^e \right) - \cos\theta \dot{P}_x \\ 0 \end{bmatrix}, \qquad (2.3) \\
\dot{P}_x &= \frac{\mathrm{d}}{\mathrm{d}t} \left(\hat{x} + \mathbf{\Psi}\mathbf{q}^e \right) = \left(r\dot{\phi} \left(1 + \frac{\partial \mathbf{\Psi}}{\partial \ell_i} \mathbf{q}^e \right) - \mathbf{\Psi}\dot{\mathbf{q}}^e \right).
\end{aligned}$$

The kinetic energy of the unwound cable relative to point w with respect to $\mathcal{F}_a$ is

$$\begin{aligned}
T_{cw/a} &= \tfrac{1}{2} \rho_c A \int_0^{\ell_i} \mathbf{v}_a^{\mathrm{d}mw/a\mathsf{T}} \mathbf{v}_a^{\mathrm{d}mw/a} \mathrm{d}\hat{x} \\
&= \tfrac{1}{2} \dot{\mathbf{q}}^{\mathsf{T}} \mathbf{M}_{cw} \dot{\mathbf{q}},
\end{aligned}$$

where

$$\mathbf{M}_{cw} = \rho_c A \begin{bmatrix} \ell_i & M_{12}^{cw} & M_{13}^{cw} & M_{14}^{cw} \\ * & M_{22}^{cw} & 0 & M_{24}^{cw} \\ * & * & M_{33}^{cw} & 0 \\ * & * & * & \ell_i \mathbf{\Lambda}_{22} \end{bmatrix},$$

$$\begin{aligned}
M_{12}^{cw} &= r \sin\theta \left(\ell_i + \mathbf{\Lambda}_1 \mathbf{q}^e \right), & M_{22}^{cw} &= r^2 \left(\ell_i + 2\mathbf{\Lambda}_1 \mathbf{q}^e + \mathbf{q}^e \frac{\mathbf{\Lambda}_{11}}{\ell_i} \mathbf{q}^e \right), \\
M_{13}^{cw} &= -\cos\theta \left(\frac{\ell_i^2}{2} + \ell_i \mathbf{\Lambda}_2 \mathbf{q}^e \right), & M_{24}^{cw} &= -r \left(\ell_i \mathbf{\Lambda}_2 + \mathbf{q}^{e\mathsf{T}} \mathbf{\Lambda}_{12} \right), \\
M_{14}^{cw} &= -\sin\theta \ell_i \mathbf{\Lambda}_2, & M_{33}^{cw} &= \frac{\ell_i^3}{3} + 2\ell_i^2 \mathbf{\Lambda}_{21} \mathbf{q}^e + \mathbf{q}^{e\mathsf{T}} \ell_i \mathbf{\Lambda}_{22} \mathbf{q}^e.
\end{aligned}$$

The symbol "$*$" represents the transpose of repeated blocks within the symmetric matrix, and the following matrices are constant [36].

$$\begin{aligned}
\mathbf{\Lambda}_1 &= \int_0^{\ell_i} \frac{\partial \mathbf{\Psi}}{\partial \ell_i} \mathrm{d}\hat{x}, & \mathbf{\Lambda}_2 &= \frac{1}{\ell_i} \int_0^{\ell_i} \mathbf{\Psi} \mathrm{d}\hat{x}, \\
\mathbf{\Lambda}_{11} &= \ell_i \int_0^{\ell_i} \frac{\partial \mathbf{\Psi}^{\mathsf{T}}}{\partial \ell_i} \frac{\partial \mathbf{\Psi}}{\partial \ell_i} \mathrm{d}\hat{x}, & \mathbf{\Lambda}_{22} &= \frac{1}{\ell_i} \int_0^{\ell_i} \mathbf{\Psi}^{\mathsf{T}} \mathbf{\Psi} \mathrm{d}\hat{x}, \\
\mathbf{\Lambda}_{12} &= \int_0^{\ell_i} \frac{\partial \mathbf{\Psi}^{\mathsf{T}}}{\partial \ell_i} \mathbf{\Psi} \mathrm{d}\hat{x}, & \mathbf{\Lambda}_{21} &= \frac{1}{\ell_i^2} \int_0^{\ell_i} \mathbf{\Psi} \hat{x} \mathrm{d}\hat{x}.
\end{aligned}$$

The somewhat unconventional choice of state-dependent basis functions in (2.1) ensures that these matrices are constant, and improves the computational efficiency of the dynamic model.

The cable is considered to be a linear elastic material with elastic strain energy $V_{cs} = \int U_0 \mathrm{d}V$, where $U_0 = \frac{1}{2}\sigma\epsilon$ is the strain density, $\sigma = E\epsilon$ is the longitudinal stress, E is the Young's modulus, and the local strain is

$$\epsilon(x,t) = \frac{\partial u(x,t)}{\partial x} = \frac{\partial \mathbf{\Psi}(x,\ell_i)}{\partial x} \mathbf{q}^e(t).$$

The strain energy stored in the cable is expressed as

$$\begin{aligned}
V_{cs} &= \int \tfrac{1}{2} E \epsilon^2 \mathrm{d}V \\
&= \tfrac{1}{2} \int_{\ell_i}^{L-\ell_i} E \left(\frac{\partial \mathbf{\Psi}}{\partial x} \mathbf{q}^e \right)^{\mathsf{T}} \left(\frac{\partial \mathbf{\Psi}}{\partial x} \mathbf{q}^e \right) A \mathrm{d}x \\
&= \tfrac{1}{2} \int_0^{\ell_i} E \left(\frac{\partial \mathbf{\Psi}}{\partial \hat{x}} \mathbf{q}^e \right)^{\mathsf{T}} \left(\frac{\partial \mathbf{\Psi}}{\partial \hat{x}} \mathbf{q}^e \right) A \mathrm{d}\hat{x} \\
&= \tfrac{1}{2} \mathbf{q}^{e\mathsf{T}} \left(EA \int_0^{\ell_i} \frac{\partial \mathbf{\Psi}^{\mathsf{T}}}{\partial \hat{x}} \frac{\partial \mathbf{\Psi}}{\partial \hat{x}} \mathrm{d}\hat{x} \right) \mathbf{q}^e \\
&= \tfrac{1}{2} \mathbf{q}^{\mathsf{T}} \mathbf{K} \mathbf{q},
\end{aligned}$$

where $\mathbf{K} = \text{diag}\{\mathbf{0}, \mathbf{K}_{ee}\}$ is a stiffness matrix, $\mathbf{K}_{ee} = EA\mathbf{\Lambda}_{33}/\ell_i$, and

$$\mathbf{\Lambda}_{33} = \ell_i \int_0^{\ell_i} \frac{\partial \mathbf{\Psi}^\mathsf{T}}{\partial \hat{x}} \frac{\partial \mathbf{\Psi}}{\partial \hat{x}} \mathrm{d}\hat{x}$$

is a constant matrix. The gravitational potential energy of the cable relative to point w is

$$V_{cg} = -\int_c \mathbf{g}_a^\mathsf{T} \mathbf{r}_a^{\mathrm{d}mw} \mathrm{d}m = -\rho_c A g \cos\theta \left(\frac{\ell_i^2}{2} + \ell_i \mathbf{\Lambda}_2 \mathbf{q}^e \right),$$

where $\mathbf{g}_a^\mathsf{T} = \begin{bmatrix} 0 & g & 0 \end{bmatrix}$ and $g = 9.81$ m/s^2 is Earth's gravitational constant.

2.4.2 Winch and Trolley

Including the cable wrapped around the winch, the combined mass of the winch and trolley is $m_{y_1} = m_1 + m_w + \rho_c A r \phi$. The translational energy and potential energy are

$$\begin{aligned} T_{\text{trans}} &= \tfrac{1}{2} m_{y_1} \mathbf{v}_a^{y_1 w/a \mathsf{T}} \mathbf{v}_a^{y_1 w/a} \\ &= \tfrac{1}{2} \left(m_1 + m_w + \rho_c A r \phi \right) \dot{x}_a^2. \end{aligned}$$

The moment of inertia of the winch disc is $I = \frac{1}{2} m_w r^2$. The moment of inertia of the cable wrapped around the winch is

$$\begin{aligned} \mathbf{J} &= -\int \mathbf{r}^\times \mathbf{r}^\times \mathrm{d}m \\ &= -\int_0^\phi \begin{bmatrix} 0 & 0 & r\cos\beta \\ 0 & 0 & r\sin\beta \\ -r\cos\beta & -r\sin\beta & 0 \end{bmatrix} \begin{bmatrix} 0 & 0 & r\cos\beta \\ 0 & 0 & r\sin\beta \\ -r\cos\beta & -r\sin\beta & 0 \end{bmatrix} \rho_c A r \mathrm{d}\beta \\ &= \rho A r^3 \int_0^\phi \begin{bmatrix} \cos^2\beta & \sin\beta\cos\beta & 0 \\ \sin\beta\cos\beta & \sin^2\beta & 0 \\ 0 & 0 & 1 \end{bmatrix} \mathrm{d}\beta \end{aligned}$$

The angular velocity of the winch relative to the inertial frame $\mathcal{F}_a$ is $\boldsymbol{\omega}^{\mathsf{T}} = \begin{bmatrix} 0 & 0 & \dot{\phi} \end{bmatrix}$, and the rotational kinetic energy of the winch is

$$\begin{aligned} T_{\text{rot}} &= \tfrac{1}{2} I \dot{\phi}^2 + \tfrac{1}{2} \boldsymbol{\omega}^{\mathsf{T}} \mathbf{J} \boldsymbol{\omega} \\ &= \tfrac{1}{2} \left(\tfrac{1}{2} m_w r^2 \right) \dot{\phi}^2 + \tfrac{1}{2} \rho_c A r^3 \phi \dot{\phi}^2. \end{aligned}$$

It is assumed the winch radius is small that the height change of the cable wrapping around the winch is negligible, which allows for the approximation that the winch and trolley does not store any gravitational potential energy. The combined kinetic energy and potential energy of the winch and trolley relative to point w with respect to $\mathcal{F}_a$ are

$$\begin{aligned} T_{y_1 w/a} &= T_{\text{trans}} + T_{\text{rot}} = \tfrac{1}{2} \dot{\mathbf{q}}^{\mathsf{T}} \mathbf{M}_{y_1 w} \dot{\mathbf{q}}, \\ V_{y_1 w/a} &= 0, \end{aligned}$$

where $\mathbf{M}_{y_1 w} = \text{diag}\{m_1 + m_w + \rho_c A r \phi, \tfrac{1}{2} m_w r^2 + \rho_c A r^3 \phi, \mathbf{0}\}$.

2.4.3 Payload

The position and velocity of the payload relative to point w, with the velocity taken with respect to $\mathcal{F}_a$, resolved in $\mathcal{F}_a$ are given by (2.2) and (2.3) evaluated at $\hat{x} = \ell_i$.

$$\mathbf{r}_a^{y_2 w} = \begin{bmatrix} x_a - \sin\theta \left(\ell_i + \boldsymbol{\Psi}_\ell \mathbf{q}^e \right) \\ \cos\theta \left(\ell_i + \boldsymbol{\Psi}_\ell \mathbf{q}^e \right) \\ 0 \end{bmatrix}, \tag{2.4}$$

$$\mathbf{v}_a^{y_2 w/a} = \begin{bmatrix} \dot{x}_a - \cos\theta \dot{\theta} \left(\ell_i + \boldsymbol{\Psi}_\ell \mathbf{q}^e \right) - \sin\theta \left(\dot{\ell}_i + \boldsymbol{\Psi}_\ell \dot{\mathbf{q}}^e \right) \\ -\sin\theta \dot{\theta} \left(\ell_i + \boldsymbol{\Psi}_\ell \mathbf{q}^e \right) + \cos\theta \left(\dot{\ell}_i + \boldsymbol{\Psi}_\ell \dot{\mathbf{q}}^e \right) \\ 0 \end{bmatrix}, \tag{2.5}$$

where

$$\boldsymbol{\Psi}_\ell = \boldsymbol{\Psi}\left(L, \ell_i\right) = \begin{bmatrix} \sin\left(\frac{\pi}{2}\right) & \sin\left(2\frac{\pi}{2}\right) & \sin\left(3\frac{\pi}{2}\right) & \dots \end{bmatrix} = \begin{bmatrix} 1 & 0 & -1 & 0 & \cdots \end{bmatrix}$$

with the chosen basis functions (2.1).

The kinetic and potential energies of the payload relative to point w with respect to $\mathcal{F}_a$ are

$$\begin{aligned} T_{y_2w/a} &= \tfrac{1}{2} m_2 \mathbf{v}_a^{y_2w/a\mathsf{T}} \mathbf{v}_a^{y_2w/a} = \tfrac{1}{2} \dot{\mathbf{q}}^\mathsf{T} \mathbf{M}_{y_2w} \dot{\mathbf{q}}, \\ V_{y_2w} &= m_2 \mathbf{g}_a^\mathsf{T} \mathbf{r}_a^{y_2w} = -m_2 g \cos\theta \left(\ell_i + \boldsymbol{\Psi}_\ell \mathbf{q}^e\right), \end{aligned}$$

where

$$\mathbf{M}_{y_2w} = m_2 \begin{bmatrix} 1 & r\sin\theta & -\cos\theta\left(\ell_i + \boldsymbol{\Psi}_\ell \mathbf{q}^e\right) & -\sin\theta \boldsymbol{\Psi}_\ell \\ * & r^2 & 0 & -r\boldsymbol{\Psi}_\ell \\ * & * & \left(\ell_i + \boldsymbol{\Psi}_\ell \mathbf{q}^e\right)^2 & \mathbf{0} \\ * & * & * & \boldsymbol{\Psi}_\ell^\mathsf{T} \boldsymbol{\Psi}_\ell \end{bmatrix}.$$

2.4.4 Kinetic and Potential Energies of the Complete System

Combining the kinetic and potential energies of the individual system components calculated in the previous sections, the total kinetic and potential energies of the crane are

$$\begin{aligned} T_{\text{total}} &= \tfrac{1}{2} \dot{\mathbf{q}}^\mathsf{T} \mathbf{M} \dot{\mathbf{q}}, \\ V_{\text{total}} &= \tfrac{1}{2} \mathbf{q}^\mathsf{T} \mathbf{K} \mathbf{q} + V_g, \end{aligned}$$

where $\mathbf{M} = \mathbf{M}_{cw} + \mathbf{M}_{y_1w} + \mathbf{M}_{y_2w}$, and $V_g = V_{cg} + V_{y_2w}$.

2.5 Equations of Motion (EOM)

Based on the kinetic and potential energies derived in Section 2.4, the equations of motion (EOM) of the system are derived using Lagrange's equation

$$\frac{\mathrm{d}}{\mathrm{d}t}\left(\frac{\partial L}{\partial \dot{\mathbf{q}}}\right)^{\mathsf{T}} - \left(\frac{\partial L}{\partial \mathbf{q}}\right)^{\mathsf{T}} = f\left(\mathbf{q}(t), t\right),$$

where $L = T_{\text{total}} - V_{\text{total}}$, and $f(\mathbf{q}(t), t)$ contains the generalized forces and moments. The equations of motion of the crane are derived to be

$$\mathbf{M}\ddot{\mathbf{q}} + \mathbf{D}\dot{\mathbf{q}} + \mathbf{K}\mathbf{q} = \mathbf{f} + \mathbf{f}_{non}\left(\mathbf{q}, \dot{\mathbf{q}}\right), \tag{2.6}$$

where $\mathbf{f}^{\mathsf{T}} = \begin{bmatrix}\hat{\mathbf{f}}^{\mathsf{T}} & \mathbf{0}\end{bmatrix}$, $\hat{\mathbf{f}}^{\mathsf{T}} = \begin{bmatrix}f & \tau\end{bmatrix}$ are the actuator inputs, $\mathbf{D} = \mathrm{diag}\{0, 0, c_\theta, \mathbf{D}_{ee}\}$, $c_\theta \geq 0$, $\mathbf{D}_{ee} = \mathbf{D}_{ee}^{\mathsf{T}} \geq 0$ represent natural damping in the payload sway and cable vibration, $\mathbf{f}_{non} = \mathbf{C}_{non}\left(\mathbf{q}, \dot{\mathbf{q}}\right)\dot{\mathbf{q}} + \mathbf{G}_{non}\left(\mathbf{q}\right)$ are the non-linear terms including

$$\mathbf{C}_{non}\left(\mathbf{q}, \dot{\mathbf{q}}\right)\dot{\mathbf{q}} = -\dot{\mathbf{M}}\dot{\mathbf{q}} + \left(\frac{\partial}{\partial \mathbf{q}}\left(\tfrac{1}{2}\dot{\mathbf{q}}^{\mathsf{T}}\mathbf{M}\dot{\mathbf{q}}\right)\right)^{\mathsf{T}},$$

$$\mathbf{G}_{non}\left(\mathbf{q}\right) = -\left(\frac{\tilde{\partial}}{\tilde{\partial}\mathbf{q}}\left(\tfrac{1}{2}\mathbf{q}^{\mathsf{T}}\mathbf{K}\mathbf{q}\right)\right)^{\mathsf{T}} - \left(\frac{\partial V_g}{\partial \mathbf{q}}\right)^{\mathsf{T}}.$$

The symbol $\frac{\tilde{\partial}}{\tilde{\partial}\mathbf{q}}$ represents that the partial derivative taken while keeping the quadratic terms of the generalized coordinates $\mathbf{q}$ constant, i.e.,

$$\left(\frac{\tilde{\partial}}{\tilde{\partial}\mathbf{q}}\left(\tfrac{1}{2}\mathbf{q}^{\mathsf{T}}\mathbf{K}\mathbf{q}\right)\right)^{\mathsf{T}} = \left(\tfrac{1}{2}\mathbf{q}^{\mathsf{T}}\left(\frac{\partial \mathbf{K}}{\partial \mathbf{q}}\right)\mathbf{q}\right)^{\mathsf{T}} = \begin{bmatrix} 0 \\ \frac{1}{2}\frac{EAr}{\ell_i^2}\mathbf{q}^{e\mathsf{T}}\mathbf{\Lambda}_{33}\mathbf{q}^{e} \\ \mathbf{0} \end{bmatrix}.$$

The full details of the entries of $\mathbf{M}$ and $\mathbf{f}_{non}$ matrices can be find in Appendix A.

It is worth noting that the nonlinear terms satisfy the following properties [36]

$$\dot{V}_g - \dot{\mathbf{q}}^{\mathsf{T}} \left(\frac{\partial V_g}{\partial \mathbf{q}} \right)^{\mathsf{T}} = 0,$$
$$\dot{\mathbf{q}}^{\mathsf{T}} \left(\mathbf{C}_{non} + \tfrac{1}{2}\dot{\mathbf{M}} \right) \dot{\mathbf{q}} = 0,$$
$$\tfrac{1}{2}\mathbf{q}^{\mathsf{T}}\dot{\mathbf{K}}\mathbf{q} = \dot{\mathbf{q}}^{\mathsf{T}} \left(\frac{\tilde{\partial}}{\tilde{\partial}\mathbf{q}} \left(\tfrac{1}{2}\mathbf{q}^{\mathsf{T}}\mathbf{K}\mathbf{q} \right) \right)^{\mathsf{T}}.$$

2.6 Conclusion

The dynamic model presented in this chapter provides a reasonably accurate model of the dominant features of a 2 DOF tower crane with a flexible hoist cable. The flexible hoist cable modeling using a Rayleigh-Ritz method inspired by [36] is a novel contribution in tower crane modeling. The tower crane is an underactuated system, whose inputs $\hat{\mathbf{f}} = \begin{bmatrix} f & \tau \end{bmatrix}^{\mathsf{T}}$ do not directly and individually control the state variables $\mathbf{q}^{\mathsf{T}} = \begin{bmatrix} x_a & \phi & \theta & \mathbf{q}^{e\mathsf{T}} \end{bmatrix}$. The sway angle θ and the cable vibration coordinates $\mathbf{q}^e$ are driven by the kinematics relationship between payload position, payload velocity, trolley position, trolley velovity associated with the inputs $\hat{\mathbf{f}}$ and Earth's gravity acting on the payload. The following chapters focus on two different control approaches that address this noncolocation issue. The dynamic model derived in this chapter is used to perform the nonlinear closed-loop simulations found in subsequent chapters.

Chapter 3

Passivity-Based μ-Tip Control

3.1 Introduction

The Passivity Theorem [37] guarantees closed-loop input-output stability of a negative feedback interconnection involving a passive system and an input strictly passive controller. Based on the kinematics of the crane system derived in Chapter 2, a μ-tip modification and passivity-based approach is presented to perform position and velocity tracking of the tower crane's payload located at the tip of the flexible cable in this chapter. It is assumed that the crane's payload is much heavier than the crane itself, which is known as a massive payload assumption [41]. This allows for an approximate decoupling of the crane's rigid and flexible equations of motion in Section 3.2. Introducing the μ-tip method [38] to modify the payload velocity $\dot{\boldsymbol{\rho}}$ into $\dot{\boldsymbol{\rho}}_\mu$ preserves a passivity input-output stability mapping from the modified control input $(\hat{\boldsymbol{\tau}}_c - \hat{\boldsymbol{\tau}}_r)$ to filtered error $\mathbf{s}_\mu = \dot{\tilde{\boldsymbol{\rho}}}_\mu + \boldsymbol{\Lambda}\tilde{\boldsymbol{\rho}}_\mu$ will be discussed in Section 3.3. Section 3.3.3 demonstrates the proposed control law and the stability of the closed-loop system, and Section 3.4 presents a the numerical simulation results.

3.2 Massive Payload Approximation

Using (2.4) and (2.5), the position and velocity of the payload resolved in the $\underrightarrow{a}^1$ and $\underrightarrow{a}^2$ directions of $\mathcal{F}_a$ are

$$\boldsymbol{\rho} = \mathbf{J}_{\text{rigid}}\boldsymbol{\eta} + \begin{bmatrix} -\sin\theta\left(L + \boldsymbol{\Psi}_\ell \mathbf{q}^e\right) \\ \cos\theta\left(L + \boldsymbol{\Psi}_\ell \mathbf{q}^e\right) \end{bmatrix}, \tag{3.1}$$

$$\dot{\boldsymbol{\rho}} = \mathbf{J}_{\text{rigid}}\dot{\boldsymbol{\eta}} + \mathbf{J}_{\text{flex}}\big|_{\mu=1}\dot{\bar{\mathbf{q}}}_e, \tag{3.2}$$

where $\boldsymbol{\eta}^\mathsf{T} = \begin{bmatrix} x_a & \phi \end{bmatrix}$ contains the rigid coordinates, $\bar{\mathbf{q}}_e^\mathsf{T} = \begin{bmatrix} \theta & \mathbf{q}^{e\mathsf{T}} \end{bmatrix}$ contains the flexible coordinates, and

$$\mathbf{J}_{\text{rigid}}\left(\bar{\mathbf{q}}_e\right) = \begin{bmatrix} 1 & r\sin\theta \\ 0 & -r\cos\theta \end{bmatrix},$$

$$\mathbf{J}_{\text{flex}}\left(\mu, \boldsymbol{\eta}, \bar{\mathbf{q}}_e\right) = \begin{bmatrix} \cos\theta\left(\frac{r\phi}{\mu} - L - \boldsymbol{\Psi}_\ell \mathbf{q}^e\right) & -\sin\theta\boldsymbol{\Psi}_\ell \\ \sin\theta\left(\frac{r\phi}{\mu} - L - \boldsymbol{\Psi}_\ell \mathbf{q}^e\right) & \cos\theta\boldsymbol{\Psi}_\ell \end{bmatrix},$$

are the state-dependent rigid and flexible Jacobians, respectively. The rigid Jacobian, $\mathbf{J}_{\text{rigid}}$, is a full-rank matrix provided $-\frac{\pi}{2} < \theta < \frac{\pi}{2}$.

The true payload velocity is presented when the scaling parameter $\mu = 1$ in the flexible Jacobian; further details on this scaling parameter are discussed in Section 3.3.1. Note that although the sway angle θ is assumed relevantly small in Section 3.3.2, a novel contribution of this work is to consider θ as a flexible coordinate.

It is assumed that the crane's payload is much heavier than the crane itself, which is known as a massive payload assumption [41]. It is also assumed that θ and $\dot{\theta}$ are small. The combination of these two assumptions allows for an approximate decoupling of the crane's rigid and flexible equations of motion, which is taken advantage of in the passivity-based control formulation of Section 3.3.

3.2.1 Approximate Rigid EOMs

Due to the massive payload, the kinetic energy of the system is dominated by that of the payload when the payload is moving [38, 41]. Mathematically, this means that when the payload is in motion, $T_{\text{total}} \approx T_{y_2w/a}$, $\dot{\tilde{\mathbf{q}}}_e \approx \mathbf{0}$ and $\ddot{\tilde{\mathbf{q}}}_e \approx \mathbf{0}$. With these approximations, the system's equations of motion become

$$\mathbf{M}_{rr}\ddot{\boldsymbol{\eta}} = \hat{\mathbf{f}} + \mathbf{C}_r\left(\mathbf{q}, \dot{\boldsymbol{\eta}}\right)\dot{\boldsymbol{\eta}} + \mathbf{G}_r\left(\mathbf{q}\right), \tag{3.3}$$

where $\mathbf{M}_{rr} = \begin{bmatrix}\mathbf{1}_{2\times 2} & \mathbf{0}\end{bmatrix}\mathbf{M}\begin{bmatrix}\mathbf{1}_{2\times 2} \\ \mathbf{0}\end{bmatrix}$, $\mathbf{C}_r\left(\mathbf{q}, \dot{\boldsymbol{\eta}}\right) = \begin{bmatrix}\mathbf{1}_{2\times 2} & \mathbf{0}\end{bmatrix}\mathbf{C}_{non}\big|_{\dot{\tilde{\mathbf{q}}}_e=0}\begin{bmatrix}\mathbf{1}_{2\times 2} \\ \mathbf{0}\end{bmatrix}$, and

$$\mathbf{G}_r\left(\mathbf{q}\right) = \begin{bmatrix} 0 \\ -gr\cos\theta\left(m_2 + \rho A\left(\ell_i + \boldsymbol{\Lambda}_2\mathbf{q}^e\right)\right) - \mathbf{q}^{e\mathsf{T}}\frac{r\mathbf{K}_{ee}}{2\ell_i}\mathbf{q}^e \end{bmatrix}.$$

It is worth noting that $2\mathbf{C}_r + \dot{\mathbf{M}}_{rr}$ is skew-symmetric. When $\dot{\tilde{\mathbf{q}}}_e = \mathbf{0}$, it is known that $\dot{\boldsymbol{\rho}} = \mathbf{J}_{\text{rigid}}\dot{\boldsymbol{\eta}}$. Substituting $\dot{\boldsymbol{\eta}} = \mathbf{J}_{\text{rigid}}^{-1}\dot{\boldsymbol{\rho}}$ and $\ddot{\boldsymbol{\eta}} = \dot{\mathbf{J}}_{\text{rigid}}^{-1}\dot{\boldsymbol{\rho}} + \mathbf{J}_{\text{rigid}}^{-1}\ddot{\boldsymbol{\rho}}$ into (3.3) and premultiplying by $\mathbf{J}_{\text{rigid}}^{-\mathsf{T}}$ gives the approximate rigid equations of motion

$$\mathbf{M}_{\rho\rho}\left(\boldsymbol{\rho}\right)\ddot{\boldsymbol{\rho}} - \mathbf{C}_\rho\left(\boldsymbol{\rho}, \dot{\boldsymbol{\rho}}\right)\dot{\boldsymbol{\rho}} - \mathbf{G}_\rho\left(\boldsymbol{\rho}\right) = \hat{\boldsymbol{\tau}}_c, \tag{3.4}$$

where

$$\begin{aligned}
&\mathbf{M}_{\rho\rho}\left(\boldsymbol{\rho}\right) = \mathbf{J}_{\text{rigid}}^{-\mathsf{T}}\mathbf{M}_{rr}\mathbf{J}_{\text{rigid}}^{-1}, \\
&\mathbf{C}_\rho\left(\boldsymbol{\rho}, \dot{\boldsymbol{\rho}}\right) = \mathbf{J}_{\text{rigid}}^{-\mathsf{T}}\mathbf{C}_r\mathbf{J}_{\text{rigid}}^{-1} - \mathbf{J}_{\text{rigid}}^{-\mathsf{T}}\mathbf{M}_{rr}\dot{\mathbf{J}}_{\text{rigid}}^{-1}, \\
&\mathbf{G}_\rho\left(\boldsymbol{\rho}\right) = \mathbf{J}_{\text{rigid}}^{-\mathsf{T}}\mathbf{G}_r, \\
&\hat{\boldsymbol{\tau}}_c = \mathbf{J}_{\text{rigid}}^{-\mathsf{T}}\hat{\mathbf{f}},
\end{aligned}$$

and $2\mathbf{C}_\rho + \dot{\mathbf{M}}_{\rho\rho}$ is skew-symmetric.

3.2.2 Approximate Elastic EOMs

For the remainder of this chapter it will be assumed that $\mu \approx 1$, which leads to the approximation $\mathbf{J}_{\text{flex}} \approx \mathbf{J}_{\text{flex}}|_{\mu=1}$. This assumption is valid provided that the payload is massive [38]. When the payload is at rest, $\dot{\boldsymbol{\rho}} = \ddot{\boldsymbol{\rho}} = \mathbf{0}$, which gives $\dot{\boldsymbol{\eta}} = -\mathbf{J}_{\text{rigid}}^{-1}\mathbf{J}_{\text{flex}}\dot{\bar{\mathbf{q}}}_e$, $\ddot{\boldsymbol{\eta}} = -\mathbf{J}_{\text{rigid}}^{-1}\left(\dot{\mathbf{J}}_{\text{rigid}}\dot{\boldsymbol{\eta}} + \mathbf{J}_{\text{flex}}\ddot{\bar{\mathbf{q}}}_e + \dot{\mathbf{J}}_{\text{flex}}\dot{\bar{\mathbf{q}}}_e\right)$. Defining $\mathbf{B}_e = \begin{bmatrix} -\mathbf{J}_{\text{rigid}}^{-1}\mathbf{J}_{\text{flex}} \\ \mathbf{1} \end{bmatrix}$ yields the relationships $\dot{\mathbf{q}} = \mathbf{B}_e\dot{\bar{\mathbf{q}}}_e$ and $\ddot{\mathbf{q}} = \mathbf{B}_e\ddot{\bar{\mathbf{q}}}_e + \dot{\mathbf{B}}_e\dot{\bar{\mathbf{q}}}_e$. Substituting these expressions into (2.6) and premultiplying by $\mathbf{B}_e^{\mathsf{T}}$ gives the elastic equations of motion

$$\begin{aligned} &\hat{\mathbf{M}}_{ee}\left(\bar{\mathbf{q}}_e\right)\ddot{\bar{\mathbf{q}}}_e + \hat{\mathbf{D}}_{ee}\dot{\bar{\mathbf{q}}}_e + \hat{\mathbf{K}}_{ee}\left(\bar{\mathbf{q}}_e\right)\bar{\mathbf{q}}_e \\ &\quad - \mathbf{C}_e\left(\bar{\mathbf{q}}_e, \dot{\bar{\mathbf{q}}}_e\right)\dot{\bar{\mathbf{q}}}_e - \mathbf{G}_e\left(\bar{\mathbf{q}}_e\right) = -\mathbf{J}_{\text{flex}}^{\mathsf{T}}\hat{\boldsymbol{\tau}}_c, \end{aligned} \tag{3.5}$$

where $\hat{\mathbf{M}}_{ee}\left(\bar{\mathbf{q}}_e\right) = \mathbf{B}_e^{\mathsf{T}}\mathbf{M}\mathbf{B}_e$, $\hat{\mathbf{D}}_{ee} = \mathbf{B}_e^{\mathsf{T}}\mathbf{D}\mathbf{B}_e = \text{diag}\{c_\theta, \mathbf{D}_{ee}\}$, $\hat{\mathbf{K}}_{ee}\left(\bar{\mathbf{q}}_e\right) = \text{diag}\{0, \mathbf{K}_{ee}\}$, $\mathbf{C}_e\left(\bar{\mathbf{q}}_e, \dot{\bar{\mathbf{q}}}_e\right) = \mathbf{B}_e^{\mathsf{T}}\mathbf{C}_{non}\mathbf{B}_e - \mathbf{B}_e^{\mathsf{T}}\mathbf{M}\dot{\mathbf{B}}_e$, $\mathbf{G}_e\left(\bar{\mathbf{q}}_e\right) = \mathbf{B}_e^{\mathsf{T}}\mathbf{G}_{non}$, and $\mathbf{C}_e + \frac{1}{2}\dot{\hat{\mathbf{M}}}_{ee}$ is skew-symmetric.

3.3 μ-Tip Rate and Passivity-Based Control Formulation

Section 3.3.1 defines the μ-tip modification of the velocity and position, Section 3.3.2 demonstrates that the μ-tip rate leads to a passive input-output mapping, and Section 3.3.3 proves closed-loop input-output stability and asymptotic stability of the payload velocity tracking error.

3.3.1 μ-Tip Rate

The measured payload velocity is located at the opposite end of the cable from where the actuated winch and trolley are located, which results in a non-colocated input-output mapping that is not passive. The μ-tip rate, which was introduced

in [38] and has since been applied to a number of different applications [36, 39–41], is a modified version of the payload velocity that along with the system input $\hat{\tau}_c$ can yield a passive input-output mapping. The μ-tip rate scales the influence of flexible coordinate rates ($\dot{\bar{\mathbf{q}}}_e$ in the case of the tower crane in this thesis) when calculating the payload velocity, and is defined as

$$\begin{aligned}\dot{\boldsymbol{\rho}}_\mu &= \mathbf{J}_{\text{rigid}}\dot{\boldsymbol{\eta}} + \mu\mathbf{J}_{\text{flex}}\dot{\bar{\mathbf{q}}}_e \\ &= \dot{\boldsymbol{\rho}} - (1-\mu)\,\mathbf{J}_{\text{flex}}\dot{\bar{\mathbf{q}}}_e,\end{aligned} \tag{3.6}$$

where $0 \leq \mu < 1$ is the scaling parameter. When $\mu = 0$, $\dot{\boldsymbol{\rho}}_\mu$ is the velocity of the payload as if $\dot{\theta} = 0$ rad/s and $\dot{\mathbf{q}}^e = \mathbf{0}$. Although $\mu = 1$ is not considered in practice, this results in the μ-tip rate matching the true payload velocity. The μ-tip position is defined through the integral of the μ-tip rate as

$$\boldsymbol{\rho}_\mu(t) = \int_0^t \dot{\boldsymbol{\rho}}_\mu(\tau)\mathrm{d}\tau. \tag{3.7}$$

3.3.2 Filtered Error Passivity Analysis

For the purpose of tracking the position and velocity of the crane's payload, the filtered error is defined as $\mathbf{s}_\mu = \dot{\tilde{\boldsymbol{\rho}}}_\mu + \boldsymbol{\Lambda}\tilde{\boldsymbol{\rho}}_\mu$, where $\boldsymbol{\Lambda} = \boldsymbol{\Lambda}^\mathsf{T} > 0$ [42]. The μ-tip position and μ-tip rate tracking errors are $\tilde{\boldsymbol{\rho}}_\mu = \boldsymbol{\rho}_\mu - \boldsymbol{\rho}_{\mu,d}$ and $\dot{\tilde{\boldsymbol{\rho}}}_\mu = \dot{\boldsymbol{\rho}}_\mu - \dot{\boldsymbol{\rho}}_{\mu,d}$, where $\dot{\boldsymbol{\rho}}_{\mu,d}$ and $\boldsymbol{\rho}_{\mu,d}$ are (3.6) and (3.7) evaluated at the prescribed desired position $\boldsymbol{\rho}_d$ and desired rate $\dot{\boldsymbol{\rho}}_d$, with the desired rigid coordinates $\boldsymbol{\eta}_d^\mathsf{T} = \begin{bmatrix} x_{a,d} & \phi_d \end{bmatrix}$ and desired elastic coordinates $\bar{\mathbf{q}}_{e,d}^\mathsf{T} = \begin{bmatrix} \theta_d & \mathbf{q}_d^{e\mathsf{T}} \end{bmatrix}$. The definition of $\dot{\boldsymbol{\rho}}_{\mu,d}$ involves the flexible Jacobian evaluated at the desired rigid and elastic coordinates, where it is assumed that $\mathbf{J}_{\text{flex}}(\mu, \boldsymbol{\eta}_d, \bar{\mathbf{q}}_{e,d}) \approx \mathbf{J}_{\text{flex}}(\mu, \boldsymbol{\eta}, \bar{\mathbf{q}}_e)$. This assumption leads to the expression

$$\dot{\tilde{\boldsymbol{\rho}}}_\mu = \dot{\tilde{\boldsymbol{\rho}}} - (1-\mu)\mathbf{J}_{\text{flex}}\dot{\tilde{\mathbf{q}}}_e,$$

where $\dot{\tilde{\boldsymbol{\rho}}} = \dot{\boldsymbol{\rho}} - \dot{\boldsymbol{\rho}}_d$ and $\dot{\tilde{\mathbf{q}}}_e = \dot{\bar{\mathbf{q}}}_e - \dot{\bar{\mathbf{q}}}_{e,d}$ [38]. The filtered error is a linear combination of the μ-tip rate and μ-tip position errors, and $\mathbf{s}_\mu = 0$ can be thought of as a sliding

surface within the context of sliding-mode control [48].

The desired rigid and flexible equations of motion of the crane are given by

$$\mathbf{M}_{\rho\rho}(\boldsymbol{\rho})\,\ddot{\boldsymbol{\rho}}_r - \mathbf{C}_{\rho}(\boldsymbol{\rho},\dot{\boldsymbol{\rho}})\,\dot{\boldsymbol{\rho}}_r - \mathbf{G}_{\rho}(\boldsymbol{\rho}) = \hat{\boldsymbol{\tau}}_r, \tag{3.8}$$

$$\begin{aligned}\mathbf{M}_{ee}(\bar{\mathbf{q}}_e)\,\ddot{\bar{\mathbf{q}}}_{e,d} + \hat{\mathbf{D}}_{ee}\dot{\bar{\mathbf{q}}}_{e,d} + \hat{\mathbf{K}}_{ee}(\bar{\mathbf{q}}_e)\,\bar{\mathbf{q}}_{e,d} \\ - \mathbf{C}_e\left(\bar{\mathbf{q}}_e,\dot{\bar{\mathbf{q}}}_e\right)\dot{\bar{\mathbf{q}}}_{e,d} - \mathbf{G}_{e,d} = -\mathbf{J}_{\text{flex},d}^{\mathsf{T}}\hat{\boldsymbol{\tau}}_r,\end{aligned} \tag{3.9}$$

where $\hat{\boldsymbol{\tau}}_r^{\mathsf{T}} = \begin{bmatrix} f_r & \tau_r \end{bmatrix}$ is the feedforward input associated with the desired dynamics, $\dot{\boldsymbol{\rho}}_r = \dot{\boldsymbol{\rho}}_d - \boldsymbol{\Lambda}\tilde{\boldsymbol{\rho}}_{\mu}$ is the virtual reference trajectory rate, $\mathbf{G}_{e,d}$ is defined to satisfy

$$\dot{\tilde{\mathbf{q}}}_e^{\mathsf{T}}\tilde{\mathbf{G}}_e + \tfrac{1}{2}\tilde{\mathbf{q}}_e^{\mathsf{T}}\dot{\hat{\mathbf{K}}}_{ee}\tilde{\mathbf{q}}_e = 0, \tag{3.10}$$

and $\tilde{\mathbf{G}}_e = \mathbf{G}_e - \mathbf{G}_{e,d}$. Subtracting (3.8) and (3.9) from (3.4) and (3.5) results in error dynamics given by

$$\mathbf{M}_{\rho\rho}(\boldsymbol{\rho})\,\ddot{\tilde{\boldsymbol{\rho}}}_r - \mathbf{C}_{\rho}(\boldsymbol{\rho},\dot{\boldsymbol{\rho}})\,\dot{\tilde{\boldsymbol{\rho}}}_r = \hat{\boldsymbol{\tau}}_c - \hat{\boldsymbol{\tau}}_r, \tag{3.11}$$

$$\begin{aligned}\mathbf{M}_{ee}(\bar{\mathbf{q}}_e)\,\ddot{\tilde{\mathbf{q}}}_e + \hat{\mathbf{D}}_{ee}\dot{\tilde{\mathbf{q}}}_e + \hat{\mathbf{K}}_{ee}(\bar{\mathbf{q}}_e)\,\tilde{\mathbf{q}}_e \\ - \mathbf{C}_e\left(\bar{\mathbf{q}}_e,\dot{\bar{\mathbf{q}}}_e\right)\dot{\tilde{\mathbf{q}}}_e - \tilde{\mathbf{G}}_e = -\mathbf{J}_{\text{flex}}^{\mathsf{T}}\left(\hat{\boldsymbol{\tau}}_c - \hat{\boldsymbol{\tau}}_r\right),\end{aligned} \tag{3.12}$$

where $\tilde{\mathbf{q}}_e = \bar{\mathbf{q}}_e - \bar{\mathbf{q}}_{e,d}$, $\dot{\tilde{\boldsymbol{\rho}}}_r = \dot{\boldsymbol{\rho}} - \dot{\boldsymbol{\rho}}_r = \dot{\tilde{\boldsymbol{\rho}}} + \boldsymbol{\Lambda}\tilde{\boldsymbol{\rho}}_{\mu}$.

Theorem 3. *Consider the system defined by the error dynamics in* (3.11) *and* (3.12)*. The input-output mapping* $(\hat{\boldsymbol{\tau}}_c - \hat{\boldsymbol{\tau}}_r) \mapsto \mathbf{s}_{\mu}$ *is passive.*

Proof. Consider the non-negative function

$$\nu = \tfrac{1}{2}\dot{\tilde{\boldsymbol{\rho}}}_r^{\mathsf{T}}\mathbf{M}_{\rho\rho}\dot{\tilde{\boldsymbol{\rho}}}_r + (1-\mu)\left(\tilde{T}_e + \tilde{V}_e\right), \tag{3.13}$$

where $\tilde{T}_e = \frac{1}{2}\dot{\tilde{\mathbf{q}}}_e^{\mathsf{T}}\hat{\mathbf{M}}_{ee}\dot{\tilde{\mathbf{q}}}_e$ and $\tilde{V}_e = \frac{1}{2}\tilde{\mathbf{q}}_e^{\mathsf{T}}\hat{\mathbf{K}}_{ee}\tilde{\mathbf{q}}_e$. Taking the time-derivative of ν and

substituting in the error dynamics of (3.11) and (3.12) yields

$$\begin{aligned}
\dot{\nu} &= \dot{\tilde{\boldsymbol{\rho}}}_r^{\mathsf{T}} \left(\mathbf{M}_{\rho\rho} \ddot{\tilde{\boldsymbol{\rho}}}_r + \tfrac{1}{2} \dot{\mathbf{M}}_{\rho\rho} \dot{\tilde{\boldsymbol{\rho}}}_r \right) + (1-\mu) \left(\tfrac{1}{2} \tilde{\mathbf{q}}_e^{\mathsf{T}} \dot{\hat{\mathbf{K}}}_{ee} \tilde{\mathbf{q}}_e + \dot{\tilde{\mathbf{q}}}_e^{\mathsf{T}} \left(\hat{\mathbf{M}}_{ee} \ddot{\tilde{\mathbf{q}}}_e + \tfrac{1}{2} \dot{\hat{\mathbf{M}}}_{ee} \dot{\tilde{\mathbf{q}}}_e + \hat{\mathbf{K}}_{ee} \tilde{\mathbf{q}}_e \right) \right) \\
&= \dot{\tilde{\boldsymbol{\rho}}}_r^{\mathsf{T}} \left(\hat{\boldsymbol{\tau}}_c - \hat{\boldsymbol{\tau}}_r \right) + \dot{\tilde{\boldsymbol{\rho}}}_r^{\mathsf{T}} \mathbf{C}_\rho \dot{\tilde{\boldsymbol{\rho}}}_r + \tfrac{1}{2} \dot{\tilde{\boldsymbol{\rho}}}_r^{\mathsf{T}} \dot{\mathbf{M}}_{\rho\rho} \dot{\tilde{\boldsymbol{\rho}}}_r + (1-\mu) \left(\tfrac{1}{2} \tilde{\mathbf{q}}_e^{\mathsf{T}} \dot{\hat{\mathbf{K}}}_{ee} \tilde{\mathbf{q}}_e \right) \\
&\quad + (1-\mu) \dot{\tilde{\mathbf{q}}}_e^{\mathsf{T}} \left(-\mathbf{J}_{\text{flex}}^{\mathsf{T}} \left(\hat{\boldsymbol{\tau}}_c - \hat{\boldsymbol{\tau}}_r \right) + \mathbf{C}_e \dot{\tilde{\mathbf{q}}}_e + \tilde{\mathbf{G}}_e + \tfrac{1}{2} \dot{\hat{\mathbf{M}}}_{ee} \dot{\tilde{\mathbf{q}}}_e - \hat{\mathbf{D}}_{ee} \dot{\tilde{\mathbf{q}}}_e \right) \\
&= \left(\dot{\tilde{\boldsymbol{\rho}}}_r - (1-\mu) \mathbf{J}_{\text{flex}} \dot{\tilde{\mathbf{q}}}_e \right)^{\mathsf{T}} \left(\hat{\boldsymbol{\tau}}_c - \hat{\boldsymbol{\tau}}_r \right) - (1-\mu) \dot{\tilde{\mathbf{q}}}_e^{\mathsf{T}} \hat{\mathbf{D}}_{ee} \dot{\tilde{\mathbf{q}}}_e + \dot{\tilde{\boldsymbol{\rho}}}_r^{\mathsf{T}} \left(\mathbf{C}_\rho + \tfrac{1}{2} \dot{\mathbf{M}}_{\rho\rho} \right) \dot{\tilde{\boldsymbol{\rho}}}_r \\
&\quad + (1-\mu) \dot{\tilde{\mathbf{q}}}_e^{\mathsf{T}} \left(\mathbf{C}_e + \tfrac{1}{2} \dot{\hat{\mathbf{M}}}_{ee} \right) \dot{\tilde{\mathbf{q}}}_e + (1-\mu) \left(\dot{\tilde{\mathbf{q}}}_e^{\mathsf{T}} \tilde{\mathbf{G}}_e + \tfrac{1}{2} \tilde{\mathbf{q}}_e^{\mathsf{T}} \dot{\hat{\mathbf{K}}}_{ee} \tilde{\mathbf{q}}_e \right). \qquad (3.14)
\end{aligned}$$

Note that the filtered error can be rewritten as

$$\begin{aligned}
\mathbf{s}_\mu &= \dot{\tilde{\boldsymbol{\rho}}}_\mu + \boldsymbol{\Lambda} \tilde{\boldsymbol{\rho}}_\mu \\
&= \dot{\tilde{\boldsymbol{\rho}}} - (1-\mu) \mathbf{J}_{\text{flex}} \dot{\tilde{\mathbf{q}}}_e + \dot{\tilde{\boldsymbol{\rho}}}_r - \dot{\tilde{\boldsymbol{\rho}}} \\
&= \dot{\tilde{\boldsymbol{\rho}}}_r - (1-\mu) \mathbf{J}_{\text{flex}} \dot{\tilde{\mathbf{q}}}_e. \qquad (3.15)
\end{aligned}$$

Using the fact that $\mathbf{C}_\rho + \frac{1}{2} \dot{\mathbf{M}}_{\rho\rho}$ and $\mathbf{C}_e + \frac{1}{2} \dot{\hat{\mathbf{M}}}_{ee}$ are skew-symmetric, (3.10), and (3.15) simplify (3.14) as

$$\dot{\nu} = \mathbf{s}_\mu^{\mathsf{T}} \left(\hat{\boldsymbol{\tau}}_c - \hat{\boldsymbol{\tau}}_r \right) - (1-\mu) \dot{\tilde{\mathbf{q}}}_e^{\mathsf{T}} \hat{\mathbf{D}}_{ee} \dot{\tilde{\mathbf{q}}}_e. \qquad (3.16)$$

Integrating (3.16) from $t = 0$ to $t = T$, where $T \geq 0$, leads to

$$\int_0^T \mathbf{s}_\mu^{\mathsf{T}} \left(\hat{\boldsymbol{\tau}}_c - \hat{\boldsymbol{\tau}}_r \right) \mathrm{d}t = -\nu(0) + \nu(T) + (1-\mu) \int_0^T \dot{\tilde{\mathbf{q}}}_e^{\mathsf{T}} \hat{\mathbf{D}}_{ee} \dot{\tilde{\mathbf{q}}}_e \mathrm{d}t.$$

Knowing that $\nu(T) \geq 0$, $\dot{\tilde{\mathbf{q}}}_e^{\mathsf{T}} \hat{\mathbf{D}}_{ee} \dot{\tilde{\mathbf{q}}}_e \geq 0$, and $\mu < 1$, gives

$$\int_0^T \mathbf{s}_\mu^{\mathsf{T}} \left(\hat{\boldsymbol{\tau}}_c - \hat{\boldsymbol{\tau}}_r \right) \mathrm{d}t \geq -\nu(0), \qquad (3.17)$$

which demonstrates that the input-output mapping $\left(\hat{\boldsymbol{\tau}}_c - \hat{\boldsymbol{\tau}}_r \right) \mapsto \mathbf{s}_\mu$ is passive. $\square$

3.3.3 Control Law and Closed-Loop Input-Output Stability

Employing the Passivity Theorem, closed-loop input-output stability of the crane with error dynamics in (3.11) and (3.12) is guaranteed by any input strictly passive (ISP) negative feedback controller [37]. One particular choice of an ISP negative feedback controller is $\hat{\boldsymbol{\tau}}_c - \hat{\boldsymbol{\tau}}_r = -\mathbf{K}_d \mathbf{s}_\mu$, where $\mathbf{K}_d = \mathbf{K}_d^\mathsf{T} > 0$, which results in a control input of

$$\hat{\boldsymbol{\tau}}_c = \mathbf{M}_{\rho\rho}(\boldsymbol{\rho})\,\ddot{\boldsymbol{\rho}}_r - \mathbf{C}_\rho(\boldsymbol{\rho}, \dot{\boldsymbol{\rho}})\,\dot{\boldsymbol{\rho}}_r - \mathbf{G}_\rho(\boldsymbol{\rho}) - \mathbf{K}_d \mathbf{s}_\mu. \tag{3.18}$$

Figure 3.1a shows a block diagram of the close-loop system with control law (3.18), and the way to calculate $\mathbf{s}_\mu$ from $\boldsymbol{\rho}_\mu$ and $\dot{\boldsymbol{\rho}}_\mu$. The plant $\mathcal{G}$ represents the practical crane model with equations of motion (2.6). An alternate block diagram is shown in Figure 3.1b, the plant $\tilde{\mathcal{G}}$ is defined by the error dynamics (3.11) and (3.12), and the passive input-output stability mapping $(\hat{\boldsymbol{\tau}}_c - \hat{\boldsymbol{\tau}}_r) \mapsto \mathbf{s}_\mu$ is marked by the dotted block.

Theorem 4. *Consider the tower crane described by the equations of motion in* (3.4) *and* (3.5). *The control law of* (3.18) *ensures that* $\tilde{\boldsymbol{\rho}}_\mu \to \mathbf{0}$, $\dot{\tilde{\boldsymbol{\rho}}} \to \mathbf{0}$, *and* $\dot{\tilde{\boldsymbol{\rho}}}_\mu \to \mathbf{0}$ *as* $t \to \infty$.

Proof. Consider the non-negative function in (3.13) and its time derivative in (3.16). Substituting $(\hat{\boldsymbol{\tau}}_c - \hat{\boldsymbol{\tau}}_r) = -\mathbf{K}_d \mathbf{s}_\mu$ into (3.16) leads to the conclusion that $\dot{\nu} \leq 0$ and $\nu(T) \leq \nu(0) < \infty$, which implies that $\{\dot{\tilde{\boldsymbol{\rho}}}_r, \dot{\tilde{\mathbf{q}}}_e, \mathbf{q}^e - \mathbf{q}_d^e\} \in \mathcal{L}_\infty$. Integrating (3.16) with $(\hat{\boldsymbol{\tau}}_c - \hat{\boldsymbol{\tau}}_c) = -\mathbf{K}_d \mathbf{s}_\mu$ from $t = 0$ to $t = T$ gives

$$\left\| \sqrt{\mathbf{K}_d}\, \mathbf{s}_\mu \right\|_{2T}^2 + (1 - \mu) \left\| \sqrt{\hat{\mathbf{D}}_{ee}}\, \dot{\tilde{\mathbf{q}}}_e \right\|_{2T}^2 = \nu(0) - \nu(T) < \infty,$$

which implies that $\{\mathbf{s}_\mu, \dot{\tilde{\mathbf{q}}}_e\} \in \mathcal{L}_2$. From the definition of $\mathbf{s}_\mu$ and knowing that $\{\dot{\tilde{\mathbf{q}}}_e, \dot{\tilde{\boldsymbol{\rho}}}_r\} \in \mathcal{L}_\infty$, it is concluded that $\mathbf{s}_\mu \in \mathcal{L}_\infty$. Rearranging the definition of

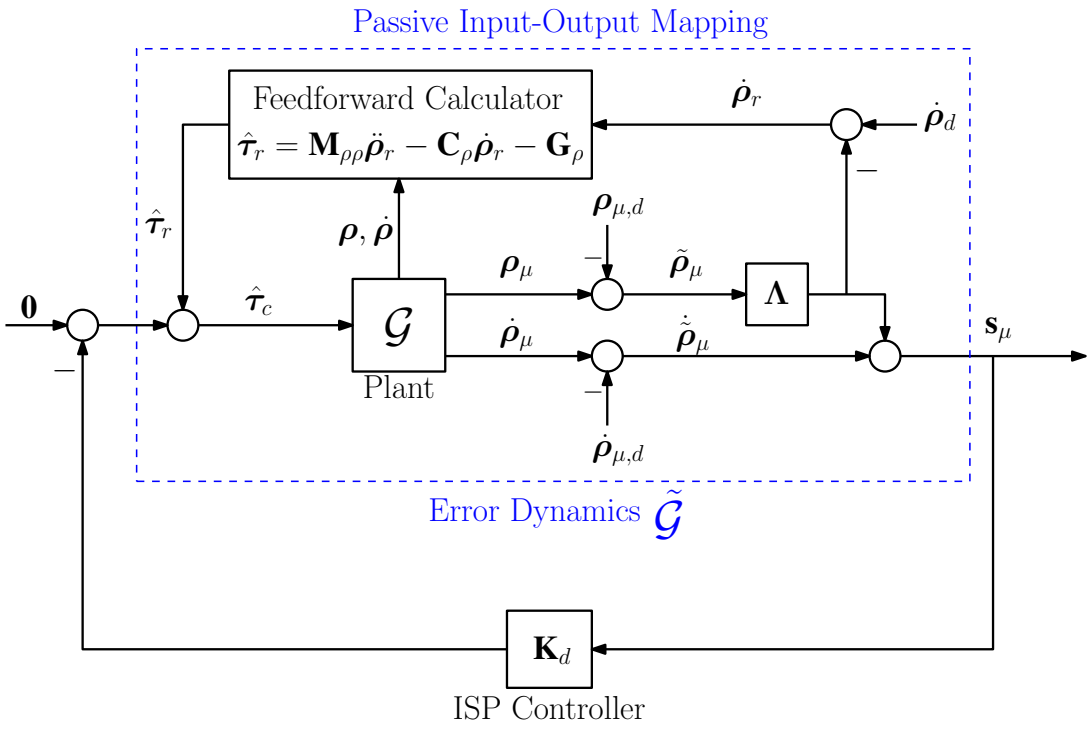

(a) Practical implementation of the feedback control system.

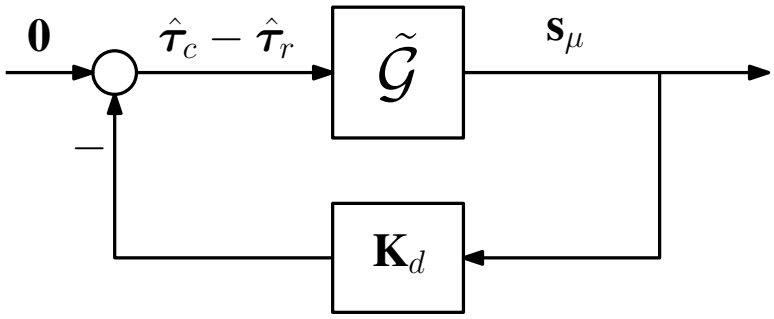

(b) Passive feedback control of the error dynamics.

Figure 3.1: Block diagrams with control law (3.18).

$\mathbf{s}_\mu$ results in $\dot{\tilde{\boldsymbol{\rho}}}_\mu = -\boldsymbol{\Lambda}\tilde{\boldsymbol{\rho}}_\mu + \mathbf{s}_\mu$, an asymptotically stable LTI system with an $\mathcal{L}_2$-bounded input, which guarantees that $\{\dot{\tilde{\boldsymbol{\rho}}}_\mu, \tilde{\boldsymbol{\rho}}_\mu\} \in \mathcal{L}_2 \cap \mathcal{L}_\infty$ employing Lemma 2 [37, p. 269]. Employing Barbalat's Lemma as in Lemma 1, $\tilde{\boldsymbol{\rho}}_\mu \to \mathbf{0}$ as $t \to \infty$ [37, p. 657].

Since $\mathbf{s}_\mu \in \mathcal{L}_2 \cap \mathcal{L}_\infty$ it is known that $\hat{\boldsymbol{\tau}}_c - \hat{\boldsymbol{\tau}}_r \in \mathcal{L}_2 \cap \mathcal{L}_\infty$. Knowing that $\{\tilde{\boldsymbol{\rho}}_\mu, \mathbf{q}^e - \mathbf{q}^e_d, \dot{\tilde{\mathbf{q}}}_e, \dot{\tilde{\boldsymbol{\rho}}}_r, \hat{\boldsymbol{\tau}}_c - \hat{\boldsymbol{\tau}}_r\} \in \mathcal{L}_\infty$ and $\{\dot{\boldsymbol{\rho}}_d, \boldsymbol{\rho}_{\mu,d}, \mathbf{q}^e_d, \dot{\mathbf{q}}^e_d\} \in \mathcal{L}_\infty$ by design, it can be concluded that $\{\boldsymbol{\rho}_\mu, \mathbf{q}^e, \dot{\mathbf{q}}^e, \ddot{\tilde{\mathbf{q}}}_e, \boldsymbol{\eta}, \boldsymbol{\rho}, \dot{\boldsymbol{\rho}}, \dot{\boldsymbol{\rho}}_r\} \in \mathcal{L}_\infty$. Since $\dot{\tilde{\mathbf{q}}}_e \in \mathcal{L}_2 \cap \mathcal{L}_\infty$ and $\ddot{\tilde{\mathbf{q}}}_e \in \mathcal{L}_\infty$, $\dot{\tilde{\mathbf{q}}}_e \to \mathbf{0}$ as $t \to \infty$ via Barbalat's Lemma. Taking the derivative of $\mathbf{s}_\mu$ gives $\dot{\mathbf{s}}_\mu = \dddot{\tilde{\boldsymbol{\rho}}}_r - (1-\mu)(\mathbf{J}_{\text{flex}}\dddot{\tilde{\mathbf{q}}}_e + \dot{\mathbf{J}}_{\text{flex}}\ddot{\tilde{\mathbf{q}}}_e)$, and leads to the conclusion that $\dot{\mathbf{s}}_\mu \in \mathcal{L}_\infty$ since $\{\ddot{\tilde{\boldsymbol{\rho}}}_r, \dddot{\tilde{\mathbf{q}}}_e, \ddot{\tilde{\mathbf{q}}}_e\} \in \mathcal{L}_\infty$ and the entries of $\mathbf{J}_{\text{flex}}$ and $\dot{\mathbf{J}}_{\text{flex}}$ are bounded. Knowing that $\mathbf{s}_\mu \in \mathcal{L}_2 \cap \mathcal{L}_\infty$ and $\dot{\mathbf{s}}_\mu \in \mathcal{L}_\infty$, $\mathbf{s}_\mu \to \mathbf{0}$ as $t \to \infty$ via Barbalat's Lemma, and hence $\hat{\boldsymbol{\tau}}_c - \hat{\boldsymbol{\tau}}_r \to \mathbf{0}$ as $t \to \infty$. From the definition of $\mathbf{s}_\mu$, $\dot{\tilde{\boldsymbol{\rho}}}_\mu \to \mathbf{0}$ as $t \to \infty$ since $\mathbf{s}_\mu \to \mathbf{0}$ and $\tilde{\boldsymbol{\rho}}_\mu \to \mathbf{0}$ as $t \to \infty$. From the definition of $\dot{\tilde{\boldsymbol{\rho}}}_\mu$ and (3.6), it is concluded that the payload velocity tracking error $\dot{\tilde{\boldsymbol{\rho}}} \to \mathbf{0}$ as $t \to \infty$ since $\tilde{\boldsymbol{\rho}}_\mu \to \mathbf{0}$ and $\dot{\tilde{\mathbf{q}}}_e \to \mathbf{0}$ as $t \to \infty$, and $\dot{\mathbf{q}}^e_d \to \mathbf{0}$ as $t \to \infty$ by assumption. □

Notice that the velocity tracking error of the payload asymptotically converges to zero, but the asymptotic behavior of the position tracking error is not proven. Theorem 4 does prove that the μ-tip tracking error asymptotically converges to zero, which motivates the desire to choose a value of μ close to one.

3.4 Numerical Example

The control law in (3.18) is implemented in a dynamic simulation of the two-dimensional tower crane using the equations of motion in (2.6). In simulation, the first two natural frequencies of axial vibration in the hoist cable are modeled using the basis functions $\boldsymbol{\Psi}(x, \ell_i) = \begin{bmatrix}\sin\bar{x} & \sin 2\bar{x}\end{bmatrix}$. Numerical values of $m_1 = 5$ kg, $m_2 = 500$ kg, and $m_w = 20$ kg are chosen, which results in a payload that is twenty times heavier than the trolley, thus satisfying the massive payload assumption [40]. The winch radius is given by $r = 0.1$ m. The numerical properties of the hoist cable are given by $E = 20$ GPa, $\rho_c = 1000$ kg/m^3, $L = 5$ m, and $r_c =$

0.002 m. The mass of the cable with nominal length $L = 5$ m is $m_c = \pi\rho_c r_c^2 L = 0.0628$ kg. The system's natural damping is chosen as $c_\theta = 10^{-12}$ N·s/m and $\mathbf{D}_{ee} = \begin{bmatrix} 12.4842 & 11.5019 \\ 0.5751 & 1.2484 \end{bmatrix}$, which corresponds to a damping ratio of less than 5 % for the hoist cable's axial modes of vibration and negligible damping of the hoist cable sway. The control parameters are given by $\mu = 0.95$, $\mathbf{\Lambda} = \text{diag}\{1, 1\}$ s^{-1}, and $\mathbf{K}_d = \text{diag}\{10^4, 10^4\}$ N/m·s. A suitable value of μ is found by examining the Bode plot of the linearized system, as discussed in [41]. Specifically, the largest value of μ for which the linearized system remains positive real is identified, and a value of μ slightly smaller than this is used to ensure a robustness margin.

Table 3.1: Parameters for desired payload trajectory.

Time	$\boldsymbol{\rho}_i^\mathsf{T}$	$\boldsymbol{\rho}_f^\mathsf{T}$
$0 \le t < 3$	$\begin{bmatrix} 0 & 5 \end{bmatrix}$	$\begin{bmatrix} 0 & 5 \end{bmatrix}$
$3 \le t < 7$	$\begin{bmatrix} 0 & 5 \end{bmatrix}$	$\begin{bmatrix} 4 & 1 \end{bmatrix}$
$7 \le t < 10$	$\begin{bmatrix} 4 & 1 \end{bmatrix}$	$\begin{bmatrix} 4 & 1 \end{bmatrix}$
$10 \le t < 14$	$\begin{bmatrix} 4 & 1 \end{bmatrix}$	$\begin{bmatrix} 3 & 5 \end{bmatrix}$
$14 \le t < 17$	$\begin{bmatrix} 3 & 5 \end{bmatrix}$	$\begin{bmatrix} 3 & 5 \end{bmatrix}$
$17 \le t < 21$	$\begin{bmatrix} 3 & 5 \end{bmatrix}$	$\begin{bmatrix} -3 & 4 \end{bmatrix}$
$21 \le t < 25$	$\begin{bmatrix} -3 & 4 \end{bmatrix}$	$\begin{bmatrix} -3 & 4 \end{bmatrix}$
$25 \le t < 29$	$\begin{bmatrix} -3 & 4 \end{bmatrix}$	$\begin{bmatrix} 0 & 5 \end{bmatrix}$
$29 \le t < 37$	$\begin{bmatrix} 0 & 5 \end{bmatrix}$	$\begin{bmatrix} 0 & 5 \end{bmatrix}$

The desired trajectory of the payload is chosen based on the smooth fifth-order polynomial

$$\boldsymbol{\rho}_d = \left(10\hat{t}^3 - 15\hat{t}^4 + 6\hat{t}^5\right)(\boldsymbol{\rho}_f - \boldsymbol{\rho}_i) + \boldsymbol{\rho}_i,$$

where $\hat{t} = (t - t_i)/(t_f - t_i)$, t_i is the initial time, t_f is the final time, $\boldsymbol{\rho}_i$ is the initial position, and $\boldsymbol{\rho}_f$ is the desired final position of the trajectory. Four instances of this trajectory are performed sequentially in 4 second intervals with a 3 second rest period in between. The numerical parameters of the desired trajectory are given in Table 3.1. Numerical simulation results are presented in Figures 3.2 to 3.5, including the payload trajectory versus time in Figure 3.2, the position

tracking error versus time in Figure 3.3, the velocity tracking error versus time in Figure 3.4, and the control inputs versus time in Figure 3.5. For clarity, the figure captions and axis labels refer to the "x-axis" and "y-axis" instead of $\underrightarrow{a}^1$ and $\underrightarrow{a}^2$, where $\boldsymbol{\rho}^\mathsf{T} = \begin{bmatrix} \rho_x & \rho_y \end{bmatrix}$ and $\dot{\boldsymbol{\rho}}^\mathsf{T} = \begin{bmatrix} \dot{\rho}_x & \dot{\rho}_y \end{bmatrix}$.

The results show that both the μ-tip and true payload tracking errors remain small throughout the simulation. The μ-tip tracking errors converge quicker than the true payload tracking errors, which is to be expected since the filtered error control law in (3.18) acts on the μ-tip errors. In Figure 3.3, $\tilde{\boldsymbol{\rho}}_x$ does not converge to zero prior to the end of the simulation, while $\tilde{\boldsymbol{\rho}}_{\mu x}$ does, which further motivates the importance of choosing a value of μ close to one for performance. To demonstrate the robustness of the control law in (3.18) to gain uncertainty, simulations with larger values of $\mathbf{K}_d$ are performed, which result in the closed-loop system remaining input-output stable. Results of the simulations with increased values of $\mathbf{K}_d$ are omitted in the interest of brevity.

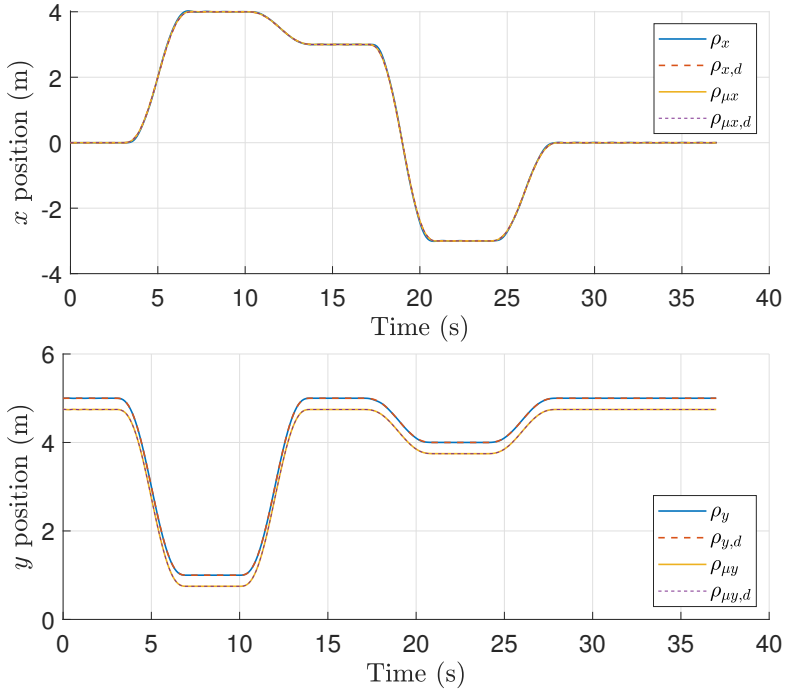

Figure 3.2: Payload position trajectories with the control law in (3.18).

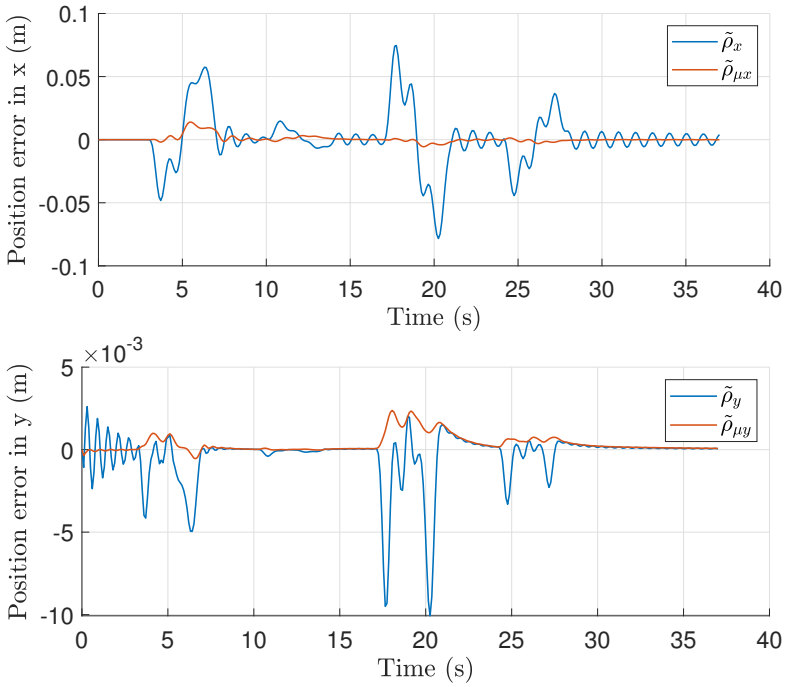

Figure 3.3: Payload position tracking errors with the control law in (3.18).

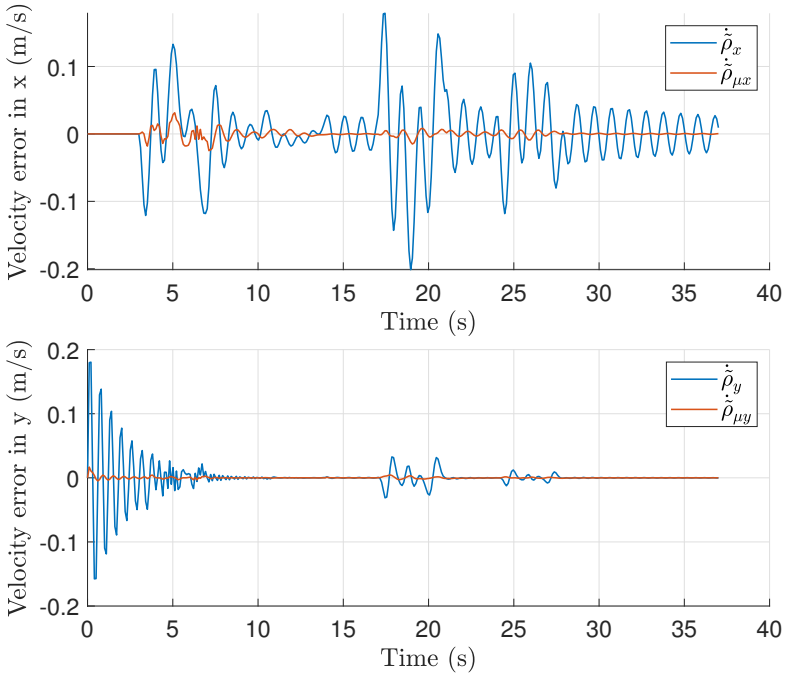

Figure 3.4: Payload velocity tracking errors with the control law in (3.18).

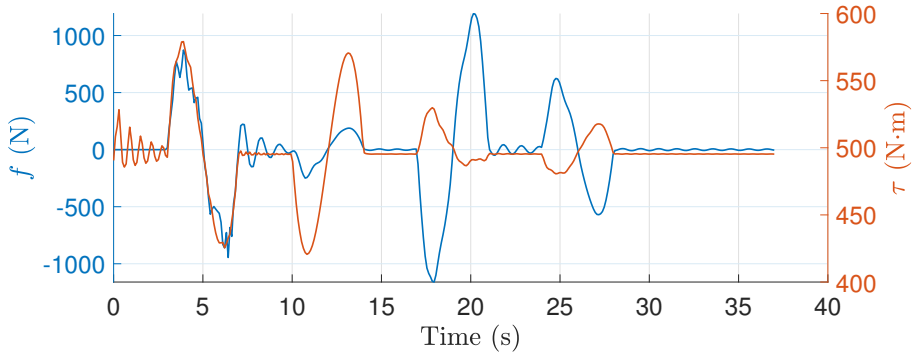

Figure 3.5: Control inputs f (blue) and τ (orange) with the control law in (3.18).

To demonstrate the benefit of using the μ-tip position and velocity in the controller formulation, a comparison to proportional-derivative (PD) control with the true payload position and velocity is performed with results shown in Figure 3.6. Different variations of feedforward control are implemented with the PD controller, including (3.8) (labeled PD_1), a modification of (3.8) replacing $\boldsymbol{\rho}_r$ with $\boldsymbol{\rho}_d$ (labeled PD_2), and a feedforward input based only on gravity compensation (labeled PD_3). In all cases, the gain of the PD controller was severely limited to prevent the closed-loop from becoming unstable, resulting in very poor tracking performance. This emphasizes the benefit of the μ-tip position and μ-tip rate when developing a controller for the tower crane.

3.5 Conclusion

The μ-tip control method in a passive input-output mapping $(\hat{\boldsymbol{\tau}}_c - \hat{\boldsymbol{\tau}}_r) \mapsto \mathbf{s}_\mu$. An ISP feedback controller is implemented and is shown to render the closed-loop system input-output stable using the Passivity Theorem, while guaranteeing that the velocity tracking error $\tilde{\boldsymbol{\rho}}$ is asymptotically stable. The numerical simulation demonstrates the performance and robustness of the proposed control law. Note that the two presented stability analyses in Sections 3.3.1 and 3.3.2 rely on assumptions that θ and $\dot{\theta}$ are small, and the payload is massive, which allow for the approximation $\mathbf{J}_{\text{flex}} \approx \mathbf{J}_{\text{flex},d} \approx \mathbf{J}_{\text{flex}}|_{\mu=1}$. These assumptions guarantee stability

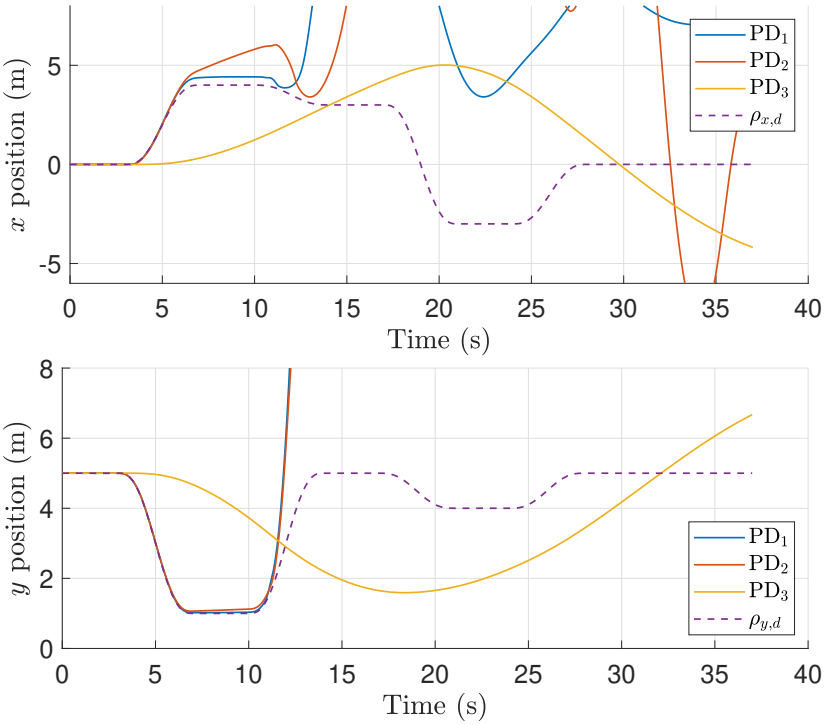

Figure 3.6: Payload position trajectories with PD control.

and robustness of the payload velocity tracking, but rely on the sway angle and its angular rate remaining small, which is not guaranteed, and could potentially result in closed-loop instability in practice. The sliding-mode-inspired control approach presented in Chapter 4 does not require these restrictive assumptions and provides a practical control alternative to the μ-tip approach.

Chapter 4

Passivity-Based Adaptive Sliding-Mode-Inspired Control

4.1 Introduction

In Chapter 3, a μ-tip passivity-based control method was derived to ensure tip tracking of the payload velocity and position. However, the stability analysis of this control method relied on the assumption that the sway angle θ is small and the scaling parameter μ is close to 1, ensuring that $\mathbf{J}_{\text{flex}} \approx \mathbf{J}_{\text{flex},d} \approx \mathbf{J}_{\text{flex}}|_{\mu=1}$. These assumptions severely limit the practicality of the proposed tower crane control method. Inspired by the adaptive sliding-mode control in [31, 32], a sliding-mode control approach is proposed in this chapter that does not rely on the restrictive assumptions of small sway angle θ and its angular rate $\dot{\theta}$. To simplify the control problem and focus on the effect of the sway angle, the elasticity of the hoist cable is removed from the dynamics, and the hoist cable is considered as a rigid bar with a time varying length in this chapter. Section 4.2 decouples the dynamics into actuated and unactuated ODEs, and reformulates the system dynamics. The novel contribution of the proposed method is presented in Section 4.3. The method in [31, 32] uses Lyapunov stability theory to prove stability of the closed-loop adaptive control law that drives the system asymptotically to the sliding surface.

Alternatively, the Passivity Theorem is used to prove closed-loop input-output stability in this chapter. Section 4.3.1 uses a similar approach to define the sliding surface and its dynamics, as well as the the reference acceleration. The method in [32] uses the actuated and unactuated states, $\mathbf{q}_a$ and q_u, to define a sliding surface, and uses a "model specific" adaptive update law to estimate uncertainties in the payload mass and damping coefficients. Section 4.3.2 uses Damaren's adaptive approach [42, 43] to define a more general adaptive update that can apply to the model. Section 4.4 further applies the novel adaptive sliding-mode control method to the system transformed into $\boldsymbol{\rho}$ coordinates which can be seen as a step towards a μ-tip inspired extension of the approach outlined in this chapter. The numerical simulations of the control methods proposed in Sections 4.3 and 4.4 applied to the tower crane dynamic model in Section 4.2 are presented in Section 4.5.

4.2 Dynamic Reformulation

To simplify the control problem and focus on the effect of the sway angle, the elasticity of the hoist cable is neglected from the dynamics. This section presents the system dynamics with a rigid hoist cable.

4.2.1 Decoupled Dynamics

In Section 2.5, the equations of motion of the tower crane with a flexible hoist cable were derived as

$$\mathbf{M}\ddot{\mathbf{q}} + \mathbf{D}\dot{\mathbf{q}} + \mathbf{K}\mathbf{q} = \mathbf{f} + \mathbf{f}_{non}\left(\mathbf{q}, \dot{\mathbf{q}}\right). \tag{2.6}$$

To model the hoist cable as rigid, $\mathbf{q}^e$ and $\mathbf{K}$ are set to zero, and the rows and columns associated with the elastic coordinates are removed. The equations of

motion can then be written in the form

$$\begin{bmatrix} M_{11} & M_{12} & M_{13} \\ * & M_{22} & M_{23} \\ * & * & M_{33} \end{bmatrix} \begin{bmatrix} \ddot{x}_a \\ \ddot{\phi} \\ \ddot{\theta} \end{bmatrix} + \begin{bmatrix} 0 & 0 & 0 \\ 0 & 0 & 0 \\ 0 & 0 & c_\theta \end{bmatrix} \begin{bmatrix} \dot{x}_a \\ \dot{\phi} \\ \dot{\theta} \end{bmatrix}$$
$$= \begin{bmatrix} \hat{\mathbf{f}} \\ 0 \end{bmatrix} + \begin{bmatrix} C_{n,11} & C_{n,12} & C_{n,13} \\ C_{n,21} & C_{n,22} & C_{n,23} \\ C_{n,31} & C_{n,32} & C_{n,33} \end{bmatrix} \begin{bmatrix} \dot{x}_a \\ \dot{\phi} \\ \dot{\theta} \end{bmatrix} + \begin{bmatrix} G_{n,1} \\ G_{n,2} \\ G_{n,3} \end{bmatrix},$$

with all the components from Section 2.5 evaluated at $\mathbf{q}^e = \mathbf{0}$. The entries of the mass matrix $\mathbf{M}$ and the nonlinear matrix $\mathbf{f}_{non}$ can be found in Appendix A.

Partitioning the dynamics above into actuated coordinates $\mathbf{q}_a = \begin{bmatrix} x_a & \phi \end{bmatrix}^\mathsf{T}$ and the unactuated coordinate $q_u = \theta$, the equations of motion become

$$\begin{bmatrix} M_{11} & M_{12} \\ * & M_{22} \end{bmatrix} \ddot{\mathbf{q}}_a + \begin{bmatrix} M_{13} \\ M_{23} \end{bmatrix} \ddot{q}_u$$
$$= \hat{\mathbf{f}} + \begin{bmatrix} C_{n,11} & C_{n,12} \\ C_{n,21} & C_{n,22} \end{bmatrix} \dot{\mathbf{q}}_a + \begin{bmatrix} C_{n,13} \\ C_{n,23} \end{bmatrix} \dot{q}_u + \begin{bmatrix} G_{n,1} \\ G_{n,2} \end{bmatrix}, \tag{4.1}$$

$$\begin{bmatrix} M_{13} & M_{23} \end{bmatrix} \ddot{\mathbf{q}}_a + M_{33}\ddot{q}_u + c_\theta \dot{q}_u = \begin{bmatrix} C_{n,31} & C_{n,32} \end{bmatrix} \dot{\mathbf{q}}_a + C_{n,33}\dot{q}_u + G_{n,3}. \tag{4.2}$$

Eqn. (4.2) can be rearranged as a function describing the unactuated acceleration

$$\ddot{q}_u = \frac{1}{M_{33}} \left(- \begin{bmatrix} M_{13} & M_{23} \end{bmatrix} \ddot{\mathbf{q}}_a + \begin{bmatrix} C_{n,31} & C_{n,32} \end{bmatrix} \dot{\mathbf{q}}_a + (C_{n,33} - c_\theta)\dot{q}_u + G_{n,3} \right). \tag{4.3}$$

which will be used to construct the reformulated dynamics in Section 4.2.2.

4.2.2 Reformulated Dynamics

Substituting the autonomous ODE (4.3) into the nonautonomous ODE (4.1), we obtain a single nonautonomous ODE. The equations of motion are reformulated

as

$$\bar{\mathbf{M}}(\mathbf{q})\ddot{\mathbf{q}}_a + \bar{\mathbf{B}}\left(\mathbf{q}, \dot{\mathbf{q}}\right)\dot{\mathbf{q}}_a + \bar{\mathbf{C}}\left(\mathbf{q}, \dot{\mathbf{q}}\right)\dot{q}_u + \bar{\mathbf{G}}(\mathbf{q}) = \mathbf{U}, \tag{4.4}$$

where $\mathbf{U} = \hat{\mathbf{f}}$,

$$\bar{\mathbf{M}}(\mathbf{q}) = \begin{bmatrix} \bar{M}_{11} & \bar{M}_{12} \\ \bar{M}_{21} & \bar{M}_{22} \end{bmatrix} = \begin{bmatrix} M_{11} - \frac{M_{13}^2}{M_{33}} & M_{12} - \frac{M_{23}M_{13}}{M_{33}} \\ * & M_{22} - \frac{M_{23}^2}{M_{33}} \end{bmatrix},$$

$$\bar{\mathbf{B}}\left(\mathbf{q}, \dot{\mathbf{q}}\right) = \begin{bmatrix} \bar{B}_{11} & \bar{B}_{12} \\ \bar{B}_{21} & \bar{B}_{22} \end{bmatrix} = \begin{bmatrix} -C_{n,11} + \frac{M_{13}C_{n,31}}{M_{33}} & -C_{n,12} + \frac{M_{13}C_{n,32}}{M_{33}} \\ -C_{n,21} + \frac{M_{23}C_{n,31}}{M_{33}} & -C_{n,22} + \frac{M_{23}C_{n,32}}{M_{33}} \end{bmatrix},$$

$$\bar{\mathbf{C}}\left(\mathbf{q}, \dot{\mathbf{q}}\right) = \begin{bmatrix} \bar{C}_1 \\ \bar{C}_2 \end{bmatrix} = \begin{bmatrix} -C_{n,13} + \frac{M_{13}}{M_{33}}(C_{n,33} - c_\theta) \\ -C_{n,23} + \frac{M_{23}}{M_{33}}(C_{n,33} - c_\theta) \end{bmatrix},$$

$$\bar{\mathbf{G}}(\mathbf{q}) = \begin{bmatrix} \bar{G}_1 \\ \bar{G}_2 \end{bmatrix} = \begin{bmatrix} -\frac{M_{13}}{M_{33}}G_{n,3} - G_{n,1} \\ -\frac{M_{23}}{M_{33}}G_{n,3} - G_{n,2} \end{bmatrix},$$

with all the components from Section 2.5 evaluated at $\mathbf{q}^e = \mathbf{0}$. The reformulated equations of motion in (4.4) are used to analyze closed-loop stability of the tower crane with a rigid hoist cable in Section 4.3.

4.2.3 Positiveness of $\bar{\mathbf{M}}$

The positive definiteness of the matrix $\bar{\mathbf{M}}$ is used in the passivity analysis in Sections 4.3.3 and 4.4.4. From (4.4), the mass matrix $\bar{\mathbf{M}}$ is defined as

$$\bar{\mathbf{M}} = \begin{bmatrix} M_{11} - \frac{M_{13}^2}{M_{33}} & M_{12} - \frac{M_{23}M_{13}}{M_{33}} \\ * & M_{22} - \frac{M_{23}^2}{M_{33}} \end{bmatrix},$$

where

$$
\begin{aligned}
M_{11} &= m_1 + m_2 + m_w + \rho_c A L, \\
M_{12} &= r \sin\theta \left(m_2 + \rho_c A \ell_i\right), \\
M_{13} &= -\cos\theta \left(m_2 \ell_i + \tfrac{1}{2}\rho_c A \ell_i^2\right), \\
M_{22} &= r^2 \left(\tfrac{1}{2} m_w + m_2 + \rho_c A L\right), \\
M_{23} &= 0, \\
M_{33} &= \ell_i^2 \left(m_2 + \tfrac{1}{3}\rho_c A \ell_i\right),
\end{aligned}
$$

which are the entries of $\mathbf{M}$ in Appendix A evaluated at $\mathbf{q}^e = \mathbf{0}$. The mass matrix $\bar{\mathbf{M}}(\phi, \theta)$ can then be written as

$$
\bar{\mathbf{M}} = \begin{bmatrix} m_1 + m_w + m_2 + \rho_c A L - \cos^2\theta \frac{\left(m_2 + \frac{1}{2}\rho_c A \ell_i\right)^2}{m_2 + \frac{1}{3}\rho_c A \ell_i} & r \sin\theta \left(m_2 + \rho_c A \ell_i\right) \\ * & r^2 \left(\frac{1}{2} m_w + m_2 + \rho_c A L\right) \end{bmatrix}.
$$

Since it is not simple to analytically show that $\bar{\mathbf{M}} > 0$, it is instead numerically verified that the minimum eigenvalue of $\bar{\mathbf{M}}$ is strictly greater than zero for values of θ and ϕ in the range $-\frac{\pi}{2} < \theta < \frac{\pi}{2}$ and $0 < \phi < \frac{L}{r}$. Figure 4.1b shows the minimum eigenvalues of $\bar{\mathbf{M}}$ with the same numerical values of the winch and hoist cable as Section 3.4, where $m_w = 20$ kg, $r = 0.1$ m, $\rho_c = 1000$ kg/m^3, $L = 5$ m, and $r_c = 0.002$ m. In Figure 4.1b, a second set of mass properties is included to demonstrate that $\bar{\mathbf{M}}$ remains positive definite for variations in these properties.

4.3 Adaptive Sliding-Mode Control in $\mathbf{q}_a$ Coordinates

An adaptive sliding-mode passivity-based control method inspired by [31, 32] is derived and analyzed in this section. In particular, Section 4.3.1 defines the sliding surface and its dynamics, Section 4.3.2 introduces an adaptive control law, and

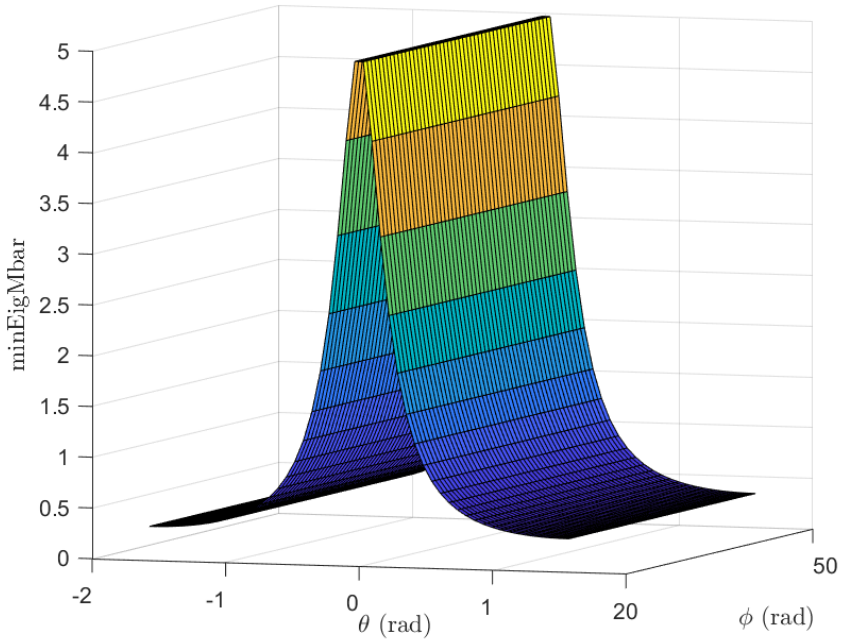

(a) Minimum eigenvalues of $\bar{\mathbf{M}}$ when $m_1 = 5$ kg, $m_2 = 500$ kg, $m_w = 20$ kg.

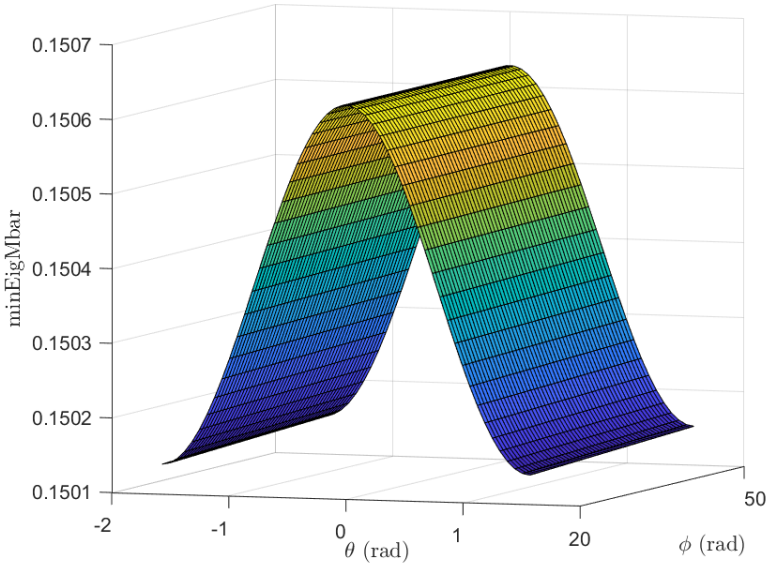

(b) Minimum eigenvalues of $\bar{\mathbf{M}}$ when $m_1 = 500$ kg, $m_2 = 5$ kg, $m_w = 20$ kg.

Figure 4.1: Positive definiteness of $\bar{\mathbf{M}}$ using numerical verification of the minimum eigenvalues of $\bar{\mathbf{M}}$ being positive in the range of $-\frac{\pi}{2} < \theta < \frac{\pi}{2}$ and $0 < \phi < \frac{L}{r}$.

passivity and closed-loop stability analyses are included in Section 4.3.3.

4.3.1 Sliding Mode and Sliding Surface

Inspired by the sliding-mode control method in [31, 32], the sliding surface dynamics

$$\dot{\mathbf{s}} + \boldsymbol{\lambda}\mathbf{s} = \mathbf{0} \tag{4.5}$$

are introduced, where $\mathbf{s} \in \mathbb{R}^2$ and $\boldsymbol{\lambda} = \boldsymbol{\lambda}^\mathsf{T} > 0$. This choice of sliding surface dynamics ensures that $\mathbf{s}(t) \to \mathbf{0}$ as $t \to \infty$ [32] for all $\mathbf{s}(0) = \mathbf{s}_0$. The sliding surface is defined as

$$\mathbf{s} = \begin{bmatrix} s_1 \\ s_2 \end{bmatrix} = \dot{\tilde{\mathbf{q}}}_a + \boldsymbol{\lambda}\tilde{\mathbf{q}}_a + \boldsymbol{\alpha} q_u, \tag{4.6}$$

where $\dot{\tilde{\mathbf{q}}}_a = \dot{\mathbf{q}}_a - \dot{\mathbf{q}}_{a,d}$, and $\tilde{\mathbf{q}}_a = \mathbf{q}_a - \mathbf{q}_{a,d}$ are tracking errors, and $\boldsymbol{\lambda} = \mathrm{diag}(\lambda_1, \lambda_2)$, $\boldsymbol{\alpha} = \begin{bmatrix} \alpha & 0 \end{bmatrix}^\mathsf{T}$ are constant control parameters. The time derivative of the sliding surface is

$$\dot{\mathbf{s}} = \ddot{\tilde{\mathbf{q}}}_a + \boldsymbol{\lambda}\dot{\tilde{\mathbf{q}}}_a + \boldsymbol{\alpha}\dot{q}_u, \tag{4.7}$$

where $\ddot{\tilde{\mathbf{q}}}_a = \ddot{\mathbf{q}}_a - \ddot{\mathbf{q}}_{a,d}$. From (4.6) and (4.7), the dynamics of the sliding surface are defined as

$$\dot{\mathbf{s}} + \boldsymbol{\lambda}\mathbf{s} = \ddot{\tilde{\mathbf{q}}}_a + 2\boldsymbol{\lambda}\dot{\tilde{\mathbf{q}}}_a + \boldsymbol{\lambda}^\mathsf{T}\boldsymbol{\lambda}\tilde{\mathbf{q}}_a + \boldsymbol{\alpha}\dot{q}_u + \boldsymbol{\lambda}\boldsymbol{\alpha} q_u. \tag{4.8}$$

Based on (4.8), we define the reference acceleration

$$\begin{aligned} \ddot{\mathbf{q}}_{a,r} &= \ddot{\mathbf{q}}_a - (\dot{\mathbf{s}} + \boldsymbol{\lambda}\mathbf{s}) \\ &= \ddot{\mathbf{q}}_{a,d} - 2\boldsymbol{\lambda}\dot{\tilde{\mathbf{q}}}_a - \boldsymbol{\lambda}^\mathsf{T}\boldsymbol{\lambda}\tilde{\mathbf{q}}_a - \boldsymbol{\alpha}\dot{q}_u - \boldsymbol{\lambda}\boldsymbol{\alpha} q_u, \end{aligned} \tag{4.9}$$

which will be used as the reference acceleration in the actuated coordinates that guides the system dynamics towards the designed sliding surface. It is worth noting that $\ddot{\mathbf{q}}_a - \ddot{\mathbf{q}}_{a,r} = \dot{\mathbf{s}} + \boldsymbol{\lambda}\mathbf{s}$ by the definition of (4.9).

4.3.2 Adaptive Control

The sliding-mode control method in [32] relies on a feedforward control input involving the system dynamics. Due to uncertainty in the parameters of the dynamic model, an adaptive feedforward control input is used. However, the adaptive control law used in [32] exploits the specific parametric structure of the equations of motion of the crane in [32]. In order to expand the applicability of this control law, the adaptive portion of the control law is modified based on the more generic regressor form found in [42].

Define the input

$$\mathbf{U} = \mathbf{W}\mathbf{a} = \bar{\mathbf{M}}\left(\mathbf{q}\right)\ddot{\mathbf{q}}_{a,r} + \bar{\mathbf{B}}\left(\mathbf{q},\dot{\mathbf{q}}\right)\dot{\mathbf{q}}_{a} + \bar{\mathbf{C}}\left(\mathbf{q},\dot{\mathbf{q}}\right)\dot{q}_{u} + \bar{\mathbf{G}}(\mathbf{q}),$$

where $\mathbf{W}$ is the regressor, and $\mathbf{a}$ is the matrix containing the true mass and nonlinear terms in the reformulated dynamics (4.4) capturing the true dynamics of the system with the reference acceleration. These matrices are given by

$$\mathbf{W} = \begin{bmatrix} \ddot{\mathbf{q}}_{a,r}^{\mathsf{T}} & \mathbf{0}_{1\times 2} & \dot{\mathbf{q}}_{a}^{\mathsf{T}} & \mathbf{0}_{1\times 2} & \dot{q}_u & 0 & 1 & 0 \\ \mathbf{0}_{1\times 2} & \ddot{\mathbf{q}}_{a,r}^{\mathsf{T}} & \mathbf{0}_{1\times 2} & \dot{\mathbf{q}}_{a}^{\mathsf{T}} & 0 & \dot{q}_u & 0 & 1 \end{bmatrix},$$

$$\mathbf{a} = \begin{bmatrix} \bar{\mathbf{m}}^{\mathsf{T}} & \bar{\mathbf{b}}^{\mathsf{T}} & \bar{\mathbf{c}}^{\mathsf{T}} & \bar{\mathbf{g}}^{\mathsf{T}} \end{bmatrix}^{\mathsf{T}},$$

where the entries of $\mathbf{a}$ are the vectorized matrices of the reformulated dynamics (4.4), $\bar{\mathbf{m}} = \begin{bmatrix} \bar{M}_{11} & \bar{M}_{12} & \bar{M}_{21} & \bar{M}_{22} \end{bmatrix}^{\mathsf{T}}$, $\bar{\mathbf{b}} = \begin{bmatrix} \bar{B}_{11} & \bar{B}_{12} & \bar{B}_{21} & \bar{B}_{22} \end{bmatrix}^{\mathsf{T}}$, $\bar{\mathbf{c}} = \begin{bmatrix} \bar{C}_1 & \bar{C}_2 \end{bmatrix}^{\mathsf{T}}$, and $\bar{\mathbf{g}} = \begin{bmatrix} \bar{G}_1 & \bar{G}_2 \end{bmatrix}^{\mathsf{T}}$. It is assumed that the regressor $\mathbf{W}$ perfectly measures the states of the system and being perfectly known.

The time derivative of $\bar{\mathbf{M}}(\phi,\theta)$ can be written as

$$\dot{\bar{\mathbf{M}}} = \frac{\mathrm{d}}{\mathrm{d}t}\bar{\mathbf{M}}(\phi,\theta) = \left.\frac{\partial\bar{\mathbf{M}}}{\partial\theta}\right|_{\phi,\theta}\dot{\theta} + \left.\frac{\partial\bar{\mathbf{M}}}{\partial\phi}\right|_{\phi,\theta}\dot{\phi}, \tag{4.10}$$

where $\frac{\partial\bar{\mathbf{M}}}{\partial\theta} = \frac{\partial\bar{\mathbf{M}}}{\partial\theta}^{\mathsf{T}}$ and $\frac{\partial\bar{\mathbf{M}}}{\partial\phi} = \frac{\partial\bar{\mathbf{M}}}{\partial\phi}^{\mathsf{T}}$. Upper bounds on the eigenvalues of $\frac{\partial\bar{\mathbf{M}}}{\partial\theta}$ and $\frac{\partial\bar{\mathbf{M}}}{\partial\phi}$

are given by the constants δ_θ and δ_ϕ, respectively. These upper bounds can be equivalently described by the matrix inequalities

$$\frac{\partial \bar{\mathbf{M}}}{\partial \theta} < \delta_\theta \mathbf{1}, \tag{4.11}$$

$$\frac{\partial \bar{\mathbf{M}}}{\partial \phi} < \delta_\phi \mathbf{1}. \tag{4.12}$$

Adding the matrix inequalities in (4.11) and (4.12), and substituting the result into(4.10) yields

$$\dot{\bar{\mathbf{M}}} < (\delta_\theta \dot{\theta} + \delta_\phi \dot{\phi})\mathbf{1}.$$

The adaptive feedforward control input is designed as

$$\begin{aligned} \hat{\mathbf{U}} &= \mathbf{W}\hat{\mathbf{a}} - \tfrac{1}{2}(\delta_\theta \dot{\theta} + \delta_\phi \dot{\phi})\mathbf{s} \\ &= \hat{\mathbf{M}}(\mathbf{q})\,\ddot{\mathbf{q}}_{a,r} + \hat{\mathbf{B}}(\mathbf{q}, \dot{\mathbf{q}})\,\dot{\mathbf{q}}_a + \hat{\mathbf{C}}(\mathbf{q}, \dot{\mathbf{q}})\,\dot{q}_u + \hat{\mathbf{G}}(\mathbf{q}) - \tfrac{1}{2}(\delta_\theta \dot{\theta} + \delta_\phi \dot{\phi})\mathbf{s}, \end{aligned} \tag{4.13}$$

where $\hat{\mathbf{a}} = \begin{bmatrix} \hat{\mathbf{m}}^\mathsf{T} & \hat{\mathbf{b}}^\mathsf{T} & \hat{\mathbf{c}}^\mathsf{T} & \hat{\mathbf{g}}^\mathsf{T} \end{bmatrix}^\mathsf{T}$, and the matrices $\hat{\mathbf{m}} = \begin{bmatrix} \hat{M}_{11} & \hat{M}_{12} & \hat{M}_{21} & \hat{M}_{22} \end{bmatrix}^\mathsf{T}$, $\hat{\mathbf{b}} = \begin{bmatrix} \hat{B}_{11} & \hat{B}_{12} & \hat{B}_{21} & \hat{B}_{22} \end{bmatrix}^\mathsf{T}$, $\hat{\mathbf{c}} = \begin{bmatrix} \hat{C}_1 & \hat{C}_2 \end{bmatrix}^\mathsf{T}$, $\hat{\mathbf{g}} = \begin{bmatrix} \hat{G}_1 & \hat{G}_2 \end{bmatrix}^\mathsf{T}$ are the estimates of the true matrices $\bar{\mathbf{M}}$, $\bar{\mathbf{B}}$, $\bar{\mathbf{C}}$, and $\bar{\mathbf{G}}$.

Let $\mathbf{U} = \hat{\mathbf{U}} + \bar{\mathbf{u}}$, where $\bar{\mathbf{u}}$ is a feedback control input to be designed. Substituting (4.13) into (4.4) gives

$$\bar{\mathbf{M}}\ddot{\mathbf{q}}_a = \hat{\mathbf{M}}\ddot{\mathbf{q}}_{a,r} + \tilde{\mathbf{B}}\dot{\mathbf{q}}_a + \tilde{\mathbf{C}}\dot{q}_u + \tilde{\mathbf{G}} - \tfrac{1}{2}(\delta_\theta \dot{\theta} + \delta_\phi \dot{\phi})\mathbf{s} + \bar{\mathbf{u}},$$

where $\tilde{\mathbf{B}} = \hat{\mathbf{B}}(\mathbf{q}, \dot{\mathbf{q}}) - \bar{\mathbf{B}}(\mathbf{q}, \dot{\mathbf{q}})$, $\tilde{\mathbf{C}} = \hat{\mathbf{C}}(\mathbf{q}, \dot{\mathbf{q}}) - \bar{\mathbf{C}}(\mathbf{q}, \dot{\mathbf{q}})$, $\tilde{\mathbf{G}} = \hat{\mathbf{G}}(\mathbf{q}) - \bar{\mathbf{G}}(\mathbf{q})$. Subtracting $\bar{\mathbf{M}}\ddot{\mathbf{q}}_{a,r}$ from both sides gives

$$\bar{\mathbf{M}}(\ddot{\mathbf{q}}_a - \ddot{\mathbf{q}}_{a,r}) = \tilde{\mathbf{M}}\ddot{\mathbf{q}}_{a,r} + \tilde{\mathbf{B}}\dot{\mathbf{q}}_a + \tilde{\mathbf{C}}\dot{q}_u + \tilde{\mathbf{G}} - \tfrac{1}{2}(\delta_\theta \dot{\theta} + \delta_\phi \dot{\phi})\mathbf{s} + \bar{\mathbf{u}},$$

where $\tilde{\mathbf{M}} = \hat{\mathbf{M}}(\mathbf{q}) - \bar{\mathbf{M}}(\mathbf{q})$. Substituting $\ddot{\mathbf{q}}_a - \ddot{\mathbf{q}}_{a,r} = \dot{\mathbf{s}} + \boldsymbol{\lambda}\mathbf{s}$ given by (4.9) yields

the error dynamics

$$\bar{\mathbf{M}}\left(\dot{\mathbf{s}}+\boldsymbol{\lambda}\mathbf{s}\right)=\tilde{\mathbf{M}}\ddot{\mathbf{q}}_{a,r}+\tilde{\mathbf{B}}\dot{\mathbf{q}}_a+\tilde{\mathbf{C}}\dot{q}_u+\tilde{\mathbf{G}}-\tfrac{1}{2}(\delta_\theta\dot{\theta}+\delta_\phi\dot{\phi})\mathbf{s}+\bar{\mathbf{u}},$$

which can be rearranged as

$$\bar{\mathbf{M}}\dot{\mathbf{s}}=\tilde{\mathbf{M}}\ddot{\mathbf{q}}_{a,r}+\tilde{\mathbf{B}}\dot{\mathbf{q}}_a+\tilde{\mathbf{C}}\dot{q}_u+\tilde{\mathbf{G}}+\bar{\mathbf{u}}-\tfrac{1}{2}(\delta_\theta\dot{\theta}+\delta_\phi\dot{\phi})\mathbf{s}-\bar{\mathbf{M}}\boldsymbol{\lambda}\mathbf{s}. \tag{4.14}$$

Notice that

$$\mathbf{W}\tilde{\mathbf{a}}=\mathbf{W}(\hat{\mathbf{a}}-\mathbf{a})=\tilde{\mathbf{M}}\ddot{\mathbf{q}}_{a,r}+\tilde{\mathbf{B}}\dot{\mathbf{q}}_a+\tilde{\mathbf{C}}\dot{q}_u+\tilde{\mathbf{G}}, \tag{4.15}$$

and therefore (4.14) can be rewritten as

$$\bar{\mathbf{M}}\dot{\mathbf{s}}=\mathbf{W}\tilde{\mathbf{a}}-\tfrac{1}{2}(\delta_\theta\dot{\theta}+\delta_\phi\dot{\phi})\mathbf{s}-\bar{\mathbf{M}}\boldsymbol{\lambda}\mathbf{s}+\bar{\mathbf{u}}. \tag{4.16}$$

4.3.3 Passivity and Closed-Loop Stability Analysis

Theorem 5 (Passive Input-Output Map $\bar{\mathbf{u}}\mapsto\mathbf{s}$)**.** *Consider the system with error dynamics defined in* (4.16)*, where the term* $\hat{\mathbf{U}}$ *is updated based on the adaptive law* $\dot{\hat{\mathbf{a}}}=-\boldsymbol{\Gamma}^{\mathsf{T}}\mathbf{W}^{\mathsf{T}}\mathbf{s}$*, where* $\boldsymbol{\Gamma}=\boldsymbol{\Gamma}^{\mathsf{T}}>0$*, and it is assumed that* $\mathbf{a}$ *is approximately constant. The input-output mapping* $\bar{\mathbf{u}}\mapsto\mathbf{s}$ *is passive.*

Proof. Consider the nonnegative function

$$V=\tfrac{1}{2}\mathbf{s}^{\mathsf{T}}\bar{\mathbf{M}}\mathbf{s}+\tfrac{1}{2}\tilde{\mathbf{a}}^{\mathsf{T}}\boldsymbol{\Gamma}^{-1}\tilde{\mathbf{a}}. \tag{4.17}$$

Taking the time derivative of (4.17) and substituting in (4.16) gives

$$\dot{V}=\mathbf{s}^{\mathsf{T}}\bar{\mathbf{M}}\dot{\mathbf{s}}+\tfrac{1}{2}\mathbf{s}^{\mathsf{T}}\dot{\bar{\mathbf{M}}}\mathbf{s}+\dot{\tilde{\mathbf{a}}}^{\mathsf{T}}\boldsymbol{\Gamma}^{-1}\tilde{\mathbf{a}}.$$

$$\begin{aligned}\dot{V} &= \mathbf{s}^{\mathsf{T}}\bar{\mathbf{M}}\dot{\mathbf{s}} + \tfrac{1}{2}\mathbf{s}^{\mathsf{T}}\dot{\bar{\mathbf{M}}}\mathbf{s} + \dot{\tilde{\mathbf{a}}}^{\mathsf{T}}\boldsymbol{\Gamma}^{-1}\tilde{\mathbf{a}} \\ &= \mathbf{s}^{\mathsf{T}}\left(\mathbf{W}\tilde{\mathbf{a}} - \tfrac{1}{2}(\delta_\theta\dot{\theta} + \delta_\phi\dot{\phi})\mathbf{s} - \bar{\mathbf{M}}\boldsymbol{\lambda}\mathbf{s} + \bar{\mathbf{u}}\right) + \tfrac{1}{2}\mathbf{s}^{\mathsf{T}}\dot{\bar{\mathbf{M}}}\mathbf{s} + \dot{\tilde{\mathbf{a}}}^{\mathsf{T}}\boldsymbol{\Gamma}^{-1}\tilde{\mathbf{a}} \\ &= \mathbf{s}^{\mathsf{T}}\bar{\mathbf{u}} - \mathbf{s}^{\mathsf{T}}\bar{\mathbf{M}}\boldsymbol{\lambda}\mathbf{s} + \tfrac{1}{2}\mathbf{s}^{\mathsf{T}}\left(\dot{\bar{\mathbf{M}}} - (\delta_\theta\dot{\theta} + \delta_\phi\dot{\phi})\mathbf{1}\right)\mathbf{s} + \left(\mathbf{s}^{\mathsf{T}}\mathbf{W} + \dot{\tilde{\mathbf{a}}}^{\mathsf{T}}\boldsymbol{\Gamma}^{-1}\right)\tilde{\mathbf{a}}. \qquad (4.18)\end{aligned}$$

Since it is assumed that $\mathbf{a}$ is constant, $\dot{\tilde{\mathbf{a}}} = \dot{\hat{\mathbf{a}}}$ and $\mathbf{s}^{\mathsf{T}}\mathbf{W} + \dot{\tilde{\mathbf{a}}}^{\mathsf{T}}\boldsymbol{\Gamma}^{-1} = \mathbf{s}^{\mathsf{T}}\mathbf{W} + \dot{\hat{\mathbf{a}}}^{\mathsf{T}}\boldsymbol{\Gamma}^{-1}$. Substituting in the adaptive law $\dot{\hat{\mathbf{a}}} = -\boldsymbol{\Gamma}^{\mathsf{T}}\mathbf{W}^{\mathsf{T}}\mathbf{s}$ into (4.18) gives

$$\dot{V} = \mathbf{s}^{\mathsf{T}}\bar{\mathbf{u}} - \mathbf{s}^{\mathsf{T}}\bar{\mathbf{M}}\boldsymbol{\lambda}\mathbf{s} + \tfrac{1}{2}\mathbf{s}^{\mathsf{T}}\left(\dot{\bar{\mathbf{M}}} - (\delta_\theta\dot{\theta} + \delta_\phi\dot{\phi})\mathbf{1}\right)\mathbf{s}. \qquad (4.19)$$

Take the integral of both sides of this equation from $t = 0$ to $t = T$ gives

$$\int_0^T \dot{V}\mathrm{d}t = \int_0^T \mathbf{s}^{\mathsf{T}}\bar{\mathbf{u}}\mathrm{d}t - \int_0^T \mathbf{s}^{\mathsf{T}}\bar{\mathbf{M}}\boldsymbol{\lambda}\mathbf{s}\mathrm{d}t + \tfrac{1}{2}\int_0^T \mathbf{s}^{\mathsf{T}}\left(\dot{\bar{\mathbf{M}}} - (\delta_\theta\dot{\theta} + \delta_\phi\dot{\phi})\mathbf{1}\right)\mathbf{s}\mathrm{d}t,$$

which results in

$$\int_0^T \mathbf{s}^{\mathsf{T}}\bar{\mathbf{u}}\mathrm{d}t = V(T) - V(0) + \int_0^T \mathbf{s}^{\mathsf{T}}\bar{\mathbf{M}}\boldsymbol{\lambda}\mathbf{s}\mathrm{d}t + \tfrac{1}{2}\int_0^T \mathbf{s}^{\mathsf{T}}\left((\delta_\theta\dot{\theta} + \delta_\phi\dot{\phi})\mathbf{1} - \dot{\bar{\mathbf{M}}}\right)\mathbf{s}\mathrm{d}t.$$

Since $V(T)$ is a nonnegative function by definition, $\bar{\mathbf{M}}\boldsymbol{\lambda} = \boldsymbol{\lambda}^{\mathsf{T}}\bar{\mathbf{M}}^{\mathsf{T}} > 0$ is a positive definite matrix, and $(\delta_\theta\dot{\theta} + \delta_\phi\dot{\phi})\mathbf{1} > \dot{\bar{\mathbf{M}}}$, it is known that

$$\int_0^T \mathbf{s}^{\mathsf{T}}\bar{\mathbf{u}}\mathrm{d}t \geq -V(0),$$

which demonstrates that the input-output mapping $\bar{\mathbf{u}} \mapsto \mathbf{s}$ is passive. □

Knowing that the input-output mapping $\bar{\mathbf{u}} \mapsto \mathbf{s}$ is passive, then using the Passivity Theorem, any ISP controller in a negative feedback interconnection with the system that possesses this input-output mapping ensures closed-loop input-output stability. In particular, an ISP negative feedback controller of the form

$$\bar{\mathbf{u}} = -\mathbf{K}_d\mathbf{s} \qquad (4.20)$$

is used, where $\mathbf{K}_d = \text{diag}\{K_{d,1}, K_{d,2}\}$ and $\mathbf{K}_d = \mathbf{K}_d^\mathsf{T} > 0$. In this case, the closed-loop equations of motion become

$$\mathbf{U} = \hat{\mathbf{U}} + \bar{\mathbf{u}} = \hat{\mathbf{M}}\ddot{\mathbf{q}}_{a,r} + \hat{\mathbf{B}}\dot{\mathbf{q}}_a + \hat{\mathbf{C}}\dot{q}_u + \hat{\mathbf{G}} - \tfrac{1}{2}(\delta_\theta\dot{\theta} + \delta_\phi\dot{\phi})\mathbf{s} - \mathbf{K}_d\mathbf{s}. \tag{4.21}$$

Figure 4.2a shows a block diagram of the concept of forming the close-loop system with control law (4.21). The plant is the practical crane model with equations of motion (2.6). The passive input-output stability mapping $\hat{\mathbf{u}} \mapsto \mathbf{s}$ is marked by the dotted block. An alternate block diagram is shown in Figure 4.2b, with the alternative plant defined by the error dynamics (4.16) and the adaptive law $\dot{\hat{\mathbf{a}}} = -\boldsymbol{\Gamma}^\mathsf{T}\mathbf{W}^\mathsf{T}\mathbf{s}$.

Theorem 6 (Stability of Adaptive Sliding-Mode Control)**.** *Consider the tower crane system described by the equations of motion in* (4.4)*. The control law of* (4.21) *ensures that* $\tilde{\phi} \to 0$*,* $\tilde{x}_a$ *is bounded, and* $\dot{\tilde{\mathbf{q}}}_a \to \mathbf{0}$ *as* $t \to \infty$*.*

Proof. Consider the nonnegative function in (4.17) and its derivative in (4.19). Substituting $\bar{\mathbf{u}} = -\mathbf{K}_d\mathbf{s}$ into (4.19) leads to the result of

$$\dot{V} = -\mathbf{s}^\mathsf{T}\left(\mathbf{K}_d + \bar{\mathbf{M}}\boldsymbol{\lambda}\right)\mathbf{s} - \tfrac{1}{2}\mathbf{s}^\mathsf{T}\left((\delta_\theta\dot{\theta} + \delta_\phi\dot{\phi})\mathbf{1} - \dot{\bar{\mathbf{M}}}\right)\mathbf{s} \leq 0.$$

Additionally, $V(T)$ nonnegative implies that $V(T) \leq V(0) < \infty$, which implies that V is bounded. This leads to the conclusion of $\{\mathbf{s}, \tilde{\mathbf{a}}\} \in \mathcal{L}_\infty$. Integrating $\dot{V}$ from $t = 0$ to $t = T$,

$$\left\| \sqrt{\mathbf{K}_d + \bar{\mathbf{M}}\boldsymbol{\lambda} + \tfrac{1}{2}\left((\delta_\theta\dot{\theta} + \delta_\phi\dot{\phi})\mathbf{1} - \dot{\bar{\mathbf{M}}}\right)}\,\mathbf{s} \right\|_{2T}^2 = V(0) - V(T),$$

$$\left\| \sqrt{\mathbf{K}_d}\,\mathbf{s} \right\|_{2T}^2 \leq V(0) - V(T) < \infty,$$

which implies that $\mathbf{s} \in \mathcal{L}_2 \cap \mathcal{L}_\infty$.

Since the sway angle is assumed bounded in the range $-\frac{\pi}{2} < \theta < \frac{\pi}{2}$, $q_u \in \mathcal{L}_\infty$. Rearranging the definition of $\mathbf{s}$ in (4.6) results in $\dot{\tilde{\mathbf{q}}}_a = -\boldsymbol{\lambda}\tilde{\mathbf{q}}_a - \boldsymbol{\alpha}q_u + \mathbf{s}$, which can

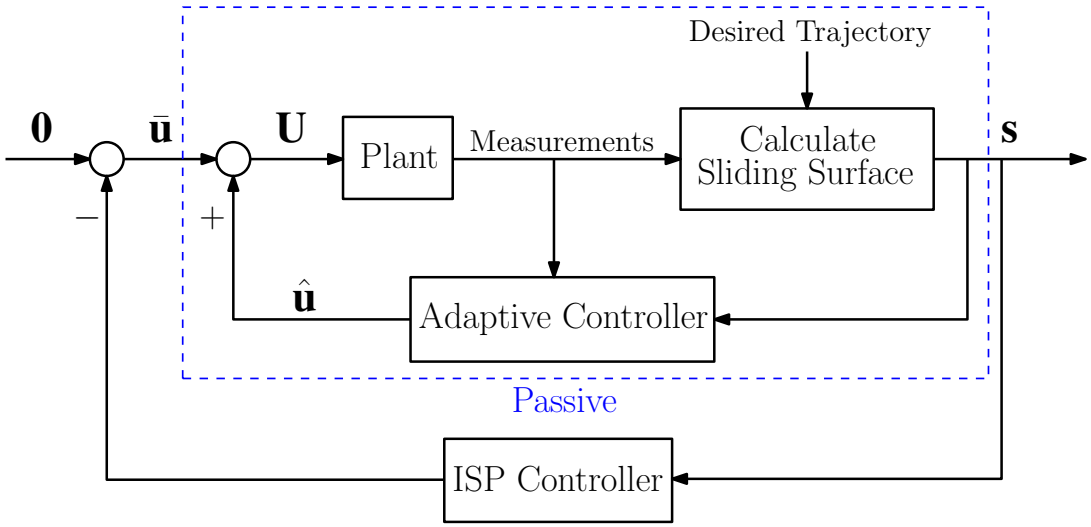

(a) Concept of implementing the adaptive feedback control system.

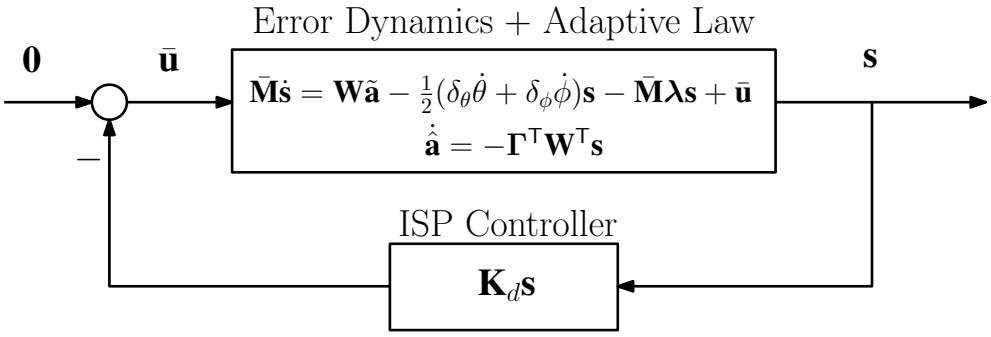

(b) Passive feedback control of the alternative plant.

Figure 4.2: Block diagrams with control law (4.21).

be expanded as

$$\dot{\tilde{x}}_a = -\lambda_1 \tilde{x}_a - \alpha_1 q_u + s_1 \tag{4.22}$$

$$\dot{\tilde{\phi}} = -\lambda_2 \tilde{\phi} + s_2. \tag{4.23}$$

Considering (4.22) as an asymptotically stable LTI system with $\mathcal{L}_\infty$-bounded inputs $\mathbf{s}$ and q_u,

$$\begin{cases} \dot{\tilde{x}}_a = -\lambda_1 \tilde{x}_a + (-\alpha_1 q_u + s_1) \\ y = \tilde{x}_a. \end{cases}$$

Employing Theorem 2, since $\{\mathbf{s}, q_u\} \in \mathcal{L}_\infty$, it is concluded that $(-\alpha_1 q_u + s_1) \in \mathcal{L}_\infty$, then $\tilde{x}_a \in \mathcal{L}_\infty$ and $\dot{\tilde{x}}_a \in \mathcal{L}_\infty$ [37, p. 270]. Although $x_a \to 0$ as $t \to \infty$ is not proved, it is shown that x_a stays bounded. Considering (4.23) as an asymptotically stable LTI system with $\mathcal{L}_2$-bounded input s_2 and employing Lemma 2, it is concluded that $\tilde{\phi} \in \mathcal{L}_2 \cap \mathcal{L}_\infty$, $\dot{\tilde{\phi}} \in \mathcal{L}_2$, and $\tilde{\phi} \to 0$ as $t \to \infty$ [37, p. 269]. Employing Barbalat's Lemma as in Lemma 1, since $\tilde{\mathbf{q}}_a \in \mathcal{L}_\infty$ has a finite limit as $t \to \infty$, and $\dot{\tilde{\mathbf{q}}}_a$ uniformly continuous, then $\dot{\tilde{\mathbf{q}}}_a \to \mathbf{0}$ as $t \to \infty$ [37, p. 657]. □

4.4 Adaptive Sliding-Mode Control in $\boldsymbol{\rho_a}$ Coordinates

In Section 4.3, the input-output mapping $\bar{\mathbf{u}} \mapsto \mathbf{s}$ is shown to be passive, where $\mathbf{s} = \dot{\tilde{\mathbf{q}}}_a + \boldsymbol{\lambda}\tilde{\mathbf{q}}_a + \boldsymbol{\alpha} q_u$. This section translates the dynamics from $\mathbf{q}_a$ coordinated into $\boldsymbol{\rho}_a$ coordinates, and elaborates the adaptive sliding-mode control method. The derivation of the theorems and proofs are similar to those presented in Section 4.3.1 and are therefore abbreviated. It is beneficial to work with the $\boldsymbol{\rho}_a$ coordinates for the purpose of payload position and velocity tracking. This can be seen as a step towards an extension of the sliding-mode control method to account for flexibility in the hoist cable using a μ-tip method similar to Chapter 3, without the restrictions small sway angle.

4.4.1 Reformulated Dynamics in $\boldsymbol{\rho}_a$ Coordinates

In Section 4.4, the adaptive sliding-mode control is applied to the dynamics in $\boldsymbol{\rho}_a$ coordinates, which is more practical than expressing the reformulated dynamics in the $\mathbf{q}_a$ coordinates, since the payload is to follow trajectories in $\boldsymbol{\rho}$. Another reformation of the dynamics is presented in this section to express the dynamics in these coordinates.

Without flexibility in the hoist cable, the payload position and velocity are redefined as

$$\boldsymbol{\rho} = \mathbf{J}_{ra}\mathbf{q}_a + \begin{bmatrix} -\sin\theta L \\ \cos\theta L \end{bmatrix} \quad \text{and} \quad \dot{\boldsymbol{\rho}} = \mathbf{J}_{ra}\dot{\mathbf{q}}_a + \mathbf{J}_{ru}\dot{q}_u, \tag{4.24}$$

where

$$\mathbf{J}_{ra} = \begin{bmatrix} 1 & r\sin\theta \\ 0 & -r\cos\theta \end{bmatrix}, \quad \text{and} \quad \mathbf{J}_{ru} = \begin{bmatrix} \cos\theta\,(r\phi - L) \\ \sin\theta\,(r\phi - L) \end{bmatrix}. \tag{4.25}$$

Consider the actuated payload position, velocity and acceleration defined as

$$\begin{aligned} \boldsymbol{\rho}_a &= \mathbf{J}_{ra,0}\mathbf{q}_a + \begin{bmatrix} 0 \\ L \end{bmatrix}, \\ \dot{\boldsymbol{\rho}}_a &= \mathbf{J}_{ra,0}\dot{\mathbf{q}}_a, \\ \ddot{\boldsymbol{\rho}}_a &= \mathbf{J}_{ra,0}\ddot{\mathbf{q}}_a, \end{aligned}$$

where

$$\mathbf{J}_{ra,0} = \mathbf{J}_{ra}|_{\theta=0} = \mathbf{J}_{ra}(\theta = 0) = \begin{bmatrix} 1 & 0 \\ 0 & -r \end{bmatrix}$$

transforms the actuated states $\mathbf{q}_a$ into $\boldsymbol{\rho}_a$ discarding the sway angle θ. The physical significance of ρ_a, $\dot{\rho}_a$, and $\ddot{\rho}_a$ can be seen as the desired payload trajectory at the equilibrium point that $\theta = 0$. Substituting $\dot{\mathbf{q}}_a = \mathbf{J}_{ra,0}^{-1}\dot{\boldsymbol{\rho}}_a$ and $\ddot{\mathbf{q}}_a = \mathbf{J}_{ra,0}^{-1}\ddot{\boldsymbol{\rho}}_a$ into (4.4), and premultiplying by $\mathbf{J}_{ra,0}^{-\mathsf{T}}$ gives the reformulated equations of motion in the $\boldsymbol{\rho}_a$ coordinates

$$\bar{\mathbf{M}}_{\rho\rho}\ddot{\boldsymbol{\rho}}_a + \bar{\mathbf{B}}_{\rho\rho}\dot{\boldsymbol{\rho}}_a + \bar{\mathbf{C}}_{\rho}\dot{q}_u + \bar{\mathbf{G}}_{\rho} = \mathbf{U}_{\rho}, \tag{4.26}$$

where $\bar{\mathbf{M}}_{\rho\rho} = \mathbf{J}_{ra,0}^{-\mathsf{T}}\bar{\mathbf{M}}\mathbf{J}_{ra,0}^{-1}$, $\bar{\mathbf{B}}_{\rho\rho} = \mathbf{J}_{ra,0}^{-\mathsf{T}}\bar{\mathbf{B}}\mathbf{J}_{ra,0}^{-1}$, $\bar{\mathbf{C}}_{\rho} = \mathbf{J}_{ra,0}^{-\mathsf{T}}\bar{\mathbf{C}}$, $\bar{\mathbf{G}}_{\rho} = \mathbf{J}_{ra,0}^{-\mathsf{T}}\bar{\mathbf{G}}$, and $\bar{\mathbf{U}}_{\rho} = \mathbf{J}_{ra,0}^{-\mathsf{T}}\bar{\mathbf{U}}$.

4.4.2 Sliding Mode and Sliding Surface

Similar to Section 4.3.1, the sliding surface dynamics are

$$\dot{\mathbf{s}}_{\rho} + \boldsymbol{\lambda}_{\rho}\mathbf{s}_{\rho} = \mathbf{0}, \tag{4.27}$$

where $\mathbf{s}_{\rho} \in \mathbb{R}^2$ and $\boldsymbol{\lambda}_{\rho} = \boldsymbol{\lambda}_{\rho}^{\mathsf{T}} > 0$. The sliding surface is defined as

$$\mathbf{s}_{\rho} = \dot{\tilde{\boldsymbol{\rho}}}_a + \boldsymbol{\lambda}_{\rho}\tilde{\boldsymbol{\rho}}_a + \boldsymbol{\alpha}_{\rho}q_u, \tag{4.28}$$

where $\dot{\tilde{\boldsymbol{\rho}}}_a = \dot{\boldsymbol{\rho}}_a - \dot{\boldsymbol{\rho}}_{a,d}$, and $\tilde{\boldsymbol{\rho}}_a = \boldsymbol{\rho}_a - \boldsymbol{\rho}_{a,d}$ are tracking errors of the payload velocity and position, and $\boldsymbol{\lambda}_{\rho} = \mathrm{diag}(\lambda_{\rho,1}, \lambda_{\rho,2})$, $\boldsymbol{\alpha}_{\rho} = \begin{bmatrix}\alpha_{\rho} & 0\end{bmatrix}^{\mathsf{T}}$ are constant control parameters. The time derivative of the sliding surface is

$$\dot{\mathbf{s}}_{\rho} = \frac{\mathrm{d}}{\mathrm{d}t}\mathbf{s}_{\rho} = \ddot{\tilde{\boldsymbol{\rho}}}_a + \boldsymbol{\lambda}_{\rho}\dot{\tilde{\boldsymbol{\rho}}}_a + \boldsymbol{\alpha}_{\rho}\dot{q}_u, \tag{4.29}$$

where $\ddot{\tilde{\boldsymbol{\rho}}}_a = \ddot{\boldsymbol{\rho}}_a - \ddot{\boldsymbol{\rho}}_{a,d}$. From (4.28) and (4.29), the dynamics of the sliding surface are defined as

$$\dot{\mathbf{s}}_{\rho} + \boldsymbol{\lambda}_{\rho}\mathbf{s}_{\rho} = \ddot{\tilde{\boldsymbol{\rho}}}_a + 2\boldsymbol{\lambda}_{\rho}\dot{\tilde{\boldsymbol{\rho}}}_a + \boldsymbol{\lambda}_{\rho}^{\mathsf{T}}\boldsymbol{\lambda}_{\rho}\tilde{\boldsymbol{\rho}}_a + \boldsymbol{\alpha}_{\rho}\dot{q}_u + \boldsymbol{\lambda}_{\rho}\boldsymbol{\alpha}_{\rho}q_u. \tag{4.30}$$

Based on (4.30), we define the reference acceleration

$$\begin{aligned}\ddot{\boldsymbol{\rho}}_{a,r} &= \ddot{\boldsymbol{\rho}}_a - (\dot{\mathbf{s}}_{\rho} + \boldsymbol{\lambda}_{\rho}\mathbf{s}_{\rho}) \\ &= \ddot{\boldsymbol{\rho}}_{a,d} - 2\boldsymbol{\lambda}_{\rho}\dot{\tilde{\boldsymbol{\rho}}}_a - \boldsymbol{\lambda}_{\rho}^{\mathsf{T}}\boldsymbol{\lambda}_{\rho}\tilde{\boldsymbol{\rho}}_a - \boldsymbol{\alpha}_{\rho}\dot{q}_u - \boldsymbol{\lambda}_{\rho}\boldsymbol{\alpha}_{\rho}q_u,\end{aligned} \tag{4.31}$$

which will be used as the reference payload acceleration for the adaptive control that guides the system dynamics towards the designed sliding surface. It is worth noting that $\ddot{\boldsymbol{\rho}}_a - \ddot{\boldsymbol{\rho}}_{a,r} = \dot{\mathbf{s}}_{\rho} + \boldsymbol{\lambda}_{\rho}\mathbf{s}_{\rho}$ by the definition of (4.31).

4.4.3 Adaptive Control

Define the input

$$\mathbf{U}_\rho = \mathbf{W}_\rho \mathbf{a}_\rho = \bar{\mathbf{M}}_{\rho\rho}\ddot{\boldsymbol{\rho}}_{a,r} + \bar{\mathbf{B}}_{\rho\rho}\dot{\boldsymbol{\rho}}_a + \bar{\mathbf{C}}_\rho \dot{q}_u + \bar{\mathbf{G}}_\rho,$$

where $\mathbf{W}_\rho$ is the regressor, and $\mathbf{a}_\rho$ is the matrix containing the true mass and nonlinear terms in the reformulated dynamics (4.26) capturing the true dynamics of the system with the reference payload acceleration. These matrices are given by

$$\mathbf{W}_\rho = \begin{bmatrix} \ddot{\boldsymbol{\rho}}_{a,r}^\mathsf{T} & \mathbf{0}_{1\times 2} & \dot{\boldsymbol{\rho}}_a^\mathsf{T} & \mathbf{0}_{1\times 2} & \dot{q}_u & 0 & 1 & 0 \\ \mathbf{0}_{1\times 2} & \ddot{\boldsymbol{\rho}}_{a,r}^\mathsf{T} & \mathbf{0}_{1\times 2} & \dot{\boldsymbol{\rho}}_a^\mathsf{T} & 0 & \dot{q}_u & 0 & 1 \end{bmatrix},$$

$$\mathbf{a}_\rho = \begin{bmatrix} \bar{\mathbf{m}}_{\rho\rho}^\mathsf{T} & \bar{\mathbf{b}}_{\rho\rho}^\mathsf{T} & \bar{\mathbf{c}}_\rho^\mathsf{T} & \bar{\mathbf{g}}_\rho^\mathsf{T} \end{bmatrix}^\mathsf{T}$$

where the entries of $\mathbf{a}_\rho$ are the vectorized matrices of the reformulated dynamics (4.26), $\bar{\mathbf{m}}_{\rho\rho} = \begin{bmatrix} \bar{M}_{\rho\rho,11} & \bar{M}_{\rho\rho,12} & \bar{M}_{\rho\rho,21} & \bar{M}_{\rho\rho,22} \end{bmatrix}^\mathsf{T}$, $\bar{\mathbf{b}}_{\rho\rho} = \begin{bmatrix} \bar{B}_{\rho\rho,11} & \bar{B}_{\rho\rho,12} & \bar{B}_{\rho\rho,21} & \bar{B}_{\rho\rho,22} \end{bmatrix}^\mathsf{T}$, $\bar{\mathbf{c}}_\rho = \begin{bmatrix} \bar{C}_{\rho,1} & \bar{C}_{\rho,2} \end{bmatrix}^\mathsf{T}$, and $\bar{\mathbf{g}}_\rho = \begin{bmatrix} \bar{G}_{\rho,1} & \bar{G}_{\rho,2} \end{bmatrix}^\mathsf{T}$. Note that we also assume $\mathbf{W}_\rho$ perfectly measures the states of the system and being perfectly known.

The time derivative of $\bar{\mathbf{M}}_{\rho\rho}(\phi,\theta)$ can be written as

$$\dot{\bar{\mathbf{M}}}_{\rho\rho} = \frac{\mathrm{d}}{\mathrm{d}t}\bar{\mathbf{M}}_{\rho\rho}(\phi,\theta) = \left.\frac{\partial \bar{\mathbf{M}}_{\rho\rho}}{\partial \theta}\right|_{\phi,\theta}\dot{\theta} + \left.\frac{\partial \bar{\mathbf{M}}_{\rho\rho}}{\partial \phi}\right|_{\phi,\theta}\dot{\phi}, \tag{4.32}$$

where $\frac{\partial \bar{\mathbf{M}}_{\rho\rho}}{\partial \theta} = \frac{\partial \bar{\mathbf{M}}_{\rho\rho}}{\partial \theta}^\mathsf{T}$ and $\frac{\partial \bar{\mathbf{M}}_{\rho\rho}}{\partial \phi} = \frac{\partial \bar{\mathbf{M}}_{\rho\rho}}{\partial \phi}^\mathsf{T}$. Upper bounds on the eigenvalues of $\frac{\partial \bar{\mathbf{M}}_{\rho\rho}}{\partial \theta}$ and $\frac{\partial \bar{\mathbf{M}}_{\rho\rho}}{\partial \phi}$ are given by the constants $\delta_{\theta,\rho}$ and $\delta_{\phi,\rho}$, respectively. These upper bounds can be equivalently described by the matrix inequalities

$$\frac{\partial \bar{\mathbf{M}}_{\rho\rho}}{\partial \theta} < \delta_{\theta,\rho}\mathbf{1}, \tag{4.33}$$

$$\frac{\partial \bar{\mathbf{M}}_{\rho\rho}}{\partial \phi} < \delta_{\phi,\rho}\mathbf{1}. \tag{4.34}$$

Adding the matrix inequalities in (4.33) and (4.34), and substituting the result

into(4.32) yields

$$\dot{\bar{\mathbf{M}}}_{\rho\rho} < (\delta_{\theta,\rho}\dot{\theta} + \delta_{\phi,\rho}\dot{\phi})\mathbf{1}.$$

Note that $\bar{\mathbf{M}}_{\rho\rho} = \mathbf{J}_{ra,0}^{-\mathsf{T}}\bar{\mathbf{M}}\mathbf{J}_{ra,0}^{-1}$ and $\mathbf{J}_{ra,0}$ is a constant matrix,

$$\dot{\bar{\mathbf{M}}}_{\rho\rho} = \mathbf{J}_{ra,0}^{-\mathsf{T}}\left(\left.\frac{\partial\bar{\mathbf{M}}}{\partial\theta}\right|_{\phi,\theta}\dot{\theta} + \left.\frac{\partial\bar{\mathbf{M}}}{\partial\phi}\right|_{\phi,\theta}\dot{\phi}\right)\mathbf{J}_{ra,0}^{-1} < (\delta_\theta\dot{\theta} + \delta_\phi\dot{\phi})\mathbf{J}_{ra,0}^{-\mathsf{T}}\mathbf{J}_{ra,0}^{-1},$$

which can be seen as a connection between $(\delta_{\phi,\rho}, \delta_{\theta,\rho})$ and $(\delta_\phi, \delta_\theta)$. The adaptive feedforward control input is designed as

$$\begin{aligned}\hat{\mathbf{U}}_\rho &= \mathbf{W}_\rho\hat{\mathbf{a}}_\rho - \tfrac{1}{2}\left(\delta_{\theta,\rho}\dot{\theta} + \delta_{\phi,\rho}\dot{\phi}\right)\mathbf{s}_\rho \\ &= \hat{\mathbf{M}}_{\rho\rho}\ddot{\boldsymbol{\rho}}_{a,r} + \hat{\mathbf{B}}_{\rho\rho}\dot{\boldsymbol{\rho}}_a + \hat{\mathbf{C}}_\rho\dot{q}_u + \hat{\mathbf{G}}_\rho - \tfrac{1}{2}\left(\delta_{\theta,\rho}\dot{\theta} + \delta_{\phi,\rho}\dot{\phi}\right)\mathbf{s}_\rho, \qquad (4.35)\end{aligned}$$

$$\hat{\mathbf{a}}_\rho = \begin{bmatrix}\hat{\mathbf{m}}_{\rho\rho}^{\mathsf{T}} & \hat{\mathbf{b}}_{\rho\rho}^{\mathsf{T}} & \hat{\mathbf{c}}_\rho^{\mathsf{T}} & \hat{\mathbf{g}}_\rho^{\mathsf{T}}\end{bmatrix}^{\mathsf{T}},$$

where $\hat{\mathbf{m}}_{\rho\rho} = \begin{bmatrix}\hat{M}_{\rho\rho,11} & \hat{M}_{\rho\rho,12} & \hat{M}_{\rho\rho,21} & \hat{M}_{\rho\rho,22}\end{bmatrix}^{\mathsf{T}}$, $\hat{\mathbf{b}}_{\rho\rho} = \begin{bmatrix}\hat{B}_{\rho\rho,11} & \hat{B}_{\rho\rho,12} & \hat{B}_{\rho\rho,21} & \hat{B}_{\rho\rho,22}\end{bmatrix}^{\mathsf{T}}$, $\hat{\mathbf{c}}_\rho = \begin{bmatrix}\hat{C}_{\rho,1} & \hat{C}_{\rho,2}\end{bmatrix}^{\mathsf{T}}$, and $\hat{\mathbf{g}}_\rho = \begin{bmatrix}\hat{G}_{\rho,1} & \hat{G}_{\rho,2}\end{bmatrix}^{\mathsf{T}}$ are estimates of the true matrices $\bar{\mathbf{M}}_{\rho\rho}$, $\bar{\mathbf{B}}_{\rho\rho}$, $\bar{\mathbf{C}}_\rho$, and $\bar{\mathbf{G}}_\rho$.

Let $\mathbf{U}_\rho = \hat{\mathbf{U}}_\rho + \bar{\mathbf{u}}_\rho$, where $\bar{\mathbf{u}}_\rho$ is a feedback control input to be designed. Substituting (4.35) into (4.26) gives

$$\bar{\mathbf{M}}_{\rho\rho}\ddot{\boldsymbol{\rho}}_a = \hat{\mathbf{M}}_{\rho\rho}\ddot{\boldsymbol{\rho}}_{a,r} + \tilde{\mathbf{B}}_{\rho\rho}\dot{\boldsymbol{\rho}}_a + \tilde{\mathbf{C}}_\rho\dot{q}_u + \tilde{\mathbf{G}}_\rho - \tfrac{1}{2}\left(\delta_{\theta,\rho}\dot{\theta} + \delta_{\phi,\rho}\dot{\phi}\right)\mathbf{s}_\rho + \bar{\mathbf{u}}_\rho,$$

where $\tilde{\mathbf{B}}_{\rho\rho} = \hat{\mathbf{B}}_{\rho\rho} - \bar{\mathbf{B}}_{\rho\rho}$, $\tilde{\mathbf{C}}_\rho = \hat{\mathbf{C}}_\rho - \bar{\mathbf{C}}_\rho$, $\tilde{\mathbf{G}}_\rho = \hat{\mathbf{G}}_\rho - \bar{\mathbf{G}}_\rho$. Subtracting $\bar{\mathbf{M}}_{\rho\rho}\ddot{\boldsymbol{\rho}}_{a,r}$ from both sides gives

$$\bar{\mathbf{M}}_{\rho\rho}\left(\ddot{\boldsymbol{\rho}}_a - \ddot{\boldsymbol{\rho}}_{a,r}\right) = \tilde{\mathbf{M}}_{\rho\rho}\ddot{\boldsymbol{\rho}}_{a,r} + \tilde{\mathbf{B}}_{\rho\rho}\dot{\boldsymbol{\rho}}_a + \tilde{\mathbf{C}}_\rho\dot{q}_u + \tilde{\mathbf{G}}_\rho - \tfrac{1}{2}\left(\delta_{\theta,\rho}\dot{\theta} + \delta_{\phi,\rho}\dot{\phi}\right)\mathbf{s}_\rho + \bar{\mathbf{u}}_\rho,$$

where $\tilde{\mathbf{M}}_{\rho\rho} = \hat{\mathbf{M}}_{\rho\rho} - \bar{\mathbf{M}}_{\rho\rho}$. Substituting $\ddot{\boldsymbol{\rho}}_a - \ddot{\boldsymbol{\rho}}_{a,r} = \dot{\mathbf{s}}_\rho + \boldsymbol{\lambda}_\rho\mathbf{s}_\rho$ given by (4.31) yields

the error dynamics

$$\bar{\mathbf{M}}_{\rho\rho}\left(\dot{\mathbf{s}}_\rho + \boldsymbol{\lambda}_\rho \mathbf{s}_\rho\right) = \tilde{\mathbf{M}}_{\rho\rho}\ddot{\boldsymbol{\rho}}_{a,r} + \tilde{\mathbf{B}}_{\rho\rho}\dot{\boldsymbol{\rho}}_a + \tilde{\mathbf{C}}_\rho \dot{q}_u + \tilde{\mathbf{G}}_\rho - \tfrac{1}{2}\left(\delta_{\theta,\rho}\dot{\theta} + \delta_{\phi,\rho}\dot{\phi}\right)\mathbf{s}_\rho + \bar{\mathbf{u}}_\rho,$$

which can be rearranged as

$$\bar{\mathbf{M}}_{\rho\rho}\dot{\mathbf{s}}_\rho = \tilde{\mathbf{M}}_{\rho\rho}\ddot{\boldsymbol{\rho}}_a + \tilde{\mathbf{B}}_{\rho\rho}\dot{\boldsymbol{\rho}}_a + \tilde{\mathbf{C}}_\rho \dot{q}_u + \tilde{\mathbf{G}}_\rho - \tfrac{1}{2}\left(\delta_{\theta,\rho}\dot{\theta} + \delta_{\phi,\rho}\dot{\phi}\right)\mathbf{s}_\rho - \bar{\mathbf{M}}_{\rho\rho}\boldsymbol{\lambda}_\rho \mathbf{s}_\rho + \bar{\mathbf{u}}_\rho. \quad (4.36)$$

Notice that

$$\mathbf{W}_\rho \tilde{\mathbf{a}}_\rho = \mathbf{W}_\rho\left(\hat{\mathbf{a}}_\rho - \mathbf{a}_\rho\right) = \tilde{\mathbf{M}}_{\rho\rho}\ddot{\boldsymbol{\rho}}_{a,r} + \tilde{\mathbf{B}}_{\rho\rho}\dot{\boldsymbol{\rho}}_a + \tilde{\mathbf{C}}_\rho \dot{q}_u + \tilde{\mathbf{G}}_\rho. \quad (4.37)$$

and therefore (4.36) can be rewritten as

$$\bar{\mathbf{M}}_{\rho\rho}\dot{\mathbf{s}}_\rho = \mathbf{W}_\rho \tilde{\mathbf{a}}_\rho - \tfrac{1}{2}\left(\delta_{\theta,\rho}\dot{\theta} + \delta_{\phi,\rho}\dot{\phi}\right)\mathbf{s}_\rho - \bar{\mathbf{M}}_{\rho\rho}\boldsymbol{\lambda}_\rho \mathbf{s}_\rho + \bar{\mathbf{u}}_\rho. \quad (4.38)$$

4.4.4 Passivity and Closed-Loop Stability Analysis

Theorem 7 (Passive Input-Output Map $\bar{\mathbf{u}}_\rho \mapsto \mathbf{s}_\rho$)**.** *Consider the system with error dynamics defined in* (4.38)*, where the term* $\hat{\mathbf{U}}_\rho$ *is updated based on the adaptive law* $\dot{\hat{\mathbf{a}}}_\rho = -\boldsymbol{\Gamma}_\rho^{\mathsf{T}}\mathbf{W}_\rho^{\mathsf{T}}\mathbf{s}_\rho$*, where* $\boldsymbol{\Gamma}_\rho = \boldsymbol{\Gamma}_\rho^{\mathsf{T}} > 0$*, and it is assumed that* $\mathbf{a}_\rho$ *is approximately constant. The input-output mapping* $\bar{\mathbf{u}}_\rho \mapsto \mathbf{s}_\rho$ *is passive.*

Proof. Consider the nonnegative function

$$V_\rho = \tfrac{1}{2}\mathbf{s}_\rho^{\mathsf{T}}\bar{\mathbf{M}}_{\rho\rho}\mathbf{s}_\rho + \tfrac{1}{2}\tilde{\mathbf{a}}_\rho^{\mathsf{T}}\boldsymbol{\Gamma}_\rho^{-1}\tilde{\mathbf{a}}_\rho. \quad (4.39)$$

Taking the time derivative of (4.39) and substituting in (4.38) gives

$$\begin{aligned}\dot{V}_\rho &= \mathbf{s}_\rho^\mathsf{T}\bar{\mathbf{M}}_{\rho\rho}\dot{\mathbf{s}}_\rho + \tfrac{1}{2}\mathbf{s}_\rho^\mathsf{T}\dot{\bar{\mathbf{M}}}_{\rho\rho}\mathbf{s}_\rho + \dot{\tilde{\mathbf{a}}}_\rho^\mathsf{T}\boldsymbol{\Gamma}_\rho^{-1}\tilde{\mathbf{a}}_\rho \\ &= \mathbf{s}_\rho^\mathsf{T}\left(\mathbf{W}_\rho\tilde{\mathbf{a}}_\rho - \tfrac{1}{2}\left(\delta_{\theta,\rho}\dot{\theta} + \delta_{\phi,\rho}\dot{\phi}\right)\mathbf{s}_\rho - \bar{\mathbf{M}}_{\rho\rho}\boldsymbol{\lambda}_\rho\mathbf{s}_\rho + \bar{\mathbf{u}}_\rho\right) + \tfrac{1}{2}\mathbf{s}_\rho^\mathsf{T}\dot{\bar{\mathbf{M}}}_{\rho\rho}\mathbf{s}_\rho + \dot{\tilde{\mathbf{a}}}_\rho^\mathsf{T}\boldsymbol{\Gamma}_\rho^{-1}\tilde{\mathbf{a}}_\rho \\ &= \mathbf{s}_\rho^\mathsf{T}\bar{\mathbf{u}}_\rho - \mathbf{s}_\rho^\mathsf{T}\bar{\mathbf{M}}_{\rho\rho}\boldsymbol{\lambda}_\rho\mathbf{s}_\rho + \tfrac{1}{2}\mathbf{s}_\rho^\mathsf{T}\left(\dot{\bar{\mathbf{M}}}_{\rho\rho} - \left(\delta_{\theta,\rho}\dot{\theta} + \delta_{\phi,\rho}\dot{\phi}\right)\mathbf{1}\right)\mathbf{s}_\rho + \left(\mathbf{s}_\rho^\mathsf{T}\mathbf{W}_\rho + \dot{\tilde{\mathbf{a}}}_\rho^\mathsf{T}\boldsymbol{\Gamma}_\rho^{-1}\right)\tilde{\mathbf{a}}_\rho.\end{aligned} \tag{4.40}$$

Since it is assumed that $\mathbf{a}_\rho$ is constant, $\dot{\tilde{\mathbf{a}}}_\rho = \dot{\hat{\mathbf{a}}}_\rho$ and $\mathbf{s}_\rho^\mathsf{T}\mathbf{W}_\rho + \dot{\tilde{\mathbf{a}}}_\rho^\mathsf{T}\boldsymbol{\Gamma}_\rho^{-1} = \mathbf{s}_\rho^\mathsf{T}\mathbf{W}_\rho + \dot{\hat{\mathbf{a}}}_\rho^\mathsf{T}\boldsymbol{\Gamma}_\rho^{-1}$. Substituting in the adaptive law $\dot{\hat{\mathbf{a}}}_\rho = -\boldsymbol{\Gamma}_\rho^\mathsf{T}\mathbf{W}_\rho^\mathsf{T}\mathbf{s}_\rho$ into (4.40) gives

$$\dot{V}_\rho = \mathbf{s}_\rho^\mathsf{T}\bar{\mathbf{u}}_\rho - \mathbf{s}_\rho^\mathsf{T}\bar{\mathbf{M}}_{\rho\rho}\boldsymbol{\lambda}_\rho\mathbf{s}_\rho + \tfrac{1}{2}\mathbf{s}_\rho^\mathsf{T}\left(\dot{\bar{\mathbf{M}}}_{\rho\rho} - \left(\delta_{\theta,\rho}\dot{\theta} + \delta_{\phi,\rho}\dot{\phi}\right)\mathbf{1}\right)\mathbf{s}_\rho. \tag{4.41}$$

Take the integral of both sides of this equation from $t = 0$ to $t = T$ gives

$$\int_0^T \dot{V}_\rho \mathrm{d}t = \int_0^T \mathbf{s}_\rho^\mathsf{T}\bar{\mathbf{u}}_\rho \mathrm{d}t - \int_0^T \mathbf{s}_\rho^\mathsf{T}\bar{\mathbf{M}}_{\rho\rho}\boldsymbol{\lambda}\mathbf{s}_\rho \mathrm{d}t + \tfrac{1}{2}\int_0^T \mathbf{s}_\rho^\mathsf{T}\left(\dot{\bar{\mathbf{M}}}_{\rho\rho} - \left(\delta_{\theta,\rho}\dot{\theta} + \delta_{\phi,\rho}\dot{\phi}\right)\mathbf{1}\right)\mathbf{s}_\rho \mathrm{d}t,$$

which results in

$$\int_0^T \mathbf{s}_\rho^\mathsf{T}\bar{\mathbf{u}}_\rho \mathrm{d}t = V_\rho(T) - V_\rho(0) + \int_0^T \mathbf{s}_\rho^\mathsf{T}\bar{\mathbf{M}}_{\rho\rho}\boldsymbol{\lambda}_\rho\mathbf{s}_\rho \mathrm{d}t + \tfrac{1}{2}\int_0^T \mathbf{s}_\rho^\mathsf{T}\left(\left(\delta_{\theta,\rho}\dot{\theta} + \delta_{\phi,\rho}\dot{\phi}\right)\mathbf{1} - \dot{\bar{\mathbf{M}}}_{\rho\rho}\right)\mathbf{s}_\rho \mathrm{d}t.$$

Since $V_\rho(T)$ is a nonnegative function by definition, $\bar{\mathbf{M}}_{\rho\rho}\boldsymbol{\lambda}_\rho = \boldsymbol{\lambda}_\rho^\mathsf{T}\bar{\mathbf{M}}_{\rho\rho}^\mathsf{T} > 0$ is a positive definite matrix, and $\left(\delta_{\theta,\rho}\dot{\theta} + \delta_{\phi,\rho}\dot{\phi}\right)\mathbf{1} > \dot{\bar{\mathbf{M}}}_{\rho\rho}$, it is known that

$$\int_0^T \mathbf{s}_\rho^\mathsf{T}\bar{\mathbf{u}}_\rho \mathrm{d}t \geq -V_\rho(0)$$

which demonstrates that the input-output mapping $\bar{\mathbf{u}}_\rho \mapsto \mathbf{s}_\rho$ is passive. □

Knowing that the input-output mapping $\bar{\mathbf{u}}_\rho \mapsto \mathbf{s}_\rho$ is passive, then using the Passivity Theorem, any ISP controller in a negative feedback interconnection with

the system that possesses this input-output mapping ensures closed-loop input-output stability. In particular, an ISP negative feedback controller of the form

$$\bar{\mathbf{u}}_\rho = -\mathbf{K}_{d,\rho}\mathbf{s}_\rho \tag{4.42}$$

is used, where $\mathbf{K}_{d,\rho} = \mathbf{K}_{d,\rho}^\mathsf{T} > 0$. In this case, the closed-loop equations of motion become

$$\mathbf{U}_\rho = \hat{\mathbf{U}}_\rho + \bar{\mathbf{u}}_\rho = \hat{\mathbf{M}}_{\rho\rho}\ddot{\boldsymbol{\rho}}_{a,r} + \hat{\mathbf{B}}_{\rho\rho}\dot{\boldsymbol{\rho}}_a + \hat{\mathbf{C}}_\rho \dot{q}_u + \hat{\mathbf{G}}_\rho - \tfrac{1}{2}\left(\delta_{\theta,\rho}\dot{\theta} + \delta_{\phi,\rho}\dot{\phi}\right)\mathbf{s}_\rho - \mathbf{K}_{d,\rho}\mathbf{s}_\rho. \tag{4.43}$$

Theorem 8 (Stability of Adaptive Sliding-Mode Control in $\boldsymbol{\rho}$ Coordinates)**.** *Consider the tower crane system described by the equations of motion in* (4.26)*. The control law of* (4.43) *ensures that* $\tilde{\rho}_{a,1}$ *is bounded,* $\tilde{\rho}_{a,2} \to 0$*, and* $\dot{\tilde{\boldsymbol{\rho}}}_a \to \mathbf{0}$ *as* $t \to \infty$*.*

Proof. Consider the nonnegative function in (4.39) and its derivative in (4.41). Substituting $\bar{\mathbf{u}} = -\mathbf{K}_{d,\rho}\mathbf{s}_\rho$ into (4.41) leads to the result of

$$\dot{V}_\rho = -\mathbf{s}_\rho^\mathsf{T}\left(\mathbf{K}_{d,\rho} + \bar{\mathbf{M}}_{\rho\rho}\boldsymbol{\lambda}_\rho\right)\mathbf{s}_\rho - \tfrac{1}{2}\mathbf{s}_\rho^\mathsf{T}\left((\delta_{\theta,\rho}\dot{\theta} + \delta_{\phi,\rho}\dot{\phi})\mathbf{1} - \dot{\bar{\mathbf{M}}}_{\rho\rho}\right)\mathbf{s}_\rho \leq 0.$$

Additionally, $V_\rho(T)$ nonnegative implies that $V_\rho(T) \leq V_\rho(0) < \infty$, which implies that V_ρ is bounded. This leads to the conclusion of $\{\mathbf{s}_\rho, \tilde{\mathbf{a}}_\rho\} \in \mathcal{L}_\infty$. Integrating $\dot{V}_\rho$ from $t = 0$ to $t = T$,

$$\left\| \sqrt{\mathbf{K}_{d,\rho} + \bar{\mathbf{M}}_{\rho\rho}\boldsymbol{\lambda}_\rho + \tfrac{1}{2}\left((\delta_{\theta,\rho}\dot{\theta} + \delta_{\phi,\rho}\dot{\phi})\mathbf{1} - \dot{\bar{\mathbf{M}}}_{\rho\rho}\right)}\,\mathbf{s}_\rho \right\|_{2T}^2 = V_\rho(0) - V_\rho(T),$$

$$\left\| \sqrt{\mathbf{K}_{d,\rho}}\,\mathbf{s}_\rho \right\|_{2T}^2 \leq V_\rho(0) - V_\rho(T) < \infty,$$

which implies that $\mathbf{s}_\rho \in \mathcal{L}_2 \cap \mathcal{L}_\infty$.

Since the sway angle is assumed bounded in the range $-\frac{\pi}{2} < \theta < \frac{\pi}{2}$, $q_u \in \mathcal{L}_\infty$. Rearranging the definition of $\mathbf{s}_\rho$ in (4.28) results in $\dot{\tilde{\boldsymbol{\rho}}}_a = -\boldsymbol{\lambda}_\rho\tilde{\boldsymbol{\rho}}_a - \boldsymbol{\alpha}_\rho q_u + \mathbf{s}_\rho$, which

can be expanded as

$$\dot{\tilde{\rho}}_{a,1} = -\lambda_{\rho,1}\tilde{\rho}_{a,1} - \alpha_{\rho,1}q_u + s_{\rho,1} \tag{4.44}$$

$$\dot{\tilde{\rho}}_{a,2} = -\lambda_{\rho,2}\tilde{\rho}_{a,2} + s_{\rho,2}. \tag{4.45}$$

Considering (4.44) as an asymptotically stable LTI system with $\mathcal{L}_\infty$-bounded inputs $\mathbf{s}_\rho$ and q_u,

$$\begin{cases} \dot{\tilde{\rho}}_{a,1} = -\lambda_{\rho,1}\tilde{\rho}_{a,1} + (-\alpha_{\rho,1}q_u + s_{\rho,1}) \\ y = \tilde{\rho}_{a,1}. \end{cases}$$

Employing Theorem 2, since $\{\mathbf{s}_\rho, q_u\} \in \mathcal{L}_\infty$, it is concluded that $(-\alpha_{\rho,1}q_u + s_{\rho,1}) \in \mathcal{L}_\infty$, then $\tilde{\rho}_{a,1} \in \mathcal{L}_\infty$ and $\dot{\tilde{\rho}}_{a,1} \in \mathcal{L}_\infty$ [37, p. 270]. Although $\rho_{a,1} \to 0$ as $t \to \infty$ is not proved, it is shown that $\rho_{a,1}$ stays bounded. Considering (4.45) as an asymptotically stable LTI system with $\mathcal{L}_2$-bounded input $s_{\rho,2}$ and employing Lemma 2, it is concluded that $\tilde{\rho}_{a,2} \in \mathcal{L}_2 \cap \mathcal{L}_\infty$, $\dot{\tilde{\rho}}_{a,2} \in \mathcal{L}_2$, and $\tilde{\rho}_{a,2} \to 0$ as $t \to \infty$ [37, p. 269]. Employing Barbalat's Lemma as in Lemma 1, since $\tilde{\boldsymbol{\rho}}_a \in \mathcal{L}_\infty$ has a finite limit as $t \to \infty$, and $\dot{\tilde{\boldsymbol{\rho}}}_a$ uniformly continuous, then $\dot{\tilde{\boldsymbol{\rho}}}_a \to \mathbf{0}$ as $t \to \infty$ [37, p. 657]. □

4.5 Numerical Example

In this section, numerical simulation results of the adaptive sliding-mode control method in Sections 4.3 and 4.4 are presented using the control laws in (4.21) and (4.43).

The same system setup as in Section 3.4 is used, and the cable is considered rigid, where the stiffness matrix $\mathbf{K} = \mathbf{0}$. Recall the numerical values chosen in Section 3.4 where $m_1 = 5$ kg, $m_2 = 500$ kg, $m_w = 20$ kg, and $r = 0.1$ m. The numerical properties of the hoist cable are given by $\rho_c = 1000$ kg/m^3, $L = 5$ m, and $r_c = 0.002$ m. The mass of the cable with nominal length $L = 5$ m is $m_c = \pi\rho_c r_c^2 L = 0.0628$ kg. The system's natural damping is chosen as $c_\theta = 10^{-12}$ N·s/m

and $\mathbf{D}_{ee} = \begin{bmatrix} 12.4842 & 11.5019 \\ 0.5751 & 1.2484 \end{bmatrix}$, which corresponds to a damping ratio of less than 5 % for the hoist cable's axial modes of vibration and negligible damping of the hoist cable sway.

The constants of the adaptive feedforward control input are chosen as $\delta_\theta = 550$ kg/rad, $\delta_\phi = 1.5 \times 10^{-4}$ kg·m/rad, $\delta_{\theta,\rho} = 750$ kg/rad and $\delta_{\phi,\rho} = 1.5 \times 10^{-3}$ kg/rad based on the upper bound of the eigenvalues of $\frac{\partial \bar{\mathbf{M}}}{\partial \theta}$, $\frac{\partial \bar{\mathbf{M}}}{\partial \phi}$, $\frac{\partial \bar{\mathbf{M}}_{\rho\rho}}{\partial \theta}$ and $\frac{\partial \bar{\mathbf{M}}_{\rho\rho}}{\partial \phi}$ in the range $-\frac{\pi}{2} < \theta < \frac{\pi}{2}$ and $0 < \phi < \frac{L}{r}$ as shown in Figure 4.3.

The desired trajectory of the payload is chosen based on the smooth fifth-order polynomial

$$\boldsymbol{\rho}_d = \left(10\hat{t}^3 - 15\hat{t}^4 + 6\hat{t}^5\right)(\boldsymbol{\rho}_f - \boldsymbol{\rho}_i) + \boldsymbol{\rho}_i,$$

where $\hat{t} = (t - t_i)/(t_f - t_i)$, t_i is the initial time, t_f is the final time, $\boldsymbol{\rho}_i$ is the initial position, and $\boldsymbol{\rho}_f$ is the desired final position of the trajectory. Four instances of this trajectory are performed sequentially in 7 second intervals with a 7 second rest period in between. The numerical parameters of the desired trajectory are given in Table 4.1.

Table 4.1: Parameters for desired payload trajectory.

Time	$\boldsymbol{\rho}_i^\mathsf{T}$	$\boldsymbol{\rho}_f^\mathsf{T}$
$0 \le t < 7$	$\begin{bmatrix} 0 & 5 \end{bmatrix}$	$\begin{bmatrix} 0 & 5 \end{bmatrix}$
$7 \le t < 14$	$\begin{bmatrix} 0 & 5 \end{bmatrix}$	$\begin{bmatrix} 4 & 1 \end{bmatrix}$
$14 \le t < 21$	$\begin{bmatrix} 4 & 1 \end{bmatrix}$	$\begin{bmatrix} 4 & 1 \end{bmatrix}$
$21 \le t < 28$	$\begin{bmatrix} 4 & 1 \end{bmatrix}$	$\begin{bmatrix} 3 & 5 \end{bmatrix}$
$28 \le t < 35$	$\begin{bmatrix} 3 & 5 \end{bmatrix}$	$\begin{bmatrix} 3 & 5 \end{bmatrix}$
$35 \le t < 42$	$\begin{bmatrix} 3 & 5 \end{bmatrix}$	$\begin{bmatrix} -3 & 4 \end{bmatrix}$
$42 \le t < 49$	$\begin{bmatrix} -3 & 4 \end{bmatrix}$	$\begin{bmatrix} -3 & 4 \end{bmatrix}$
$49 \le t < 56$	$\begin{bmatrix} -3 & 4 \end{bmatrix}$	$\begin{bmatrix} 0 & 5 \end{bmatrix}$
$56 \le t < 63$	$\begin{bmatrix} 0 & 5 \end{bmatrix}$	$\begin{bmatrix} 0 & 5 \end{bmatrix}$

Numerical simulation results in the $\mathbf{q}_a$ coordinates using the control parameters given by $\lambda_1 = 16$ s^{-1}, $\lambda_2 = 4$ s^{-1}, $\alpha_1 = 4$ m/(s·rad), $K_{d,1} = 10^5$ N·s/m, $K_{d,2} = 10^5$ N·m·s/rad, $\boldsymbol{\Gamma} = \mathbf{1}_{12\times 12}$ are presented in Figures 4.4 to 4.7 including the payload

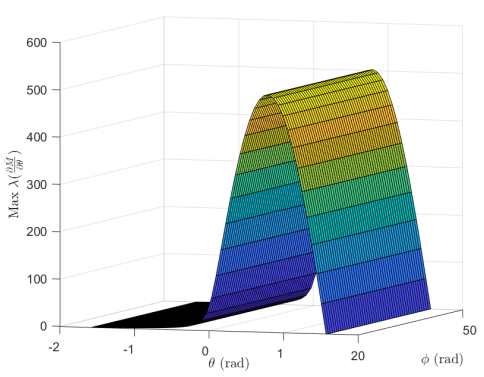

(a) Maximum eigenvalues of $\frac{\partial \bar{\mathbf{M}}}{\partial \theta}$.

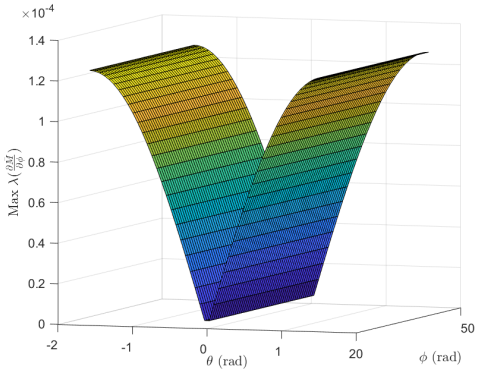

(b) Maximum eigenvalues of $\frac{\partial \bar{\mathbf{M}}}{\partial \phi}$.

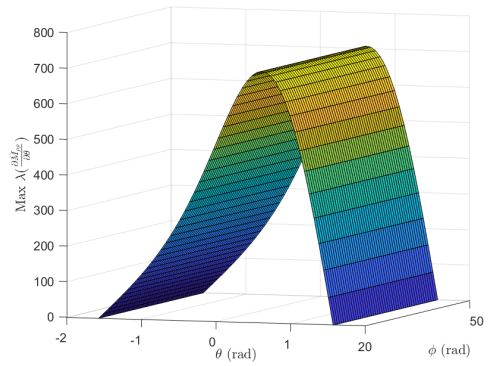

(c) Maximum eigenvalues of $\frac{\partial \bar{\mathbf{M}}_{\rho\rho}}{\partial \theta}$.

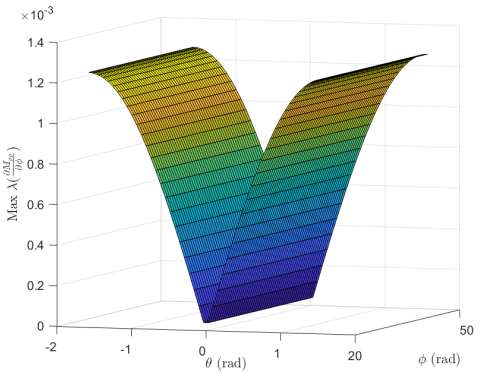

(d) Maximum eigenvalues of $\frac{\partial \bar{\mathbf{M}}_{\rho\rho}}{\partial \phi}$.

Figure 4.3: Maximum eigenvalues of partial derivatives of $\bar{\mathbf{M}}$ and $\bar{\mathbf{M}}_{\rho\rho}$ with model parameters $m_1 = 5$ kg, $m_2 = 500$ kg, $m_w = 20$ kg, $r = 0.1$ m, $\rho_c = 1000$ kg/m^3, $L = 5$ m, $r_c = 0.002$ m in the range $-\frac{\pi}{2} < \theta < \frac{\pi}{2}$ and $0 < \phi < \frac{L}{r}$.

trajectory versus time in Figure 4.4, the velocity tracking versus time in Figure 4.5, the rate tracking error 4.6, and the control inputs versus time in Figure 4.7. For clarity, the figure captions and axis labels refer to the "x-axis" and "y-axis" instead of $\underrightarrow{a}^1$ and $\underrightarrow{a}^2$, where $\boldsymbol{\rho}^\mathsf{T} = \begin{bmatrix} \rho_x & \rho_y \end{bmatrix}$ and $\dot{\boldsymbol{\rho}}^\mathsf{T} = \begin{bmatrix} \dot{\rho}_x & \dot{\rho}_y \end{bmatrix}$.

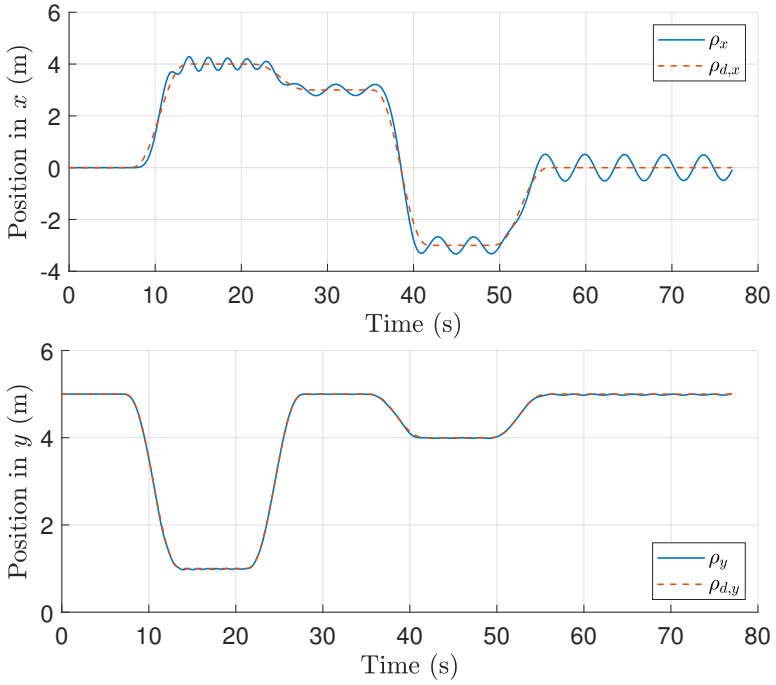

Figure 4.4: Payload position tracking with the control law in (4.21).

Another simulation in the $\boldsymbol{\rho}_a$ coordinates with the equivalent control parameters $\lambda_{\rho,1} = 16$ s^{-1}, $\lambda_{\rho,2} = 4$ s^{-1}, $\alpha_{\rho,1} = 4$ m/(s·rad), and $\mathbf{K}_{d,\rho} = 10^5 \times \text{diag}\{1, \frac{1}{r^2}\}$ N·s/m, and $\boldsymbol{\Gamma}_\rho = \text{diag}(1, \frac{1}{r^2}, 1, \frac{1}{r^2}, 1, \frac{1}{r^2}, 1, \frac{1}{r^2}, 1, 1, 1, 1)$ are presented as a comparison. The simulation results are presented in Figures 4.8 to 4.11, including the payload trajectory versus time in Figure 4.8, the velocity tracking versus time in Figure 4.9, the velocity tracking error versus time in Figure 4.10, and the control inputs versus time in Figure 4.11.

Comparing the simulation results in the $\boldsymbol{\rho}_a$ coordinates and $\mathbf{q}_a$ coordinates using the control law in (4.21) and (4.43), the transformation between these two coordinates are both verified. In the interest of brevity, only one simulation result

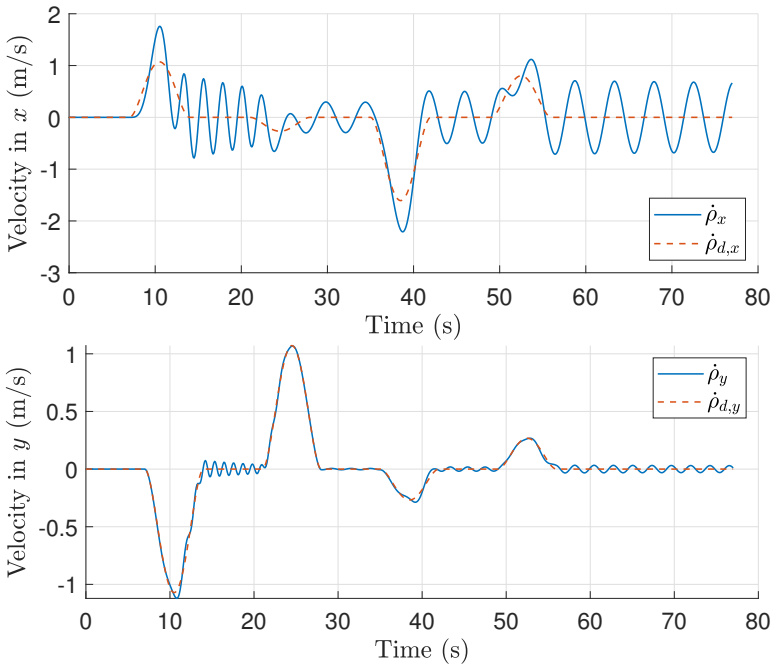

Figure 4.5: Payload velocity tracking with the control law in (4.21).

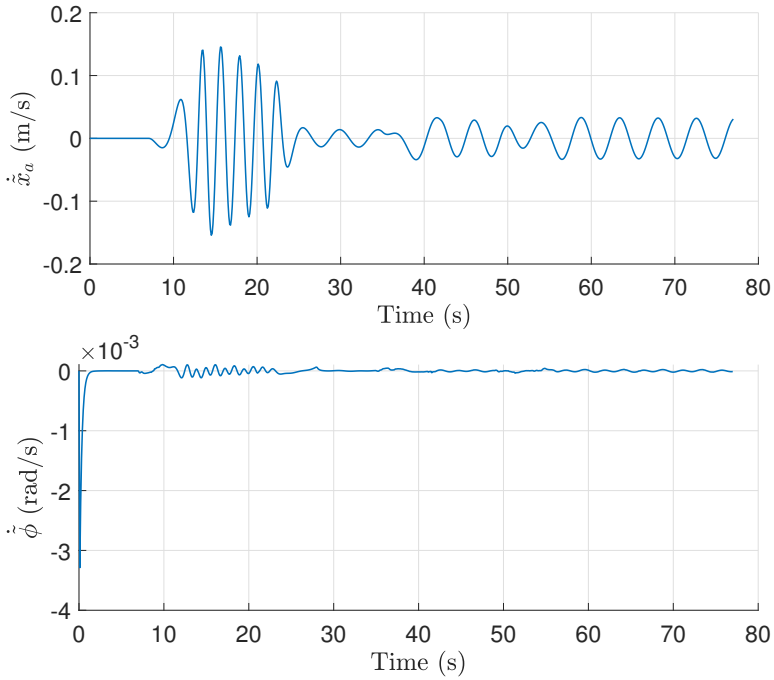

Figure 4.6: States rate tracking with the control law in (4.21).

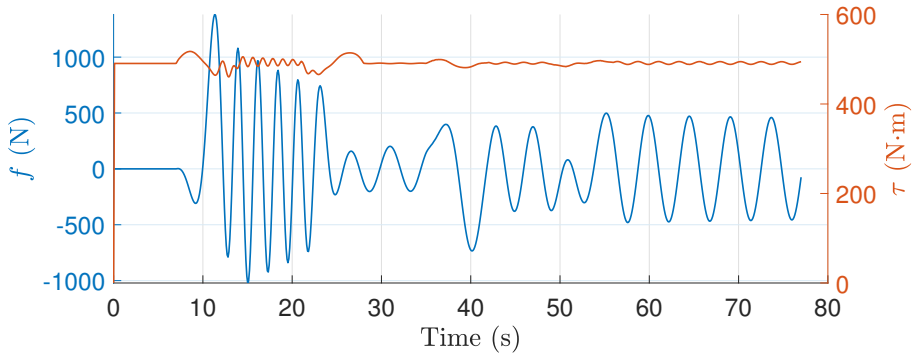

Figure 4.7: Control inputs f (blue) and τ (orange) with the control law in (4.21).

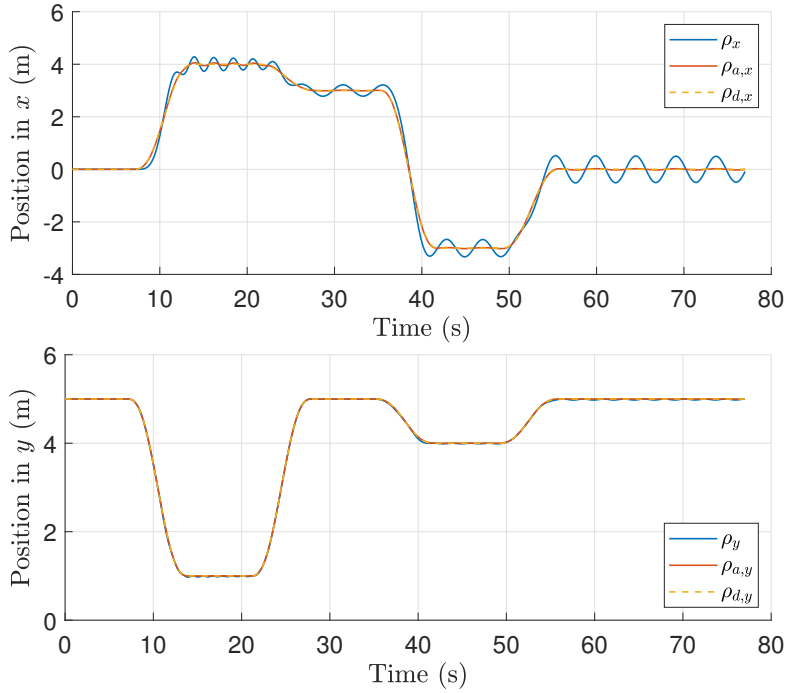

Figure 4.8: Payload position tracking with the control law in (4.43).

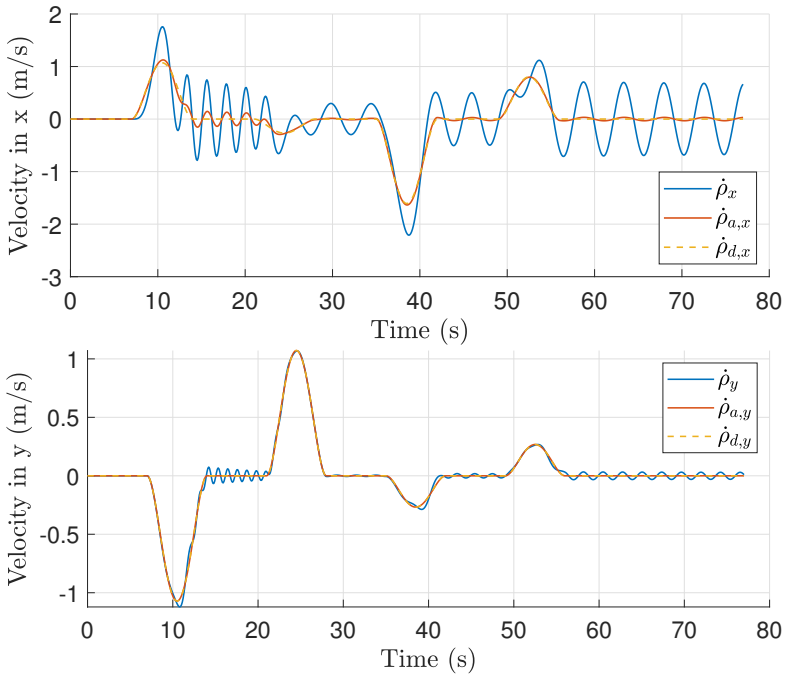

Figure 4.9: Payload velocity tracking with the control law in (4.43).

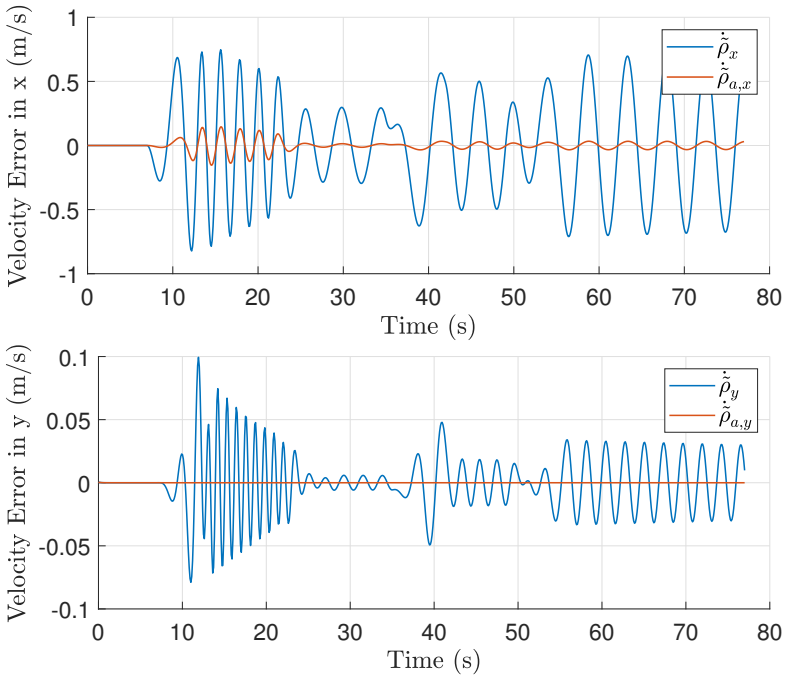

Figure 4.10: Payload velocity tracking error with the control law in (4.43).

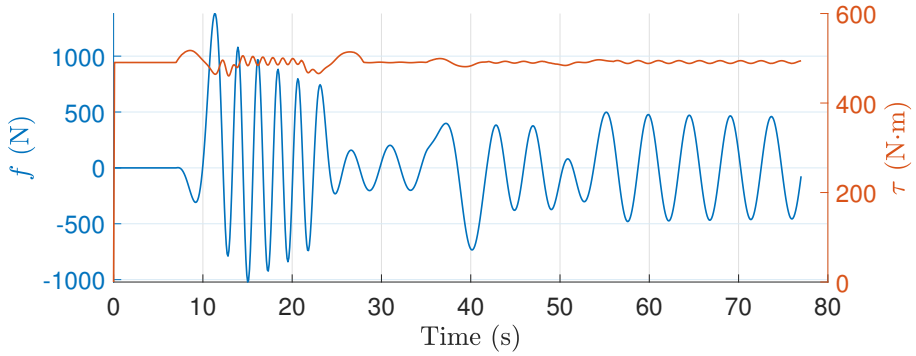

Figure 4.11: Control inputs f (blue) and τ (orange) with the control law in (4.43).

is presented. It is worth noting that by speeding up the payload trajectory motion, the sway angle gets large, but the system remains input-output stable. This confirms that the adaptive sliding-mode control method preserves the stability of the closed-loop system, and the restriction of small sway angle used in Chapter 3 is removed.

To compare to the adaptive method used in [32], a numerical simulation is performed with

$$\bar{\mathbf{u}} = -\mathbf{K}_d \mathbf{sat}(\mathbf{s}), \quad \text{where } \mathbf{sat}(\mathbf{s}) = \begin{cases} 1 & \text{if } \frac{s_i}{\epsilon} > 1 \\ \frac{s_i}{\epsilon} & \text{if } -1 < \frac{s_i}{\epsilon} < 1, \\ -1 & \text{if } \frac{s_i}{\epsilon} < -1 \end{cases}$$

s_i is the element of $\mathbf{s}$, and ϵ is a constant that denotes the thickness of the boundary layer [32]. Substituting $\bar{\mathbf{u}} = -\mathbf{K}_d \mathbf{sat}(\mathbf{s})$ into (4.21), the control law becomes

$$\mathbf{U} = \hat{\mathbf{U}} + \bar{\mathbf{u}} = \hat{\mathbf{M}}\ddot{\mathbf{q}}_{a,r} + \hat{\mathbf{B}}\dot{\mathbf{q}}_a + \hat{\mathbf{C}}\dot{q}_u + \hat{\mathbf{G}} - \tfrac{1}{2}(\delta_\theta \dot{\theta} + \delta_\phi \dot{\phi})\mathbf{s} - \mathbf{K}_d \mathbf{sat}(\mathbf{s}). \tag{4.46}$$

Note that the control law in (4.46) is not identical to the control law used in [32], as the adaptive feedforward control input in [32] relies on a configuration-specific structure of the system dynamics that is not applicable to the crane system considered in this work. Moreover, the adaptive update law in [32] requires exact

knowledge of the system's mass properties, which is not required in the proposed adaptive control formulation. Choosing $\epsilon = 0.01$, the results with the control law in (4.46) are shown in Figures 4.12 to 4.15, including the payload trajectory versus time in Figure 4.12, the velocity tracking versus time in Figure 4.13, the rate tracking error 4.14, and the control inputs versus time in Figure 4.15.

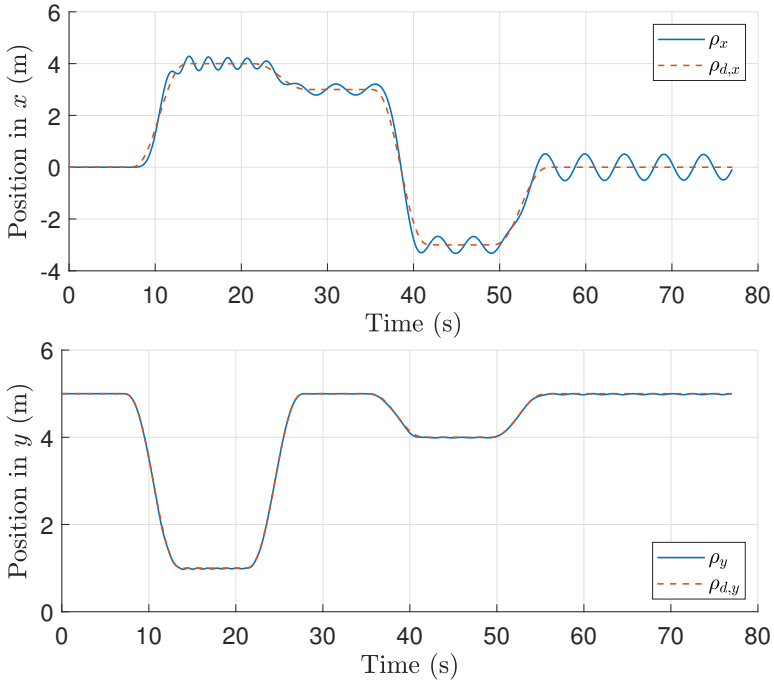

Figure 4.12: Payload position tracking with the control law in (4.46).

Comparison of the control laws in (4.21), (4.43), and (4.46) are presented in Figures 4.16 to 4.19. Specifically, subscript q denotes the control law in (4.21), subscript ρ denotes the control law in (4.43), and subscript T denotes the control law in (4.46).

The results with the control laws in (4.21), (4.43), and (4.46) are quite similar, which is to be expected considering that (4.21) and (4.43) only differ by a coordinate transformation, and (4.46) uses a similar adaptive feedforward structure. Comparing the adaptive method in [32] and the method in Sections 4.3.2, the numerical results does not show too much of a difference, but the "model specific"

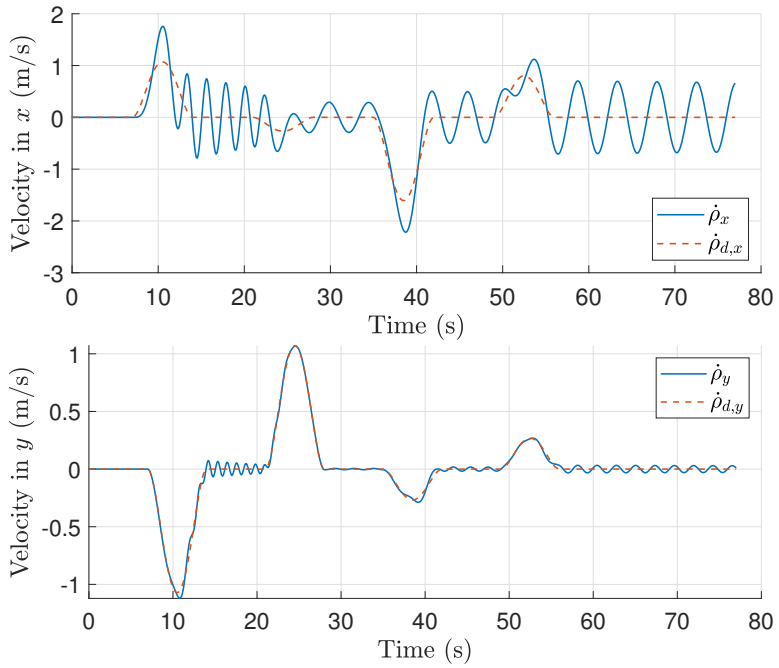

Figure 4.13: Payload velocity tracking with the control law in (4.46).

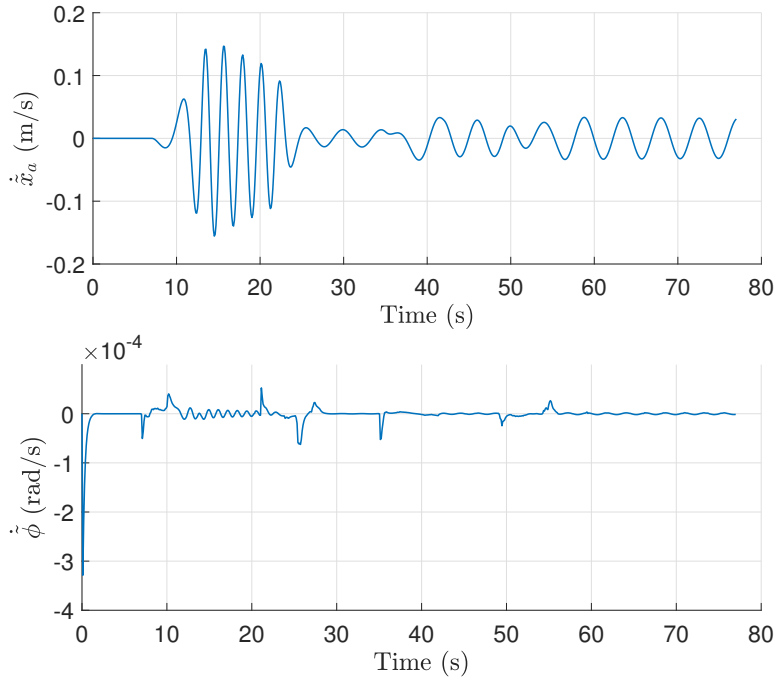

Figure 4.14: States rate tracking with the control law in (4.46).

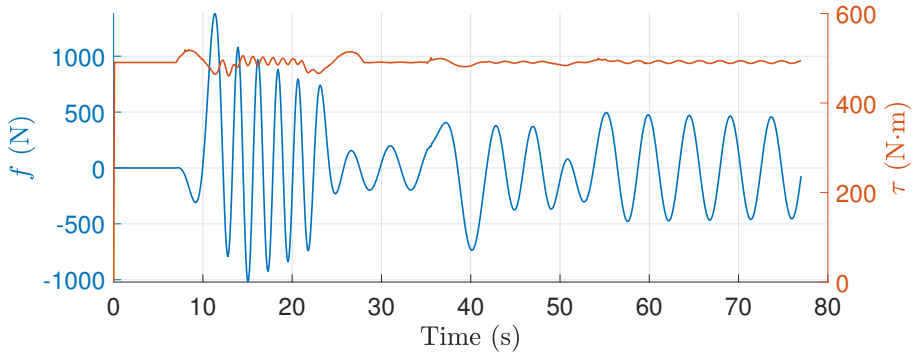

Figure 4.15: Control inputs f (blue) and τ (orange) with the control law in (4.46).

adaptive law in [32] is replaced by a more general adaptation as in Sections 4.3.2.

4.6 Conclusion

The passivity-based adaptive sliding-mode control method inspired by the sliding-mode method in [32] and the adaptive control method in [42, 43] gives a solution to reduce the payload swaying while tracking a payload trajectory. Although the performance of the proposed method does not track the payload position and velocity as well as the μ-tip method proposed in Chapter 3, the passivity-based adaptive sliding-mode control method removes the limitation of a small sway angle, and accounts for uncertainties of the model with an adaptive control law. This is a more practical and applicable control method. The proposed adaptive method provides a more generic adaptive law with less requirement of the knowledge of system's mass properties comparing to the adaptive law in [32] that requires the dynamic structure and the mass of the payload known to form the adaptive law. The passivity-based adaptive sliding-mode control in $\boldsymbol{\rho}_a$ coordinates shows a more intuitive way for designing a controller that tracks the desired trajectory in the task space, and the control gains $\mathbf{K}_d = \text{diag}(K_{d,1}, K_{d,2})$ are in the same unit and same scale. This can also be seen as a step before applying the μ-tip method to account for a flexible hoist cable. The reformulation of the dynamics in the $\boldsymbol{\rho}_a$ coordinated can be further extended with a μ-tip method to solve the flexibility

of the cable. This is an interesting extension of the work in this section that is to be investigated in future work.

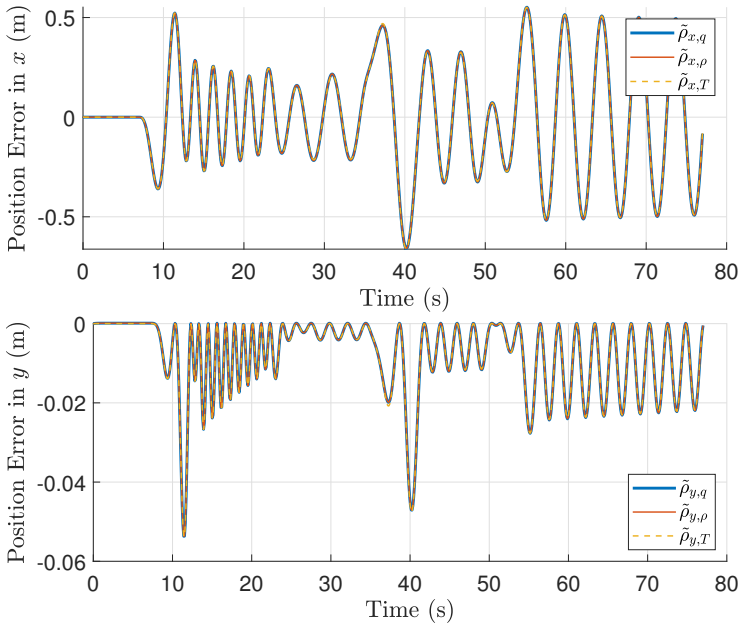

Figure 4.16: Payload position tracking error with the control laws in (4.21), (4.43), and (4.46).

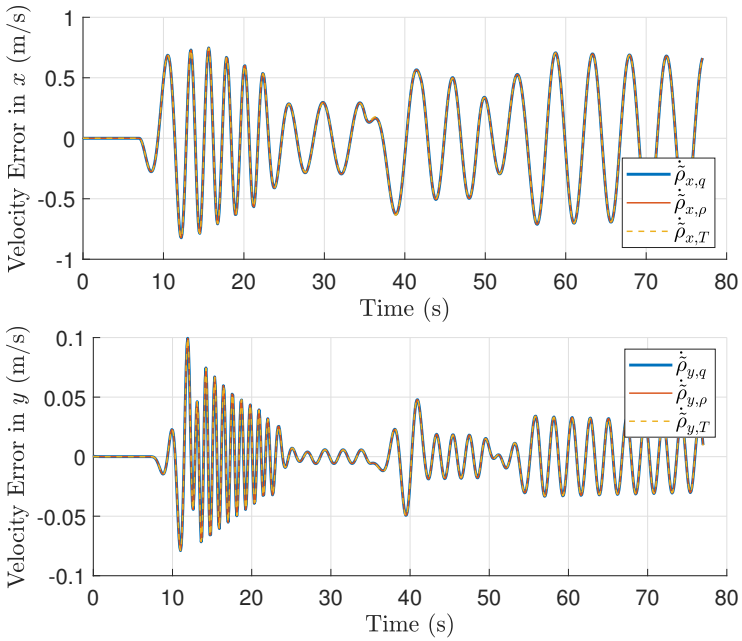

Figure 4.17: Payload velocity tracking error with the control laws in (4.21), (4.43), and (4.46).

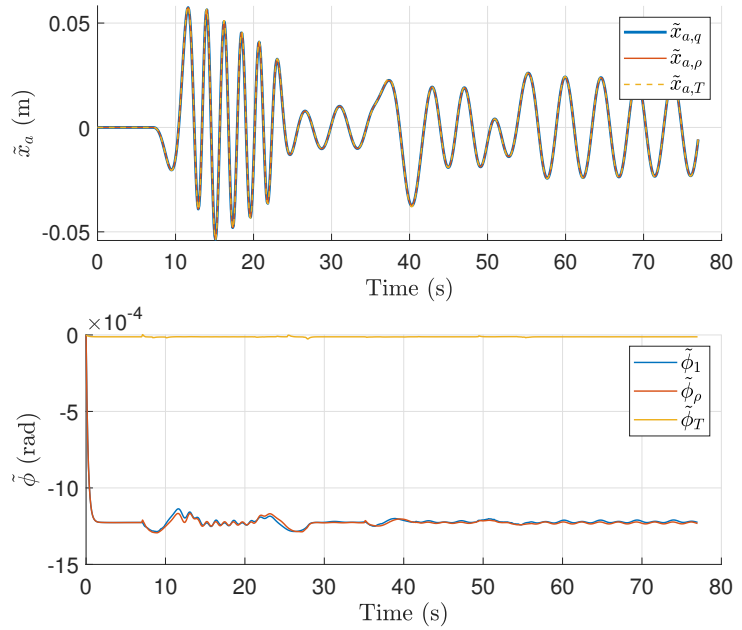

Figure 4.18: States tracking error $\tilde{\mathbf{q}}_a$ with the control laws in (4.21), (4.43), and (4.46).

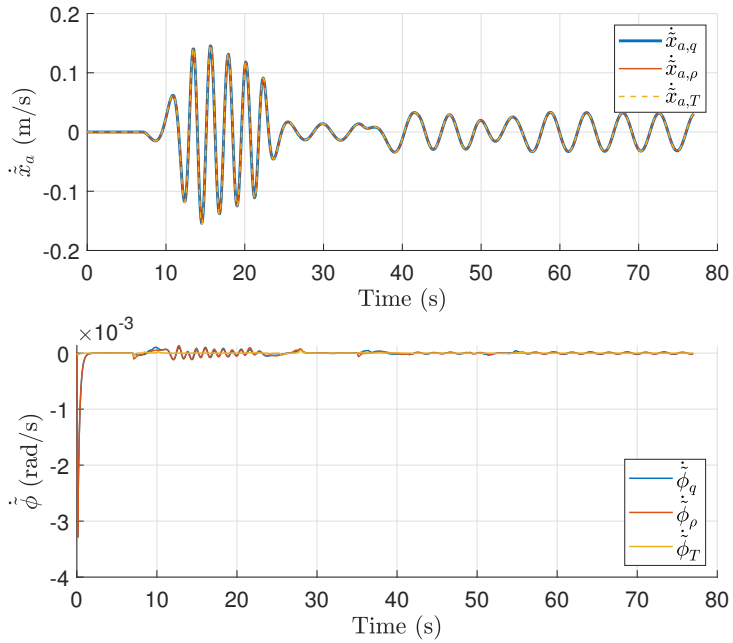

Figure 4.19: State rates tracking error $\dot{\tilde{\mathbf{q}}}_a$ with the control laws in (4.21), (4.43), and (4.46).

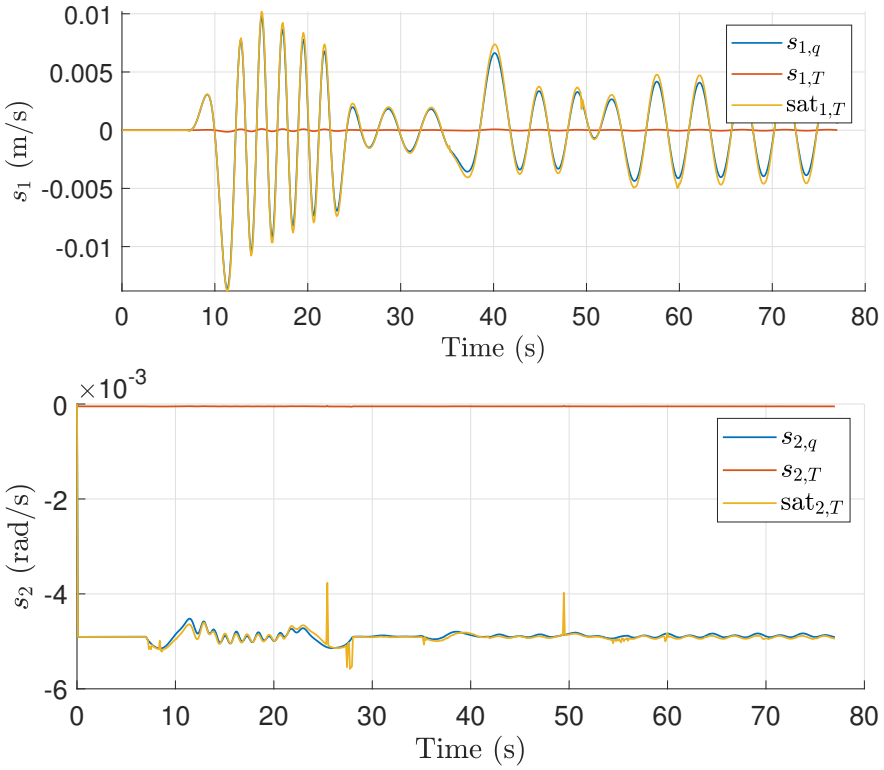

Figure 4.20: Sliding surfaces $\mathbf{s}$ and $\mathbf{sat}(\mathbf{s})$ with the control laws in (4.21), and (4.46).

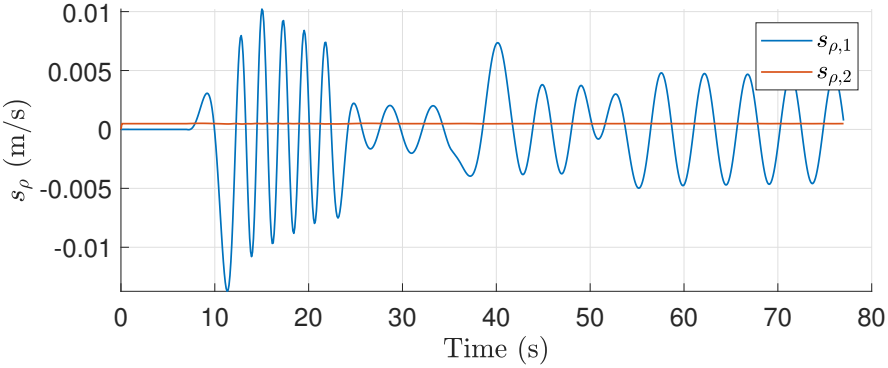

Figure 4.21: Sliding surfaces $\mathbf{s}_\rho$ with the control law in (4.43).

Chapter 5

Experiment

5.1 Introduction

Chapter 4 provides numerical simulations of the passivity-based adaptive sliding-mode control method theorems. This chapter aims to validate and demonstrate the practicality of the adaptive sliding-mode control method in the $\mathbf{q}_a$ coordinates presented in Section 4.3 using a small-scale tower crane manufactured by Quanser, shown in Figure 5.1. This existing small-scale system provides a testbed on which to test the control theory developed in Chapter 4 without focusing on the many practical engineering problems that would be encountered if the system were designed and built from scratch. Details of the experiment setup including the 3 DOF tower crane system and the closed-loop control model can be found in Section 5.2. The experimental results of the adaptive sliding-mode control are presented in Section 5.3.

5.2 Experiment Setup

Details on the hardware setup of system are found in the Quanser 3 DOF Tower Crane User Manual [2]. This small-scale (1.5 m tall) tower crane features a vertical tower, a horizontal rotary jib, a trolley (or a cart in [2]) moving along the

Figure 5.1: Quanser 3 DOF Crane [2].

jib, and a winding cable on the cart that connects to a payload on its other end. There are three motors controlling the movement of the winch, trolley and jib. Five encoders are used to measure the angular positions of the three motors and the two Euler angles that define the three-dimensional sway of the payload. The payload is attached to one end of a kevlar hoist cable, which is considered non-extensible. The signals from the encoders and the current driving the motors are processed by the DAQ terminal board, HIL data acquisition card, and AMPAQ power amplifier. The crane, AMPAQ, DAQ and HIL are wired to a PC, and the signals are processed using Matlab and Simulink interface. The representative parameters of the crane are given as $r = 0.0127$ m, $m_2 = 0.147$ kg, $m_1 + m_w = 0.6$ kg, $L = 0.8636$ m, and negligible cable mass. Details of the physical components of the crane can be found in [2].

A modification of the Simulink model provided in [2] is developed to conduct experiments with the proposed control method in Section 4.3. Figure 5.2 includes a screenshot of the Simulink model that shows the overall structure of the code. The

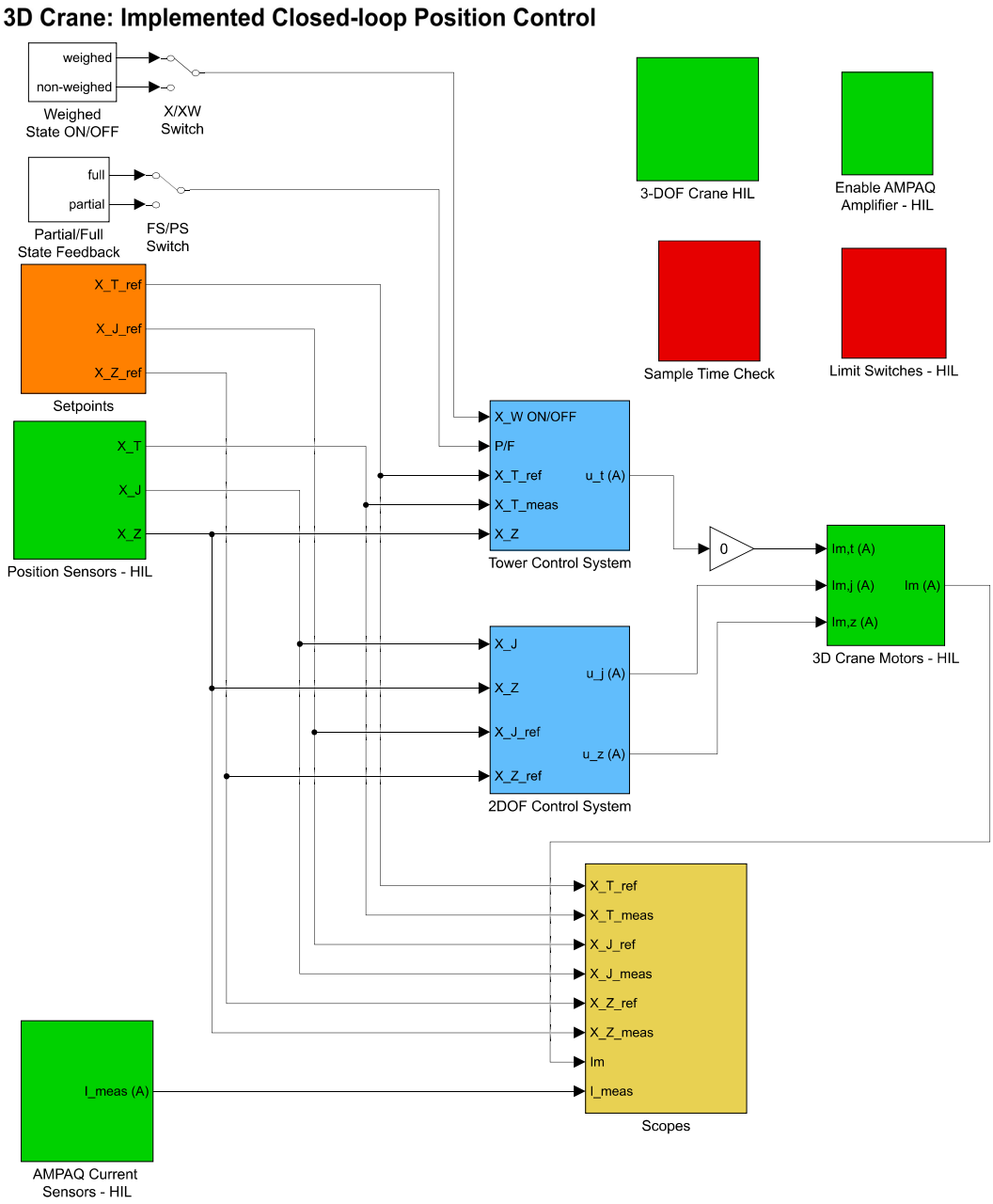

Figure 5.2: Modified 3 DOF crane closed-loop control model in Simulink.

system states are given by the block of Position Sensors - HIL. The measurements of the states $\mathbf{q} = \begin{bmatrix} \mathbf{q}_a^T & q_u \end{bmatrix}^T = \begin{bmatrix} x_a & \phi & \theta \end{bmatrix}^T$ are captured by the built-in encoders processed with a low-pass filter. The rate of these states $\dot{\mathbf{q}} = \begin{bmatrix} \dot{x}_a & \dot{\phi} & \dot{\theta} \end{bmatrix}^T$ are given by the encoder signals passing through a low-pass derivative filter.

Figure 5.3 shows the 2 DOF control system block in Figure 5.2. The original measurements from the payload position sensors are the cable length and its change rate (not exactly the same as ℓ_i and $\dot{\ell}_i$, since Quanser defines the reference frame differently), which is divided by r to obtain the winch angle ϕ and rate $\dot{\phi}$.

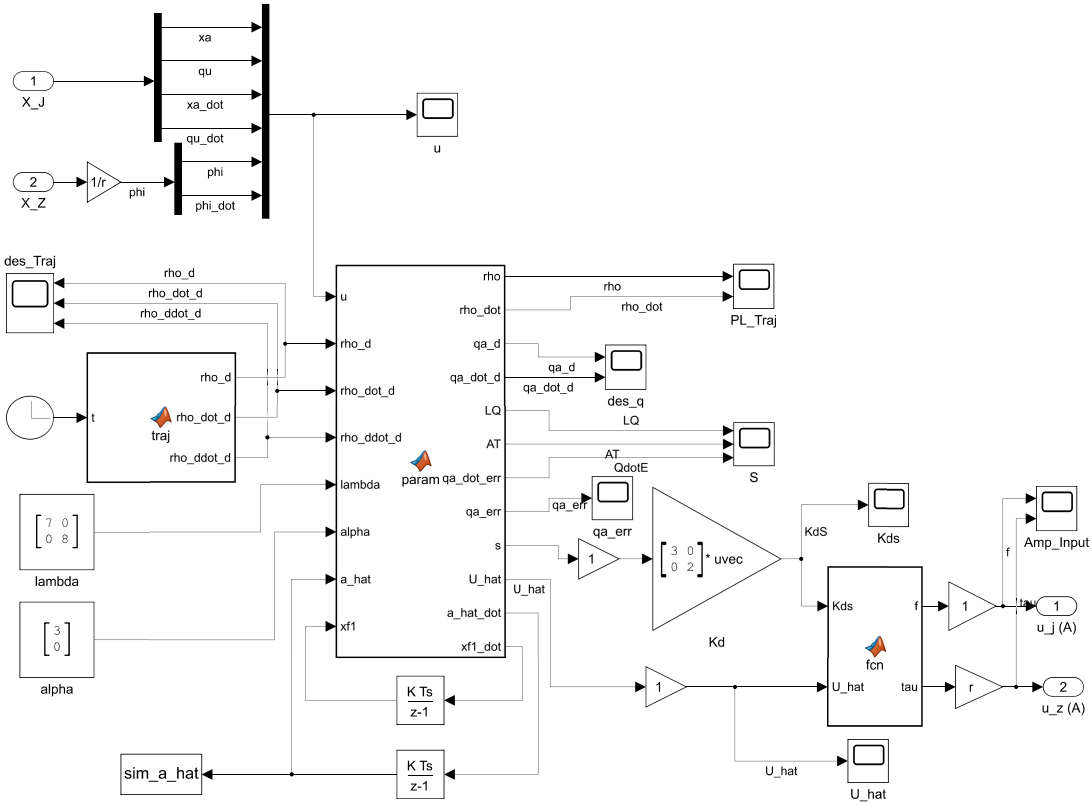

Figure 5.3: 2D controller model.

5.3 Experiment Results

5.3.1 COVID-19 Statement

The University of Minnesota moved to extended reduced operations on March 17, 2020 due to the COVID-19 pandemic, which forced the closure of the Aerospace, Robotics, Dynamics, and Control (ARDC) Laboratory. The experiment presented in this chapter were done before the closure of the ARDC Lab. In Section 4.3, the adaptive sliding-mode control law is chosen as

$$\mathbf{U} = \hat{\mathbf{U}} + \bar{\mathbf{u}} = \hat{\mathbf{M}}\ddot{\mathbf{q}}_{a,r} + \hat{\mathbf{B}}\dot{\mathbf{q}}_a + \hat{\mathbf{C}}\dot{q}_u + \hat{\mathbf{G}} - \tfrac{1}{2}(\delta_\theta\dot{\theta} + \delta_\phi\dot{\phi})\mathbf{s} - \mathbf{K}_d\mathbf{s}. \tag{4.21}$$

This form of the adaptive feedforward input $\hat{\mathbf{U}} = \hat{\mathbf{M}}\ddot{\mathbf{q}}_{a,r} + \hat{\mathbf{B}}\dot{\mathbf{q}}_a + \hat{\mathbf{C}}\dot{q}_u + \hat{\mathbf{G}} - \frac{1}{2}(\delta_\theta\dot{\theta} + \delta_\phi\dot{\phi})\mathbf{s}$ was formulated after the university closure. As such, the control law described in this chapter that was implemented in the experiments does not exactly match the controller in Section 4.3. Due to the graduation time limit specified by the Taiwanese fellowship that funded the research in this thesis, it is not possible to obtain experimental results with the controller described in Section 4.3. This is left as potential work for a future graduate student.

5.3.2 Experiments of Adaptive Sliding-Mode Control

The adaptive control law presented in Section 4.3 requires measurements of $\dot{\mathbf{q}}_a$, $\dot{q}_u$, $\mathbf{q}_a$, q_u in order to calculate the regressor matrix $\mathbf{W}$. Unfortunately, these measurements are not readily available in the experimental setup. Through experimental testing it was shown that simple low-pass derivative filters do not yield a sufficiently accurate estimate of these quantities for use with the adaptive control law. For this reason, two simplifications of the adaptive control law are implemented experimentally: one that does not perform any adaptation, and another that lumps all adaptive terms into a single term that involves a constant regressor. Removing the adaptive control input is undesirable, as this adaptation is required in order to establish the passive input-output mapping upon which closed-loop input-output

stability of the system is established. Although a single adaptive term based on a constant regressor does not exactly account for the dynamics of the true system, it can provide a reasonable approximation of the system dynamics provided they are slowly varying with time.

To show the payload tracking performance, the desired trajectory is designed with a vertical upward movement, a horizontal rightward movement, and a cross diagonal left-and-downward movement. As in the numerical simulations, the desired trajectory of the payload is chosen based on the smooth fifth-order polynomial

$$\boldsymbol{\rho}_d = \left(10\hat{t}^3 - 15\hat{t}^4 + 6\hat{t}^5\right)(\boldsymbol{\rho}_f - \boldsymbol{\rho}_i) + \boldsymbol{\rho}_i,$$

where $\hat{t} = (t - t_i)/(t_f - t_i)$, t_i is the initial time, t_f is the final time, $\boldsymbol{\rho}_i$ is the initial position, and $\boldsymbol{\rho}_f$ is the desired final position of the trajectory. Three instances of this trajectory are performed sequentially in 2 second intervals with a 4 second rest period in between. The numerical parameters of the desired trajectory are given in Table 5.1.

Table 5.1: Parameters for desired payload trajectory.

Time	$\boldsymbol{\rho}_i^\mathsf{T}$	$\boldsymbol{\rho}_f^\mathsf{T}$
$0 \le t < 4$	$\begin{bmatrix}0 & 0.8638\end{bmatrix}$	$\begin{bmatrix}0 & 0.8636\end{bmatrix}$
$4 \le t < 6$	$\begin{bmatrix}0 & 0.8636\end{bmatrix}$	$\begin{bmatrix}0 & 0.5\end{bmatrix}$
$6 \le t < 10$	$\begin{bmatrix}0 & 0.5\end{bmatrix}$	$\begin{bmatrix}0 & 0.5\end{bmatrix}$
$10 \le t < 12$	$\begin{bmatrix}0 & 0.5\end{bmatrix}$	$\begin{bmatrix}0.15 & 0.5\end{bmatrix}$
$12 \le t < 18$	$\begin{bmatrix}0.15 & 0.5\end{bmatrix}$	$\begin{bmatrix}0.15 & 0.5\end{bmatrix}$
$18 \le t < 20$	$\begin{bmatrix}0.15 & 0.5\end{bmatrix}$	$\begin{bmatrix}0 & 0.8638\end{bmatrix}$
$20 \le t < 23$	$\begin{bmatrix}0 & 0.8638\end{bmatrix}$	$\begin{bmatrix}0 & 0.8638\end{bmatrix}$

The first experiment considers no adaptive input. The control law is thus chosen as

$$\mathbf{U} = \begin{bmatrix} f \\ \tau \end{bmatrix} = \hat{\mathbf{U}} + \bar{\mathbf{u}} = -\mathbf{K}_d \mathbf{s}, \tag{5.1}$$

where

$$\mathbf{s} = \begin{bmatrix} s_1 \\ s_2 \end{bmatrix} = \dot{\tilde{\mathbf{q}}}_a + \boldsymbol{\lambda}\tilde{\mathbf{q}}_a + \boldsymbol{\alpha} q_u.$$

Another experiment considers only the gravity terms in the adaptive input, where the control law is

$$\mathbf{U} = \hat{\mathbf{U}} + \bar{\mathbf{u}} = \hat{\mathbf{G}} - \mathbf{K}_d \mathbf{s}. \tag{5.2}$$

The feedback control parameters are chosen the same as for both of the experiments, where $\boldsymbol{\lambda} = \text{diag}(7, 8)$ s$^-$1, $K_{d,1} = 3$ N·s/m, $K_{d,2} = 2$ N·m·s/rad, and $\alpha_1 = 3$ m/(s·rad). The adaptive update constant matrix in the second experiment is chosen as $\boldsymbol{\Gamma} = \text{diag}(\mathbf{0}_{1\times 10}, 10, 10)$.

The result of the experiments are show in Figures 5.4 to 5.9, including the payload position tracking in Figure 5.4, the payload velocity tracking in Figure 5.5, payload position tracking error in Figure 5.6, the payload velocity tracking error in Figure 5.7, and the input force and torque with the control law in Figure 5.8 and 5.9. The subscript N represents the result using the control law in (5.1) without any adaptive input, and the subscript G represents the result using the control law in (5.2) with an adaptive gravitational feedforward.

In Figure 5.4 and 5.6, the performance of rejecting payload sway and horizontal oscillation is better when including the adaptive feedforward input in $\hat{\mathbf{G}}$. The orange lines in Figure 5.9 show the gravitational adaptive efforts. The maximum total inputs, i.e. the yellow line in Figure 5.9, is not significantly larger than the inputs in Figure 5.8. These results suggest that the adaptive feedforward input is a crucial component of the control law, as it improves the performance of the control law. The results also demonstrate the robustness of the proposed control law, as neither control law contains the exact form of the adaptive control law in Section 4.3. In future work, improvements to the state estimation of the system may be investigated to allow for components of the adaptive control law to be properly accounted for.

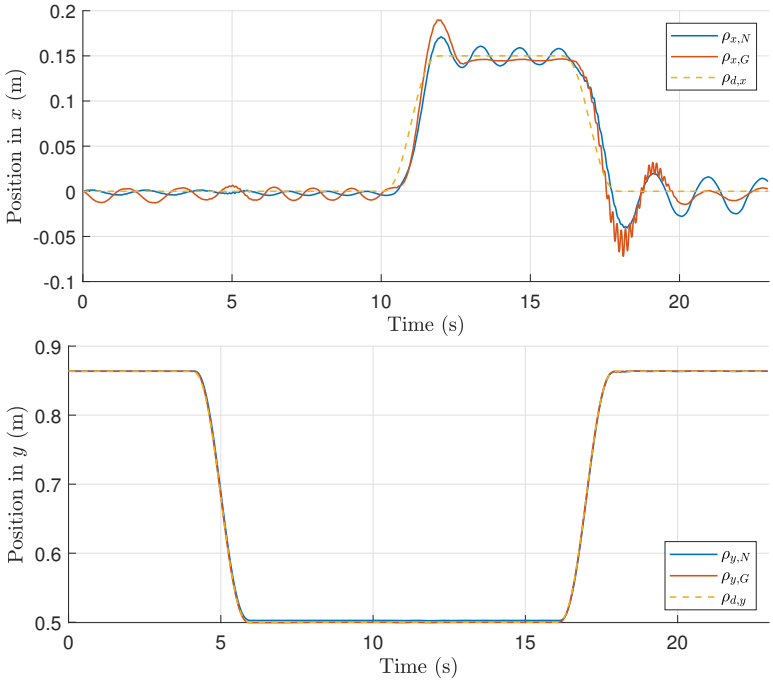

Figure 5.4: Payload position with the control law in (5.1) and (5.2).

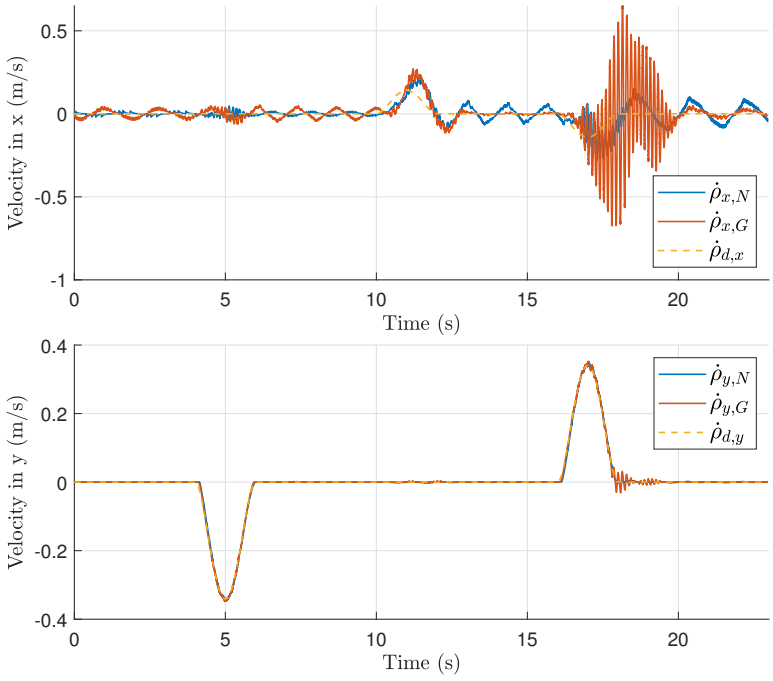

Figure 5.5: Payload velocity with the control law in (5.1) and (5.2).

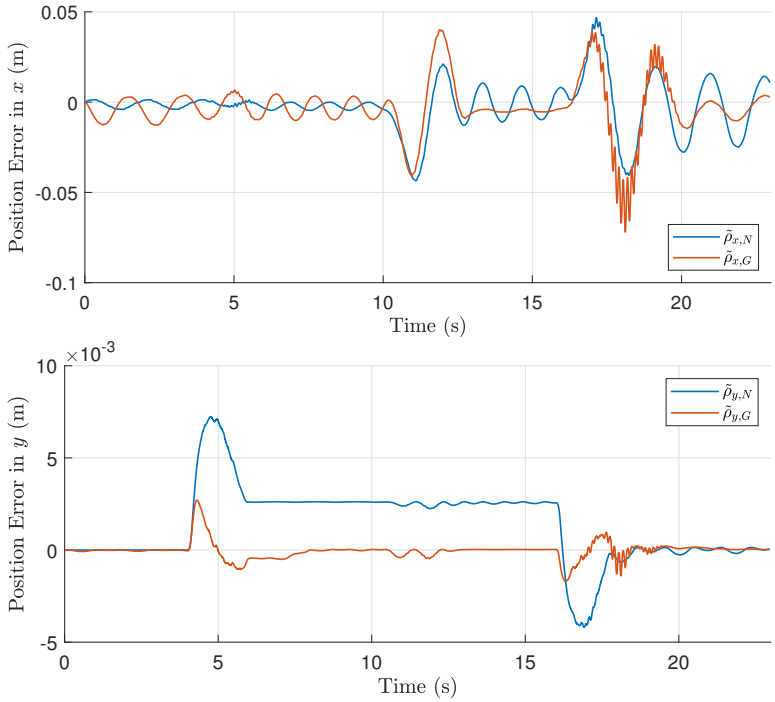

Figure 5.6: Payload position error with the control law in (5.1) and (5.2).

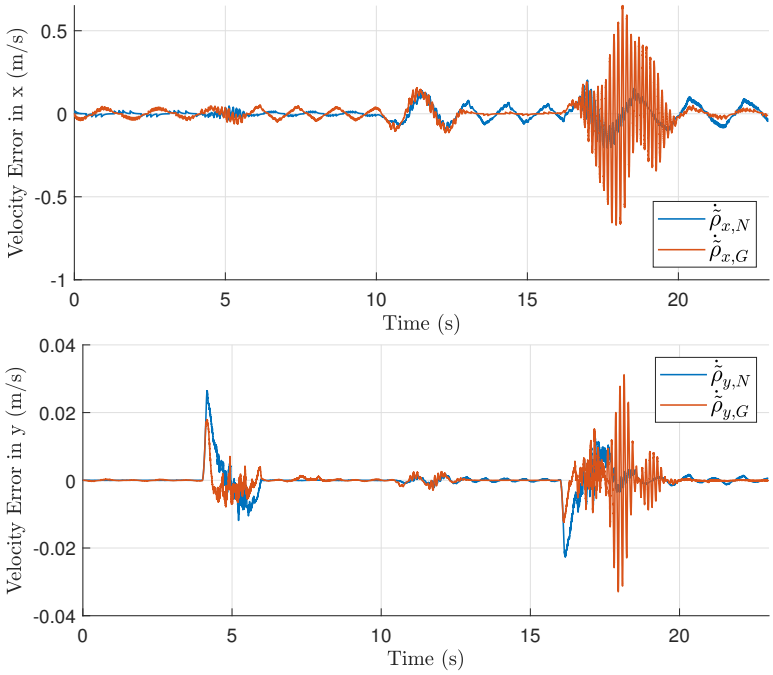

Figure 5.7: Payload velocity error with the control law in (5.1) and (5.2).

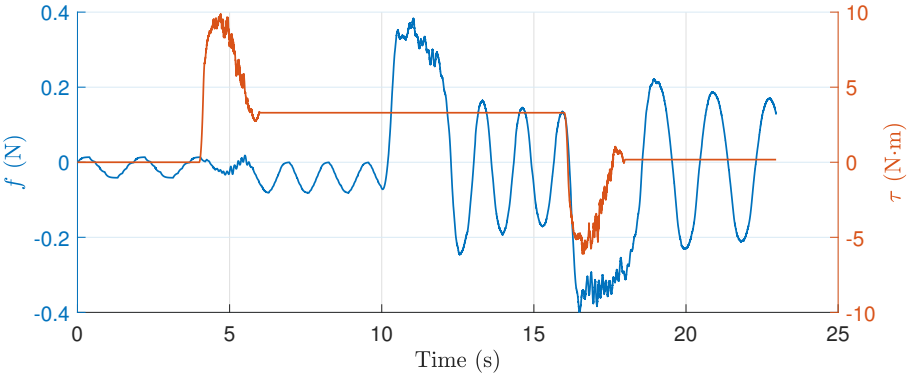

Figure 5.8: Control inputs f (blue) and τ (orange) with the control law in (5.1).

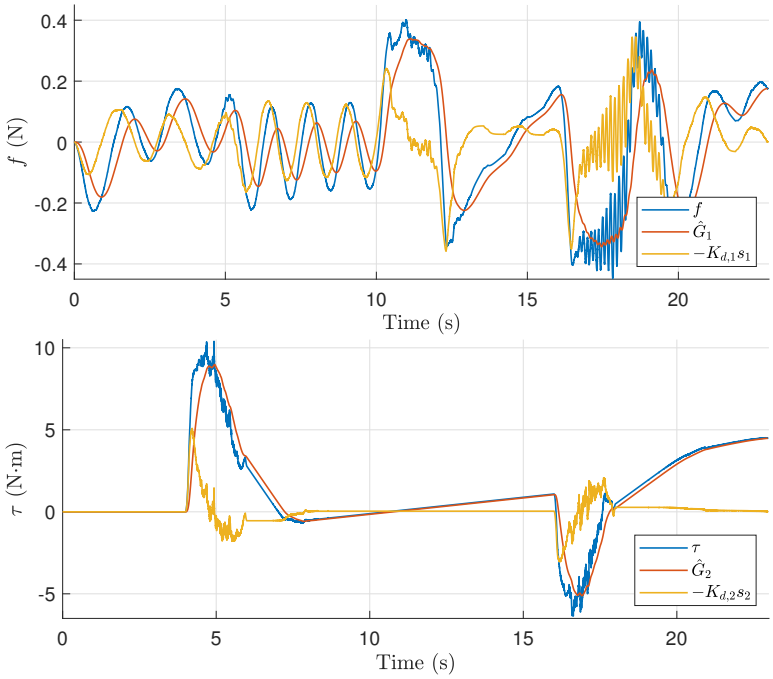

Figure 5.9: Control inputs with the control law in (5.2).

5.4 Conclusion

The numerical simulation in Chapter 4 shows the theoretical payload trajectory tracking performance of the adaptive sliding-mode control method. Although the imperfectness of the state measurements prevents the full adaptive feedforward input being applied, the experiment results validate the theory and show a stable payload trajectory tracking. Provided that improved state estimation is possible, the complete adaptive sliding-mode control law in (4.21) can be implemented in future work.

Chapter 6

Conclusions and Future Work

This thesis has presented a dynamic model of a 2 DOF tower crane that includes a flexible hoist cable and proposed passivity-based control methods for payload trajectory tracking. The proposed passivity-based μ-tip control method shows robust payload position and velocity tracking performance. However, assumptions of small sway angle and small angular rate limits applicability of this method in practice. A passivity-based adaptive sliding-mode control was then proposed to solve these limitations and to provide the ability to account for uncertainties. Experiments of the passivity-based adaptive sliding-mode control are presented, where it is verified that the payload trajectory tracking is achievable using the proposed control method. The passivity-based adaptive sliding-mode control in $\boldsymbol{\rho}_a$ coordinates is derived to present a more intuitive way for designing a controller that tracks the desired trajectory in the task space, and the control gains $\mathbf{K}_{d,\rho} = \text{diag}(K_{d,\rho 1}, K_{d,\rho 2})$ are in the same units and same scale where the gain $\mathbf{K}_d = \text{diag}(K_{d,1}, K_{d,2})$ in the $\mathbf{q}_a$ coordinates are not. This can also be seen as a step towards applying the μ-tip method to account for a flexible hoist cable.

The main contributions of this thesis related to the dynamic modeling and control of a 2 DOF tower crane are as follows.

- Modeling the axial vibration of a flexible varying-length tower crane hoist cable using a Rayleigh-Ritz discretization.

- Using a μ-tip modification to establish a passive input-output mapping of a 2 DOF tower crane with a flexible hoist cable from a modified force input to the payload's μ-tip rate by considering the sway angle θ as a flexible coordinate.

- A robust sliding-mode-inspired passivity-based control method for payload trajectory tracking with a rigid hoist cable. The novel contributions of this control method compared to the literature include

  - an adaptive update law that does not rely on a specific structure of the dynamic equations or exact knowledge of the crane's mass properties;
  - a formulation in the payload coordinates (ρ coordinates), which facilitates the generation of desired trajectories and the choice of control gains;
  - experimental validation of the proposed passivity-based sliding-mode control method.

The theory and control methods presented in this thesis can also be extended to other robotic systems that use cables for actuation. Currently, the passivity-based adaptive sliding-mode control is established on a system with a rigid hoist cable. Future work on this topic will investigate combining the adaptive sliding-mode control with the μ-tip modification considering a flexible hoist cable, and extending the current 2 DOF tower crane model to a 3 DOF system that includes rotation of the jib.

References

[1] Heavy Equipment Guide, "Linden comansa's lc 2100 series." [Online]. Available: https://www.heavyequipmentguide.ca/product/4626/lc-2100/

[2] Quanser Innovate. Educate., "3 dof crane user manual." [Online]. Available: https://www.quanser.com/products/3-dof-crane/

[3] R. Olfati-Saber, "Trajectory tracking for a flexible one-link robot using a nonlinear noncollocated output," *IEEE Decis. Contr. P.*, vol. 4, pp. 4024–4029, 2000.

[4] Y. Liu and H. Yu, "A survey of underactuated mechanical systems," *IET Control Theory A.*, vol. 7, no. 7, pp. 921–935, 2013.

[5] F. Ju and Y. S. Choo, "Dynamic analysis of tower cranes," *J. Eng. Mech.*, vol. 131, no. 1, pp. 88–96, 2005.

[6] L. A. Tuan and S.-G. Lee, "Modeling and advanced sliding mode controls of crawler cranes considering wire rope elasticity and complicated operations," *Mech. Syst. Signal Pr.*, vol. 103, pp. 250–263, 2018.

[7] S. Zhang and X. He, "Boundary control of a flexible crane system in two-dimensional space," *IET Control Theory A.*, vol. 11, no. 14, pp. 2187–2194, 2017.

[8] X. Xing and J. Liu, "Pde modelling and vibration control of overhead crane bridge with unknown control directions and parametric uncertainties," *IET Control Theory A.*, vol. 14, no. 1, pp. 116–126, 2020.

[9] E. M. Abdel-Rahman, A. H. Nayfeh, and Z. N. Masoud, "Dynamics and control of cranes: A review," *J. Vib. Control*, vol. 9, no. 7, pp. 863–908, 2003.

[10] L. Ramli, Z. Mohamed, A. M. Abdullahi, H. I. Jaafar, and I. M. Lazim, "Control strategies for crane systems: A comprehensive review," *Mech. Syst. Signal Pr.*, vol. 95, no. 1, pp. 1–23, 2017.

[11] Y. Sung and W. Singhose, "Robustness analysis of input shaping commands for two-mode flexible systems," *IET Control Theory A.*, vol. 3, no. 6, pp. 722–730, 2009.

[12] W. Singhose, W. Seering, and N. Singer, "Residual vibration reduction using vector diagrams to generate shaped inputs," *J. Mech. Design*, vol. 116, no. 2, p. 654, 1994.

[13] W. Singhose, L. Porter, M. Kenison, and E. Kriikku, "Effects of hoisting on the input shaping control of gantry cranes," *Control Eng. Pract.*, vol. 8, no. 10, pp. 1159–1165, 2000.

[14] K. L. Sorensen, W. Singhose, and S. Dickerson, "A controllers enabling precise positioning and sway reduction in bridge and gantry cranes," *Control Eng. Pract.*, vol. 15, no. 7, pp. 825–837, 2007.

[15] D. Blackburn, J. Lawrence, J. Danielson, W. Singhose, T. Kamoi, and A. Taura, "Radial-motion assisted command shapers for nonlinear tower crane rotational slewing," *Control Eng. Pract.*, vol. 18, no. 5, pp. 523–531, 2010.

[16] J. Vaughan, D. Kim, and W. Singhose, "Control of tower cranes with double-pendulum payload dynamics," *IEEE T. Contr. Syst. T.*, vol. 18, no. 6, pp. 1345–1358, 2010.

[17] J. Vaughan, A. Yano, and W. Singhose, "Comparison of robust input shapers," *J. Sound Vib.*, vol. 315, no. 4, pp. 797–815, 2008.

[18] W. Blajer and K. Kołodziejczyk, "Motion planning and control of gantry cranes in cluttered work environment," *IET Control Theory A.*, vol. 1, no. 5, pp. 1370–1379, 2007.

[19] H. Chen, Y. Fang, and N. Sun, "Optimal trajectory planning and tracking control method for overhead cranes," *IET Control Theory A.*, vol. 10, no. 6, pp. 692–699, 2016.

[20] N. Sun, Y. Fang, and X. Wu, "An enhanced coupling nonlinear control method for bridge cranes," *IET Control Theory A.*, vol. 8, no. 13, pp. 1215–1223, 2014.

[21] N. Sun, Y. Fang, X. Zhang, and Y. Yuan, "Transportation task-oriented trajectory planning for underactuated overhead cranes using geometric analysis," *IET Control Theory A.*, vol. 6, no. 10, pp. 1410–1423, 2012.

[22] Z. Wu and X. Xia, "Optimal motion planning for overhead cranes," *IET Control Theory A.*, vol. 8, no. 17, pp. 1833–1842, 2014.

[23] K. Takagi and H. Nishimura, "Gain-scheduled control of a tower crane considering varying load-rope length," *JSME Int. J. C-Dyn. Con.*, vol. 42, no. 4, pp. 914–921, 1999.

[24] G. Bartolini, A. Pisano, and E. Usai, "Second-order sliding-mode control of container cranes," *Automatica*, vol. 38, no. 10, pp. 1783–1790, 2002.

[25] N. B. Almutairi and M. Zribi, "Sliding mode control of a three-dimensional overhead crane," *J. Vib. Control*, vol. 15, no. 11, pp. 1679–1730, 2009.

[26] Z. Xi and T. Hesketh, "Discrete time integral sliding mode control for overhead crane with uncertainties," *IET Control Theory A.*, vol. 4, no. 10, pp. 2071–2081, 2010.

[27] Z. Zhang, L. Li, and Y. Wu, "Disturbance-observer-based antiswing control of underactuated crane systems via terminal sliding mode," *IET Control Theory A.*, vol. 12, no. 18, pp. 2588–2594, 2018.

[28] X. Wu and X. He, "Enhanced damping-based anti-swing control method for underactuated overhead cranes," *IET Control Theory A.*, vol. 9, no. 12, pp. 1893–1900, 2015.

[29] J. Huang, E. Maleki, and W. Singhose, "Dynamics and swing control of mobile boom cranes subject to wind disturbances," *IET Control Theory A.*, vol. 7, no. 9, pp. 1187–1195, 2013.

[30] I. Mizumoto, T. Chen, S. Ohdaira, M. Kumon, and Z. Iwai, "Adaptive output feedback control of general mimo systems using multirate sampling and its application to a cart-crane system," *Automatica*, vol. 43, no. 12, pp. 2077–2085, 2007.

[31] Q. Ngo and K.-S. Hong, "Adaptive sliding mode control of container cranes," *IET Control Theory A.*, vol. 6, no. 5, pp. 662–668, 2012.

[32] L. A. Tuan, S.-C. Moon, W. G. Lee, and S.-G. Lee, "Adaptive sliding mode control of overhead cranes with varying cable length," *J. Mech. Sci. Technol.*, vol. 27, no. 3, pp. 885–893, 2013.

[33] M. Robertson and W. Singhose, "Robust discrete-time deflection-limiting commands for flexible systems," *IET Control Theory A.*, vol. 3, no. 4, pp. 473–480, 2009.

[34] Y. Zhang, S. Agrawal, and P. Hagedorn, "Longitudinal Vibration Modeling and Control of a Flexible Transporter System with Arbitrarily Varying Cable Lengths," *J. Vib. Control*, vol. 11, no. 3, pp. 431–456, 2005.

[35] A. Walsh and J. R. Forbes, "Modeling and control of a wind energy harvesting kite with flexible cables," *P. Amer. Contr. Conf.*, no. 1, pp. 2383–2388, 2015.

[36] H. A. Godbole, R. J. Caverly, and J. R. Forbes, "Dynamic modeling and adaptive control of a single degree-of-freedom flexible cable-driven parallel robot," *J. Dyn. Syst.-T. ASME*, vol. 141, no. 10, pp. 1–13, 2019.

[37] B. Brogliato, R. Lozano, B. Maschke, and O. Egeland, *Dissipative systems analysis and control: theory and applications*, 3rd ed., ser. Communications and control engineering. Cham: Springer, 2020.

[38] C. J. Damaren, "Approximate Inverse Dynamics and Passive Feedback for Flexible Manipulators with Large Payloads," *IEEE T. Robot. Autom.*, vol. 12, no. 1, pp. 131–138, 1996.

[39] E. G. Christoforou and C. J. Damaren, "Application of passivity-based techniques to the control of structurally flexible gantry robots," *IEEE Int. Conf. Robot.*, no. 5, pp. 324–329, 2011.

[40] R. J. Caverly and J. R. Forbes, "Dynamic modeling and noncollocated control of a flexible planar cable-driven manipulator," *IEEE T. Robot.*, vol. 30, no. 6, pp. 1386–1397, 2014.

[41] R. J. Caverly, J. R. Forbes, and D. Mohammadshahi, "Dynamic Modeling and Passivity-Based Control of a Single Degree of Freedom Cable-Actuated System," *IEEE T. Contr. Syst. T.*, vol. 23, no. 3, pp. 898–909, 2015.

[42] C. Damaren, "Adaptive control of flexible manipulators carrying large uncertain payloads," *J. Robotic Syst.*, vol. 13, no. 4, pp. 219–228, 1996.

[43] C. J. Damaren, "Passivity and Noncollocation in the Control of Flexible Multibody Systems ," *J. Dyn. Syst-T. ASME*, vol. 122, no. 1, pp. 11–17, 1999.

[44] A. H. J. De Ruiter, C. J. Damaren, and J. R. Forbes, *Spacecraft dynamics and control : an introduction.* Chichester, West Sussex, UK: John Wiley and Sons Ltd., 2013.

[45] P. C. Hughes, *Spacecraft attitude dynamics*, ser. Dover Books on Aeronautical Engineering Ser. Mineola, New York: Dover Publications, 2004.

[46] H. J. Marquez, *Nonlinear Control Systems: Analysis and Design.* Hoboken, NJ: Wiley, 2003.

[47] C. A. Desoer, *Feedback systems: input-output properties*, ser. Electrical science. New York: Academic Press, 1975.

[48] J.-J. E. Slotine and W. Li, "On the adaptive control of robotic manipulators," *Int. J. Robot. Res.*, vol. 6, no. 3, pp. 49–59, 1987.

Appendix A

Detail of the Full EOM

The equations of motion of the full system with a flexible hoist cable is derived in Chapter 2 as equation (2.6). The full details of the mass and non-linear matrices are included in Appendices A.1 and A.2.

A.1 Mass Matrix

The mass matrix $\mathbf{M} = \begin{bmatrix} M_{11} & M_{12} & M_{13} & \mathbf{M}_{14} \\ * & M_{22} & M_{23} & \mathbf{M}_{24} \\ * & * & M_{33} & \mathbf{M}_{34} \\ * & * & * & \mathbf{M}_{44} \end{bmatrix}$ is given by

$$
\begin{aligned}
M_{11} &= m_1 + m_2 + m_w + \rho_c A L, \\
M_{12} &= r \sin\theta \left(m_2 + \rho_c A \left(\ell_i + \mathbf{\Lambda}_1 \mathbf{q}^e \right) \right), \\
M_{13} &= -\cos\theta \left(m_2 \left(\ell_i + \mathbf{\Psi}_\ell \mathbf{q}^e \right) + \rho_c A \ell_i \left(\frac{\ell_i}{2} - \mathbf{\Lambda}_2 \mathbf{q}^e \right) \right), \\
\mathbf{M}_{14} &= -\sin\theta \left(\mathbf{\Psi}_\ell + \rho_c A \ell_i \mathbf{\Lambda}_2 \right), \\
M_{22} &= r^2 \left(\frac{m_w}{2} + m_2 + \rho_c A \left(L + 2\mathbf{\Lambda}_1 \mathbf{q}^e + \mathbf{q}^{e\mathsf{T}} \frac{\mathbf{\Lambda}_{11}}{\ell_i} \mathbf{q}^e \right) \right), \\
M_{23} &= 0, \\
\mathbf{M}_{24} &= -r \left(m_2 \mathbf{\Psi}_\ell + \rho_c A \left(\ell_i \mathbf{\Lambda}_2 + \mathbf{q}^{e\mathsf{T}} \mathbf{\Lambda}_{12} \right) \right), \\
M_{33} &= m_2 \left(\ell_i^2 + 2\ell_i \mathbf{\Psi}_\ell \mathbf{q}^e + \mathbf{q}^{e\mathsf{T}} \mathbf{\Psi}_\ell^{\mathsf{T}} \mathbf{\Psi}_\ell \mathbf{q}^e \right) \\
&\quad + \rho_c A \left(\frac{\ell_i^3}{3} - 2\ell_i^2 \mathbf{\Lambda}_{21} \mathbf{q}^e + \ell_i \mathbf{q}^{e\mathsf{T}} \mathbf{\Lambda}_{22} \mathbf{q}^e \right), \\
\mathbf{M}_{34} &= \mathbf{0}, \\
\mathbf{M}_{44} &= m_2 \mathbf{\Psi}_\ell^{\mathsf{T}} \mathbf{\Psi}_\ell + \rho_c A \ell_i \mathbf{\Lambda}_{22},
\end{aligned}
$$

A.2 Non-linear Matrices

The nonlinear terms of the equations of motion are $\mathbf{f}_{non} = \mathbf{C}_{non}\left(\mathbf{q}, \dot{\mathbf{q}}\right) \dot{\mathbf{q}} + \mathbf{G}_{non}\left(\mathbf{q}\right)$, including the matrices $\mathbf{C}_{non} = \begin{bmatrix} C_{n,11} & C_{n,12} & C_{n,13} & \mathbf{C}_{n,14} \\ C_{n,21} & C_{n,22} & C_{n,23} & \mathbf{C}_{n,24} \\ C_{n,31} & C_{n,32} & C_{n,33} & \mathbf{C}_{n,34} \\ C_{n,41} & C_{n,42} & C_{n,43} & \mathbf{C}_{n,44} \end{bmatrix}$ and $\mathbf{G}_{non} = \begin{bmatrix} G_{n,1} \\ G_{n,2} \\ G_{n,3} \\ G_{n,4} \end{bmatrix}$,

where

$$
\begin{aligned}
C_{n,11} &= 0, \\
C_{n,22} &= \dot{\phi}(-\frac{3}{2}\rho A r^3 \mathbf{q}^{e\mathsf{T}} \frac{\mathbf{\Lambda}_{11}}{\ell_i^2}\mathbf{q}^e) + (-\rho A r^2(\mathbf{\Lambda}_1 + \mathbf{q}^{e\mathsf{T}}\frac{\mathbf{\Lambda}_{11}}{\ell_i}))\dot{\mathbf{q}}^e, \\
C_{n,33} &= -m_2(\ell_i + \mathbf{\Psi}_\ell \mathbf{q}^e)(\dot{\ell}_i + \mathbf{\Psi}_\ell \dot{\mathbf{q}}^e) - \rho A(\ell_i^2 \mathbf{\Lambda}_{21} + \ell_i \mathbf{q}^{e\mathsf{T}}\mathbf{\Lambda}_{22})\dot{\mathbf{q}}^e \\
&\quad - \tfrac{1}{2}\rho A \dot{\ell}_i(\ell_i^2 + 4\ell_i \mathbf{\Lambda}_{21}\mathbf{q}^e + \mathbf{q}^{e\mathsf{T}}\mathbf{\Lambda}_{22}\mathbf{q}^e), \\
C_{n,44} &= \dot{\phi}(\rho A r(-\frac{\mathbf{\Lambda}_{12}}{2} + \mathbf{\Lambda}_{22})), \\
C_{n,12} &= \dot{\phi}(\rho A r^2 \sin\theta) + \dot{\theta}(\rho A r \cos\theta(\mathbf{\Lambda}_2 - \mathbf{\Lambda}_1)\mathbf{q}^e) + (-\rho A r \sin\theta \mathbf{\Lambda}_2)\dot{\mathbf{q}}^e, \\
C_{n,21} &= \dot{\theta}(-m_2 r\cos\theta - \rho A r\cos\theta(\ell_i + (\mathbf{\Lambda}_2 - \mathbf{\Lambda}_1)\mathbf{q}^e)) + (\rho A r \sin\theta \mathbf{\Lambda}_2)\dot{\mathbf{q}}^e, \\
C_{n,13} &= \dot{\phi}(\rho A r\cos\theta(\mathbf{\Lambda}_1 - \mathbf{\Lambda}_2)\mathbf{q}^e) + (m_2\cos\theta\mathbf{\Psi}_\ell + \rho A\cos\theta\ell_i\mathbf{\Lambda}_2)\dot{\mathbf{q}}^e \\
&\quad + \dot{\theta}(-m_2\sin\theta(\ell_i + \mathbf{\Psi}_\ell\mathbf{q}^e) - \rho A\sin\theta(\frac{\ell_i^2}{2} + \ell_i\mathbf{\Lambda}_2\mathbf{q}^e)), \\
C_{n,31} &= \dot{\phi}(-m_2 r\cos\theta - \rho A r\cos\theta(\ell_i + \mathbf{\Lambda}_1\mathbf{q}^e)), \\
C_{n,14} &= \dot{\phi}(\rho A r\sin\theta(\mathbf{\Lambda}_2 - \mathbf{\Lambda}_1)) + \dot{\theta}(m_2\cos\theta\mathbf{\Psi}_\ell + \rho A\cos\theta\ell_i\mathbf{\Lambda}_2), \\
C_{n,41} &= \dot{\phi}(\rho A r\sin\theta\mathbf{\Lambda}_1^{\mathsf{T}}), \\
C_{n,23} &= \dot{\theta}(-m_2 r(\ell_i + \mathbf{\Psi}_\ell\mathbf{q}^e) - \rho A r(\frac{\ell_i^2}{2} + 2\ell_i\mathbf{\Lambda}_{21}\mathbf{q}^e + \mathbf{q}^{e\mathsf{T}}\frac{\mathbf{\Lambda}_{22}}{2}\mathbf{q}^e)), \\
C_{n,32} &= -C_{n,23}^{\mathsf{T}}, \\
C_{n,24} &= \dot{\phi}(-\rho A r^2(\mathbf{\Lambda}_1 + 2\mathbf{q}^{e\mathsf{T}}\frac{\mathbf{\Lambda}_{11}^{\mathsf{T}}}{\ell_i})) + \dot{\mathbf{q}}^{e\mathsf{T}}(\rho A r\frac{\mathbf{\Lambda}_{12}}{2}), \\
C_{n,42} &= \dot{\phi}(\rho A r^2(\mathbf{\Lambda}_1^{\mathsf{T}} - \mathbf{\Lambda}_2^{\mathsf{T}} + \frac{\mathbf{\Lambda}_{11}}{\ell_i}\mathbf{q}^e)) + (\rho A r\frac{\mathbf{\Lambda}_{12}^{\mathsf{T}}}{2})\dot{\mathbf{q}}^e, \\
C_{n,34} &= \dot{\theta}(-m_2(\ell_i + \mathbf{\Psi}_\ell\mathbf{q}^e)\mathbf{\Psi}_\ell - \rho A(\ell_i^2\mathbf{\Lambda}_{21} + \ell_i\mathbf{q}^{e\mathsf{T}}\mathbf{\Lambda}_{22}^{\mathsf{T}})), \\
C_{n,43} &= -C_{n,34}^{\mathsf{T}},
\end{aligned}
$$

$$
\begin{aligned}
G_{n,1} &= 0, \\
G_{n,2} &= -\tfrac{1}{2} EAr \mathbf{q}^{e\mathsf{T}} \frac{\mathbf{\Lambda}_{33}}{\ell_i^2} \mathbf{q}^e - gr\cos\theta(m_2 + \rho A(\ell_i + \mathbf{\Lambda}_2 \mathbf{q}^e)), \\
G_{n,3} &= -g\sin\theta(m_2(\ell_i + \mathbf{\Psi}_\ell \mathbf{q}^e) - \rho A(\frac{\ell_i^2}{2} + \ell_i \mathbf{\Lambda}_2 \mathbf{q}^e)), \\
G_{n,4} &= g\cos\theta(m_2 \mathbf{\Psi}_\ell^{\mathsf{T}} + \rho A \ell_i \mathbf{\Lambda}_2^{\mathsf{T}}).
\end{aligned}
$$